ALGERIAN DEMOCRATIC AND POPULAR REPUBLIC
MINISTRY OF HIGH EDUCATATION AND SCIENTIFIC RESEARCH

UNIVERSITY FRERES MENTOURI CONSTANTINE 1
FACULTY OF SCIENCES EXACTES
DEPARTMENT OF PHYSICS

Order N°:05/phy/2018
Series :71/D3C/2018

THESIS

PRESENTED FOR LMD DOCTORAT DEGREE REQUIREMENT

SPECIALITY

Nanomaterials and Advanced Materials

THEME

Study of a nanostructured compound based on II-VI semiconductors (ZnS)

By

GHEZALI KHAOULA

Jury committee:

President :	**M. SEBAIS**	**Prof.**	**Univ. Frères Mentouri Constantine 1**
Advisor:	**B. BOUDINE**	**Prof.**	**Univ. Frères Mentouri Constantine 1**
Co-advisor:	**A. AZIZI**	**Prof.**	**Univ. Ferhat Abbas-Sétif 1**
Examiners:	**O. HALIMI**	**Prof.**	**Univ. Frères Mentouri Constantine 1**
	L. ZERROUAL	**Prof.**	**Univ. Ferhat Abbas-Sétif 1**
Invited	**N. TABET**	**Prof.**	**QEERI- HBKU, Qatar**

Soutenu le 27/06/2018

DEDICATE

THIS PRESENT WORK IS DEDICATED TO:

MY UNCLE AND MY GRAND MOTHER

MY MOTHER AND MY FATHER

MY HUSBAND

MY BROTHERS YOUCEF AND SELMAN

MY SISTER'S SALSABIL AND AMINA

MY AUNT MOUNIRA

AND MY FRIENDS AMEL HADJER FATIMA SAMIHA AND SARA

Acknowledgements

Firstly, I would like to express my sincere appreciate to my main advisor Boubakeur Boudine professor at Constantine University and my co-advisor Amor Azizi professor at Sétif-1 University. I could not have imagined having better advisors and mentors for my PhD. Thank you for supervising my thesis work and for supporting and encouraging me along the way, and for enthusiasm and inspiration, which was always there when I needed it. Thank you for your patience in reading and correcting my thesis. Throughout my thesis-writing period, you provided encouragement, sound advice, good teaching, and many good ideas.

I would like to express my gratitude to Prof. Tabet Nouar for his guide, encouragement, trust all the times, and help in the whole research work in Qatar. Without his support and input, this thesis would not have been completed so fast. Particularly, with your immense knowledge, you help me open a new door when I only have a small window to look into the physics world. It is my honour to be your student and I am proud of it.

I would also like to express my sincere thanks to Loubna Mentar for her encouragement, support and help.

I address my thanks to Miloud Sebais, Ouahiba Halimi Professors of Constantine-1-University and Larbi Zerroual Professor of Sétif-1 University, for their acceptance to judge this modest work.

Many thanks to everyone in Setif-1(LCIMN), Constantine-1(Crystallography laboratory) and HBKU University in Qatar (QEERI): O. baka, M. R. Khaladi, Pr. A. Belaidi, Pr, Belabbes. Pr. A, Merzougui, Pr. Fahhad H. Alharbi, Dr. Md, Anower Hossain, Pr. H. Hamoudi, Dr. A. Abdallah, Dr. R. Al-Gaashani, W. Ali for their help in various situations over last few years.

For my Uncle and my parents, words are not enough to express my gratitude for you. Without your selfless love and endless support, I cannot be me today. Thank you for always being there

Finally, I would like to give heartfelt thanks to all the people for their care and help during my work!

Contents

Figures captions

Chapter I

Chapter II

Chapter III

Introduction

The synthesis of low dimensional materials comprising thin films and nanostructures from easily available and environmentally friendly starting materials along with exploration of cost–effective deposition methods are main challenges of today's materials science. Today, nanostructured materials attract a considerable attention owing to the development of the daily life needs. Nanostructured materials are a new class of materials having dimensions in the nanometers range, which provide one of the greatest potentials for improving performance and extended capabilities of products in a number of industrial sectors. Different form of nanostructures could be obtained such as nano-particles, nano-rods, nano-tubes, nano-foams, nano-pillars, nano-layers and nano-flakes have dominated the research field in the past two decades. It has increased the appreciation of materials in the community and been a topic of much interest even amongst chemists, physicists, and other scientists and engineers, because of the potential applications that can be exploited due to the possibility of attaining unusual properties, as well as the new science that can be understood in terms of material behavior due to nano-scale structures.

In recent years, research on semiconductor nanostructures is of great interest. Semiconductor chalcogenides have attracted considerable attention due to their important unique physical and chemical properties. The II-VI semiconductor nanostructures have shown to be an important group with considerable progresses in the synthesis and utilization of their unique properties in extensive and novel applications, one of the intensively studied properties is the large band gap [1]. In the present work we focus our work on the study of Zinc sulfide nanostructures, owing to their interest properties.

Zinc sulfide (ZnS) is one of the first semiconductors discovered [2]. It has traditionally shown remarkable versatility and promise for novel fundamental properties and diverse applications. The nanoscale morphologies of ZnS have been proven to be one of the richest among all inorganic semiconductors [3]. It is a promising candidate for diverse applications such as light-emitting diodes (LEDs), infrared windows, electroluminescence, lasers, photovoltaic cells and sensors, catalysts, cathode-ray tubes (CRT), field emission display (FED) phosphors for a long time [4]. It can also be used for electroluminescent devices and photodiodes [5]. A Characteristic of nanostructures is the high surface to volume ratio, which induces the structural and electronic changes. These differences depend on particle sizes, shape and surface characteristics. The decrease of particle sizes causes an extremely high surface area to volume ratio. The increase of surface area to volume ratio favors surface states, which change the activity of electrons and holes, and affects the chemical reaction

dynamics [2]. Therefore, much research on ZnS nanostructures and their physicochemical properties has been carried out and various methods have been used for the preparation of these nanostructures [6]–[9]. ZnS can be also used in semiconductor heteronanostructures. Nanostructures where two or more materials are used can produce new optical and electrical properties. An example is core/shell QD, where ZnS is used for shell i.e. barrier [10].

Up to the beginning of the present investigation, a very limited number of studies was reported by various physical and chemical methods: spray pyrolysis [5], Chemical bath deposition [11], radio-frequency (RF) magnetron sputtering [12], pulsed laser deposition [16], atomic layer deposition [6], sol gel process [13] and electrodeposition [8]. Electrochemical deposition is one of the most interesting methods for the synthesis of thin films of semiconductors. It provides serval advantages over other film processing techniques such as the ability to use a low synthesis temperature, cost effectiveness, large area deposition, controllable thickness and morphology [14]. Also, electrodeposition experimental parameters can be controlled more precisely. Many research groups have adopted this method to prepare ZnS thin films. They found that the electrodeposited thin films exhibit a low transmittance in the visible range, in order to improve this property, the obtained thin films was annealed at 300 and 400 °C [15], It need energy and more time for this reason, several researchers have been using doping by foreign elements to improve the optical properties [16], [17]. We report for the first time the effect of the electrodeposited rare earth (Er, Sm) doped ZnS, to improve the optical properties.

The main purpose of this thesis is to study the effect of different electrodeposition parameters as well as the doping by rare earths (Er, Sm) on the electrochemical, morphological, structural and optical properties of the ZnS thin films.

The thesis is organized as following:

A general bibliographic review was presented in chapter I. The first part of this chapter is devoted to the presentation of some generalities on nanostructures and the II-VI semiconductors. When the second part is devoted exclusively to ZnS, the properties, defects and the different fields of application of this material.

The second chapter is concerned exclusively to the different experimental techniques used for the deposition of undoped and doped ZnS nanostructures and the techniques used for their electrochemical, morphological, structural and optical characterizations.

In the third chapter of this thesis we present the results of the electrodeposited ZnS thin films at different parameters (variation of zinc concentration, pH, deposition potential and time) and the obtained results will be discussed in details.

In the last chapter we presents the results (electrochemical, structural and optical) of the films doped with the rare earths (Er, Sm)

At the end of this manuscript we give a general conclusion in which we summarize the principal results of this work.

Chapter I

Zinc sulphide nanostructures

Chapter I ZnS thin films and nanostructures

Chapter I ZnS thin films and nanostructures

This chapter is intended to provide a bibliographic basis to help us understand the following chapters. For this, we embark on this part, an introduction on the semiconductors II-VI as a general point of view, after that we interest in the case of ZnS nanostructures. A brief description of different deposition parameters going to be reported, followed by a description of doping ZnS nanostructures. Then we expose some morphological, structural and optical properties that give a remarkable capability for a wide variety of uses of the undoped and doped ZnS nanostructures. At the end we represent the most important applications in various technological areas.

I.1. Nanotechnology

Nanotechnology is defined to be the development at the atomic, molecular or macromolecular levels using a length scale of approximately one to one hundred nanometers in any dimension. The creation and use of structures, devices and systems that have novel properties and functions and the ability to control or manipulate matter on an atomic scale.

As we are aware that nanostructures are the age of the future, a lot of interesting research going on currently and therefore the literature has been growing very fast in these area. Nanostructures could be defined as structures designed on atomic or molecular scale in which at least one dimension is measured in nanometers [18]. A nano is 10^{-9} that's a really small number so let we put into perspective for us a Nano here is to a meter as marble is to the diameter of the entire earth, how's that for scale. The interest in these materials has been stimulated by the fact that, owing to the small size of building blocks (particle, grain or layer) and the high surface-to volume ratio, significant increase in grain boundary area, these materials are expected to demonstrate unique mechanical, optical, electronic, and magnetic properties [19]. Due to their superior properties, nanostructured materials find a wide range of applications in novel electronic and optical nano devices etc. [19]. Controlled and cost–effective fabrication, investigation, and further integration of nanomaterials to nano devices is a great challenge in nanoscale technology.

I.2. Wide band gap II-VI Semiconductors

The wide band gap II-VI semiconductors are compounds formed with $A^{II}B^{VI}$, where A is an element from group II (Zn, Cd, Hg) and B an element from the group VI (O, S, Se, Te). These compound semiconductors have been the subject of extensive research for several decades in both fundamental studies and device applications [20]. The broad range of band gaps and lattice constants have been key factors that make II-VI semiconductor widely study and improved compared to other semiconductors. Because of this, II-VI semiconductors are particularly attractive for a wide range of

applications such as optoelectronic devices, infrared lasers and detectors, blue-green lasers and light emitting diodes (LEDs), nonlinear optical materials, magneto-optical devices and radiation detectors [21]. Such applications have significantly improved photonics, computers, telecommunications as well as many other industries and technologies. Nevertheless, during 1960 and 1970 II-VI semiconductors did not receive much attention from the semiconductor community due to limitations of growth and doping techniques. Only in the 1980 and 1990, with the advent of advanced crystal growth techniques such as metal-organic chemical vapor deposition (MOCVD) and molecular beam epitaxy (MBE), a new surge of research devoted to II-VI emerged. Presently, with progress of thin films deposition techniques and along many new directions, including spintronic, optoelectronics, quantum heterostructures, and II-VI materials gains much interest.

Among these materials, Zinc Sulphide (ZnS) is becoming one of the most important II-VI direct band gap semiconductor. ZnS thin films are prepared by several techniques such as sputtering [22] spray pyrolysis [5], pulsed laser deposition (PLD) [23] thermal evaporation [24], chemical bath deposition (CBD) [11] and electrodeposition [14]. Each technique has its specifications and advantage characteristic however, the electrodeposition is one of the simple, easy, inexpensive and safe technique and it doesn't require any heavy or costly equipment's. It has been used to procure large homogeneous areas of the deposited films.

I.3. Properties and preparation techniques

Most of the II-VI semiconductors crystallize in two structures: cubic zinc blend structure or hexagonal Wurtzite structure, where an anion is surrounded by four cations and vice- versa. The atoms of the column II are located in the positions (0,0,0), (0,1/2,1/2), (1/2,0,1/2), (1/2,1/2,0), while the atoms of the VI column are in located in the sites (1/4,1/4,1/4), (1/4,3/4,3/4), (3/4,1/4,3/4), (3/4,3/4,1/4) [20]. Some II VI semiconductors properties are shown in table I. 1.
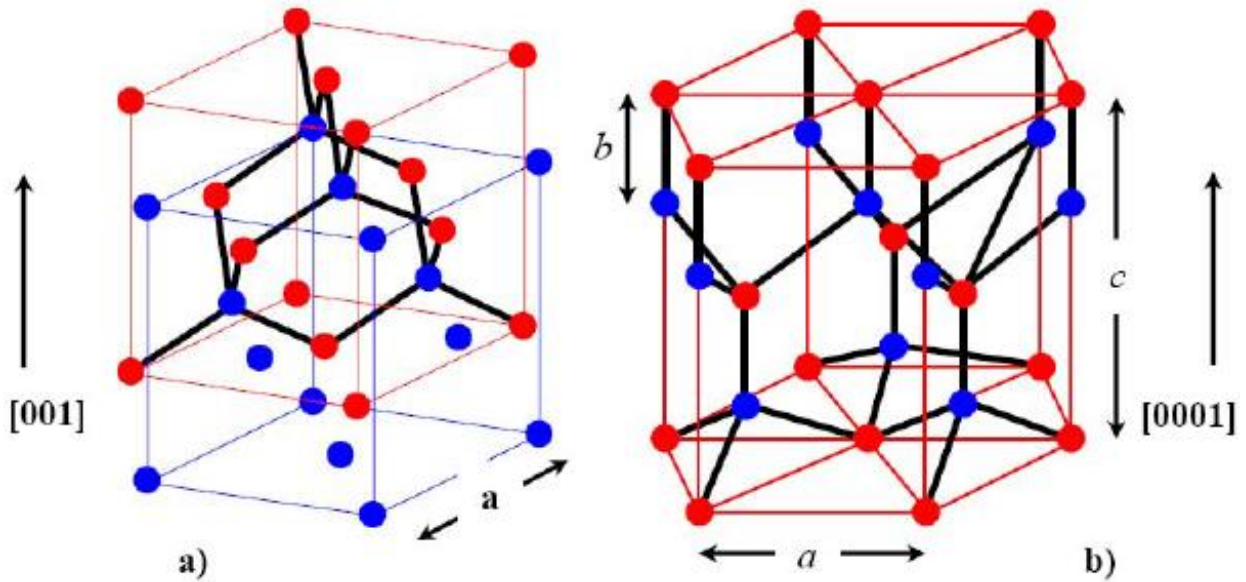
Figure I. 1: *Crystalline structures of the a) Diamond and zinc blende (cubic) and b) Wurzite (hexagonal) semiconductors* [20].

Wide-bandgap II–VI compounds were commonly grown using different physical and chemical techniques. The first deposits II-VI nanostructures experience was done using the conventional vapor-phase epitaxy (VPE) method for 60s.With the development of science and technology, new and higher requirements arose for material preparation. For this reason, a novel epitaxial growth techniques were developed(hot-wall epitaxy (HWE) [25], metalorganic chemical vapor deposition (MOCVD) [26], molecular-beam epitaxy (MBE) [27], [28], metalorganic molecular-beam epitaxy (MOMBE) [29] and atomic layer epitaxy (ALE) [30]) to simplify the growth, by improve the quality of the deposited compounds and facilitate the control of the film thickness, those methods are highly expensive and perhaps requires a large amount of material target. Since the need to produce good-quality thin films with low economical cost is necessary the chemical methods are presented such as: Chemical bath deposition (CBD) [31], sol-gel [32], spray pyrolysis [33], Chemical vapor deposition (CVD) [34] , sputtering [35]and electrodeposition [36].

Table I. 1: *Properties of some wide-bandgap II–VI compound semiconductors* [21].

Material Property	ZnS	ZnO	ZnSe	ZnTe	CdS	CdSe	CdTe
Melting point (K)	2038(WZ, 150atm)	2248	1797	1513	2023 (WZ, 100 atm)	1623	1370 (ZB)
Energy gap Eg at 300K (eV) (ZB*/WZ*)	3.68/3.91	–/3.4	2.71/–	2.394	2.50/2.50	–/1.751	1.475
Structure	ZB/WZ	WZ	ZB/WZ	ZB	ZB/WZ	WZ	ZB
Lattice constant (ZB) a$_0$ at 300K (nm)	0.541		0.567	0.610	0.582	0.608	0.648
Lattice constant (WZ) a$_0$ = b$_0$ c$_0$ at 300K (nm)	0.3811 0.6234	0.324 0.520	0.398 0.653	0.427 0.699	0.4135 0.6749	0.430 0.702	
Dielectric constant ε$_0$/ε$_\infty$	8.6/5.2	8.6/4.	9.2/5.8	9.3/6.9	8.6/5.3	9.5/6.2	2.27/–

ZB:Zinc blend,W:Wurtzite

I.4 Zinc sulphide preparation

4.1 Solution processing- Electrochemical deposition

Recently, several attempts have been made to employ the electrodeposition process in which the ZnS nanostructures was deposited by pulse [19] or potentiostatic mod [20]. Nevertheless, the obtained films were not in good qualities, either poorly crystallized or in low purity. The critical reasons may lie in the much more positive Nernst potential of sulfur ($E_{(S_2O_3^{2-}/S)} \approx$ -0.7 V vs. SCE) than that of zinc ($E_{(Zn^{2+}/Zn)} \approx -1$ V vs. SCE), which would cause the preferential deposition of sulfur and consequently affect the qualities of the ZnS nanostructures.

Among the different solutions used for the development of ZnS nanostructures, we will mention, Hennayaka et al. [37], used an electrolyte bath containing 25 mM $ZnSO_4$ $7H_2O$ and 10 mMN$Na_2S_2O_3$. In addition, 10 mM Na_3-$C_6H_5O_7$ $2H_2O$ was added as a chelating agent. The pH of the solution was fixed at 4.10 using diluted H_2SO_4 acid. Xu et al. [36] used an acidic electrolytes (pH 3.5) containing 20 mM $Na_2S_2O_3$, (15‑25 mM) Zn $(CH_3COO)_2$, (0‑0.2 mM) $C_7H_6O_6S$, 0.375 mM Na_2SO_3 and 200 mM LiCl. Among them, the Na_2SO_3 was used as a stabilizing agent to keep the

6

relatively long lifetime of the $S_2O_3^{2-}$ containing acidic electrolytes, and the LiCl was used as a supporting electrolyte. And other research was using an acidic solution containing $ZnSO_4$ and $Na_2S_2O_3$ [15], [38].

4.2 Other solution processing methods

Changing the deposition method introduced changes to the first conditions used. One of the most influenced thing on the quality of the obtained nanostructures is the bath solution used for that. Starting by CBD technique, all we need is Beaker, hotplate, substrate, chemicals and timer. CBD technique has widely used for the elaboration of ZnS nanostructures, H, Ahn et al grown ZnS nanostructures on glass substrates by using an aqueous solution containing $ZnSO_4$ (0.010 M), ammonia (0.07 M), and thiourea (0.8 M) at 90 °C. The mixture was poured into a beaker and heated to $90^\circ C$. The process consisted of an aqueous bath whose temperature was controlled with a hot plate. When deposition temperature is reached, the glass substrate were introduced vertically into the solution. After deposition, the thin films were rinsed with distilled water and dried using N_2 gas [39]. Also sol-gel method attract much attention for the elaboration of ZnS nanostructures, different capping agent or stabilizer were used for the preparation of deposition solution and different parameters should be controlled. M, Akhtar et al. [40] synthesized ZnS nanostructures from an aqueous solution of Na_2S was mixed drop wise to the aqueous solution of $Zn (NO_3)_2$ under continuous stirring using magnetic stirrer. Nitric acid (0.5M) was used to control the pH of solutions. During synthesis of ZnS, no capping agent or stabilizer was used. After two hours of vigorous stirring at 60°C, clear and transparent solution was obtained. Prepared solution were then left for aging for 24 hours in order to give sufficient time to reactants for complete reaction. The aged samples were deposited on cleaned glass substrates via spin coating under specific speed.

I.5 Electrochemical deposition control factor

Many research groups have adopted electrochemical deposition method to prepare ZnS thin films at various deposition parameters. The electrodeposition of ZnS thin films was first reported by C. D. Lokhande et al. [41] from a $ZnSO4-Na_2S_2O_3$ solutions. The films was electrodeposited cathodically on two different substrates (stainless steel and indium tin oxide-coated (ITO) glass) at -300 mV vs. SCE.

N, Fathy *et al.* [42] were studied the effect of bath concentration on the properties of the ZnS thin films obtained by pulse deposition. In this study, two different bath were used, the first group grown from $ZnSO_4$-rich solution and the second grown from $Na_2S_2O_3$-rich solution, they discussed the optical and electrical properties of ZnS thin films grown from both solution. It was found that the

transparency of the as-deposited films obtained from the $ZnSO_4$-rich solution is higher than that obtained from the $Na_2S_2O_3$-rich. Also, it is shown that the annealing of the films at 300 °C for 1 h improves the transmission and the photosensitivity. For electrical properties, they found that Au and In contacts have ohmic-like characteristics to ZnS and the resistivity of the as-deposited films is lower than the resistivity of the annealed films.

On the other hand, A. Kassim *et al.* [42], were electrodeposited ZnS thin films on an indium tin oxide glass substrate (using a potensiostatic mode) using zinc chloride, sodium thiosulfate and triethanolamine solutions at room temperature. The triethanolamine complexing agents was added to improve the quality of the obtained thin films. Also, they studied the effect of both applied potential and deposition time on the formation of the deposits. The X-ray diffraction patterns confirm the presence of ZnS for all the samples and the AFM images indicate that the grain size decreases as the cathodic potential becomes more negative at various deposition periods. As a comparison between all the prepared samples with different conditions they report that the film deposited at -1.1 V during 30 min had a homogenous, uniform and high crystallinity (Fig. I.2).
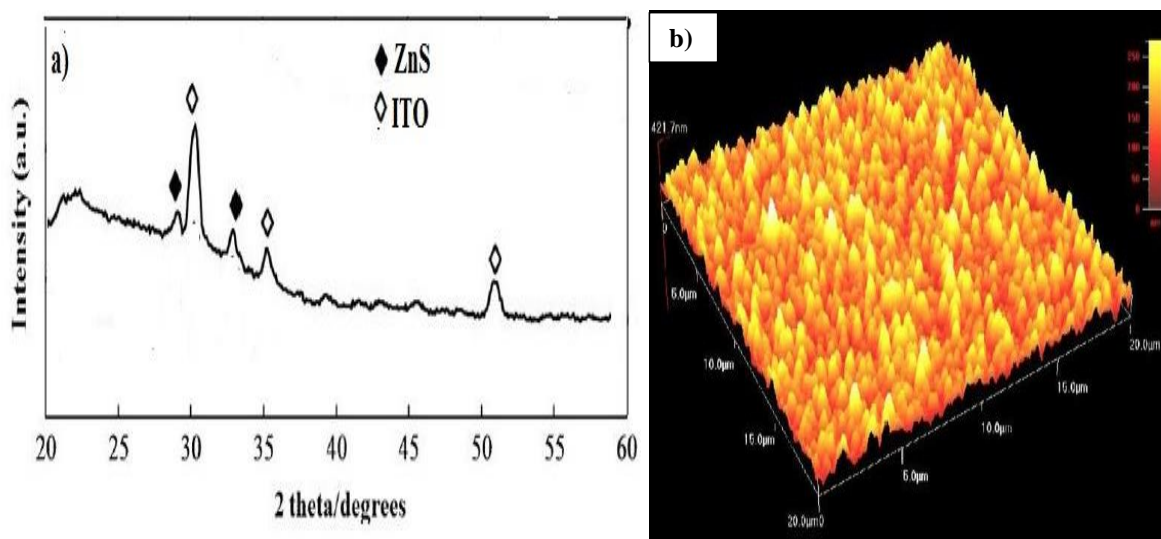
Figure I. 2: *a) X-ray diffraction patterns and b) AFM image of ZnS thin films deposited for 30 min at $^-$1.1 V [42].*

The electrochemical preparation of ZnS thin films by a Galvanostatic mode was studied by Xu *et al.* [14]. The deposition was performed at 10 mA.cm^{-2} in acidic electrolytes containing 15-30 mM $Zn(CH_3COO)_2$, 20 mM $Na_2S_2O_3$, 200 mM LiCl, 0.375 mM Na_2SO_3, and 0.0 or 0.2 mM $C_7H_6O_6S$. The results show that the presence of $C_7H_6O_6S$ can suppress the precipitation of Zn and S impurity phases during the ZnS deposition process. The deposited ZnS film exhibits only hexagonal structure with an ideal Zn/S atomic ratio of 1.03 and a close-packed granular morphology. The estimated optical band gap of the as-deposited films was equal to 2.86 eV, this value is smaller than the common

value of ZnS. After annealing, the band gap value was increased to 3.70 eV and the crystalline phase transformed from hexagonal to cubic structure (Fig. I.3).
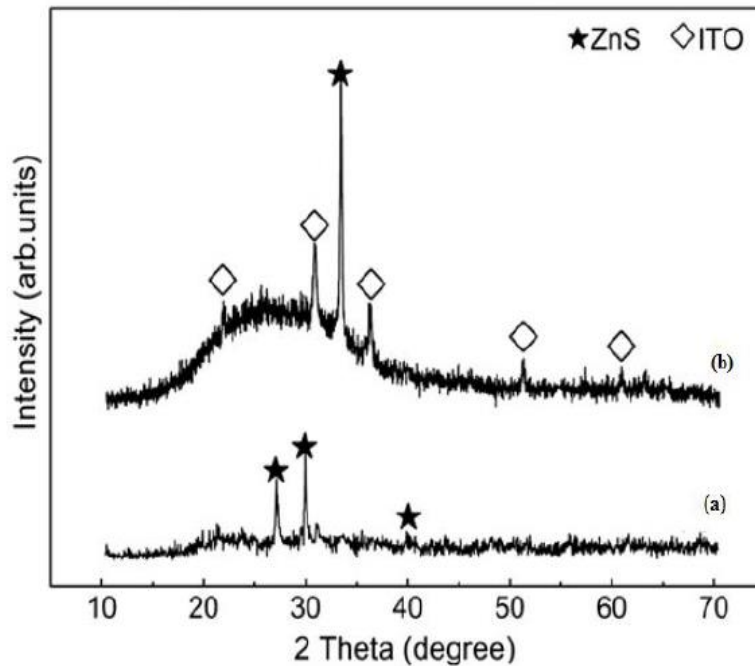
Figure I. 3: *XRD patterns of the film (a) before and (b) after annealing [14].*

Also, Hennayaka et al. [37] were grown ZnS thin films on ITO glass substrates from a $ZnSO_4$-$Na_2S_2O_3$ solutions using pulsed electrodeposition. $Na_3C_6H_5O_7\cdot 2H_2O$ was added as a chelating agent. The effect of the deposition temperature on the structural and optical properties of the ZnS films was investigated. As the deposition temperature increased, a polycrystalline cubic ZnS was obtained for all films and its optical transmittance and bandgap decreased because its thickness and grain size increased (Fig.I.4). Moreover, the ZnS films grown at 90 °C exhibited the highly (200) preferred orientation and n-type conductivity with a wide bandgap of 3.75 eV.
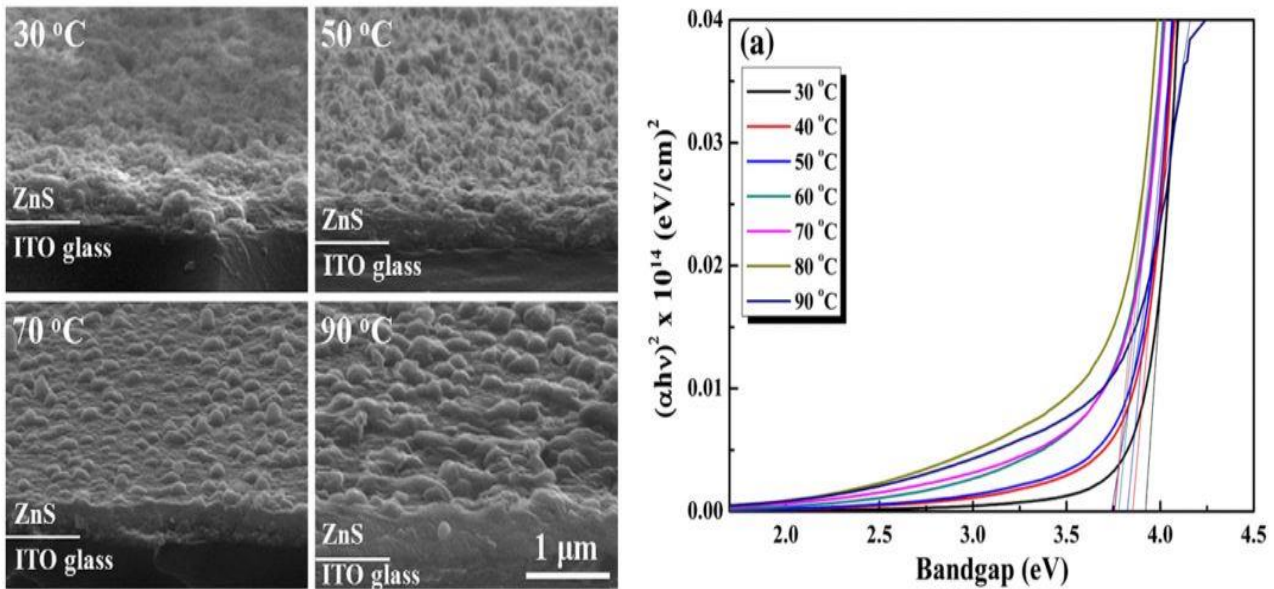
Figure I. 4: *(a) Cross section view FE-SEM images of the ZnS and (b) optical bandgap obtained at different deposition temperatures* [37].

I.6 Doping zinc sulphide

6.1 Defect in ZnS

Understanding the behaviors of native point defects is essential to the successful application of any semiconductor. For example, native point defects often influence or control the conductive type (n- or p- type) of semiconductors. Besides, they often control, directly or indirectly, doping, minority carrier lifetime, and luminescence efficiency. Theoritical study of the native point defect have been done by several researchers [43]–[45]. Here we describe some results:

- **Antisites**

Zinc antisites (Zn_S) introduce defect states in the band gap occupied by two electrons, which might be excited to the conduction band, thus acting as donors. Therefore, zinc antisites cannot provide electrons to the conduction band by thermal excitation. On the other hand, they have high formation energy. In S-rich conditions, their formation energy is extremely high for any position of the Fermi level in the band gap but in Zn-rich conditions, the Zn_S defects will not occur in high concentrations. Contrary to zinc antisites, sulfur antisites (S_{Zn}) introduce partially occupied states in the band gap, which can accept additional electrons to act as acceptors. The S_{Zn} is located at 2.57, 2.81 and 3.09 eV above the Valence Band Maximum (VBM) [45]. These levels are too deep for the S_{Zn} defects to provide holes to the valence band by thermal excitation, thus they cannot contribute to the p-type conductivity of ZnS. The formation energy of the S_{Zn} defects is always high in Zn-rich than S-rich conditions.

- **Vacancies**

TheSulfur vacancies (V_S) defect is not stable at all the Fermi level positions in the band gap and the defects will transit directly from the neutral to the 2+ charge state. The local relaxed geometries around sulfur vacancies in the neutral, 1+ and 2+ charge state is shown in Figure I. 5.

It's clearly seen that that the four nearest neighboring zinc atoms around V_S^0 are displaced inward, while those around V_S^{1+} and V_S^{2+} are displaced outward.

Sulfur vacancies are deep donors and they cannot contribute to n-type conductivity of ZnS. The formation energy of the V_S defects is low at the VBM in Zn-rich conditions. Therefore, they are very strong compensating centers in p-type ZnS. In S-rich conditions, sulfur vacancies have high formation energies. It means that the defects will not appear in observed concentrations if the materials are grown in S-rich and thermal equilibrium conditions.
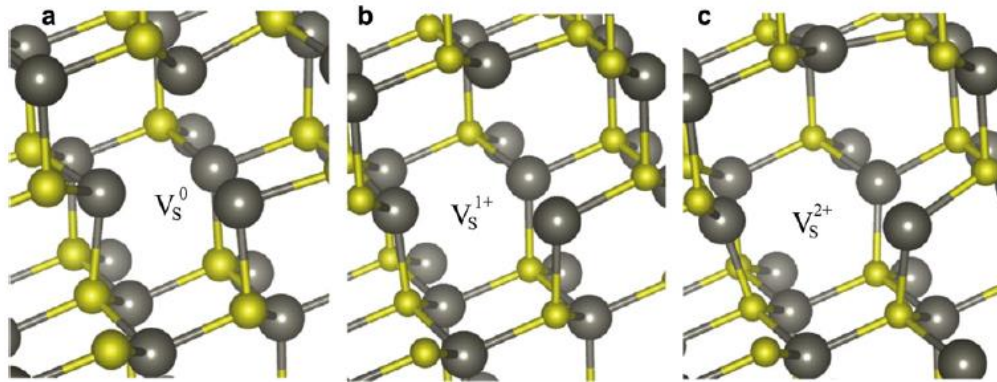
Figure I. 5: *Local atomic relaxations around the sulfur vacancy in the a) neutral, b) 1+, and c) 2+ charge states. Yellow and small balls denote sulfur atoms, and gray and big one denote zinc atoms* [45].

- **Interstitials**

There are two kinds of interstitial sites in zinc blende ZnS: one is the zinc cage site and the other is the sulfur cage site. The zinc cage site is the cubic body center of the ZnS conventional cell, while the sulfur cage site is the 1/4 site on body diagonal of the cubic. Zinc atoms can occupy both the zinc or sulfur cage sites (Zn_{Zn-I} or Zn_{S-i}), introducing defect states in the band gap occupied by two electrons, thus they may act as donors. However, their transition levels are in the upper part of the band gap, so they are deep donors. At room temperature, they cannot be excited and thus have no contributions to n-type conductivity. Besides, it's obtained that the Zn_{Zn-i} defects have the lowest high formation energy at the VBM in Zn-rich conditions, indicating they are strong compensation centers in p-type materials. In S-rich conditions, the formation energy of the Zn_{Zn-i} defects are always high,

thus they cannot occur in high concentrations. The Zn_{S-i} defects have high formation energies in both Zn- and S- rich conditions, so they are also difficult to form.

The deviation from perfect structure in a semiconductor material will exert much influence on the properties of the material. Therefore, the properties especially the conductivity can be tuned by controlling the stoichiometry during growth without the intentional doping of dopants.

The electrical property of a native semiconductor is determined by the dominative native defects under a certain growing conditions. For example, to be an n-type material, the dominative acceptor defects must have high formation energy and ionization energy. Meanwhile, the intrinsic compensation defects are abundant. To examine the formation of native n-type ZnS, we mainly focus on the regions where E_F is up towards the VBM [45].

6.2 Dopant materials

Generally, the n-type conductivity of ZnS is easily obtained by doping with the elements of group IIIA (Al, Ga, In, etc.) as a zinc substituent, or by the elements of the group VIIA (F, Br, etc.) as substituent of sulfur [46]. Those elements are incorporated into the ZnS lattice by forming deep donor levels, which contribute to the electrical conduction of ZnS.

The electrical properties of a semiconductor can also be engineered by the deliberate incorporation of impurities. Up to now, various doping materials including group V substituting on S site, group I elements and group IB elements (Cu, Ag, Au) on Zn site have been tried to investigate the p-type dopability of ZnS via the intentional incorporation of impurities, we attempt the same dopants as usually used in ZnO. For the dopant to be a good acceptor, it should have low ionization energy and high solubility under proper condition that does not favor the formation of compensation from native donors defects [46].

Various researchers have achieved such doping using different metals, such as aluminum, chromium [47], or several transition metals [48]. As found by Nasir [49], adding aluminum to a ZnS film results in the growth of free negative charge carriers. Doping ZnS films by chromium was achieved by the simultaneous co-evaporation of two precursors from different evaporators. Unfortunately, all of the experiments reported by Aamodt et al. [47] Show that incorporation of Cr in ZnS films results in an increase of their resistivity and tends to form Cr clusters instead of dissolving in the ZnS matrix. Zhang et al. [48] theoretically studied the incorporation of divalent transition metals (such as Cr, Mn, Fe, Co and Ni) in ZnS films. It was found that the incorporation of Cr, Ni and Fe ions in ZnS films increased light absorption in the visible region, which may be useful for the preparation of new solar cell prototypes.

I.7 Properties of zinc sulphide and doped Zinc sulphide

7.1 Morphologies

The morphology of the ZnS thin films have generally studied using SEM (microscopy electronic scanning) and AFM (Atomic Force Microscopy). It was established that the deposition parameters considerably influence the morphology of the deposited ZnS thin films. Ortiz-Ramos et al. [50] have obtained smaller aggregates, for the film prepared by CBD technique shown in figure I.6.a, the growth mechanism involved in the deposition of the ZnS films was the called cluster-by-cluster [51].
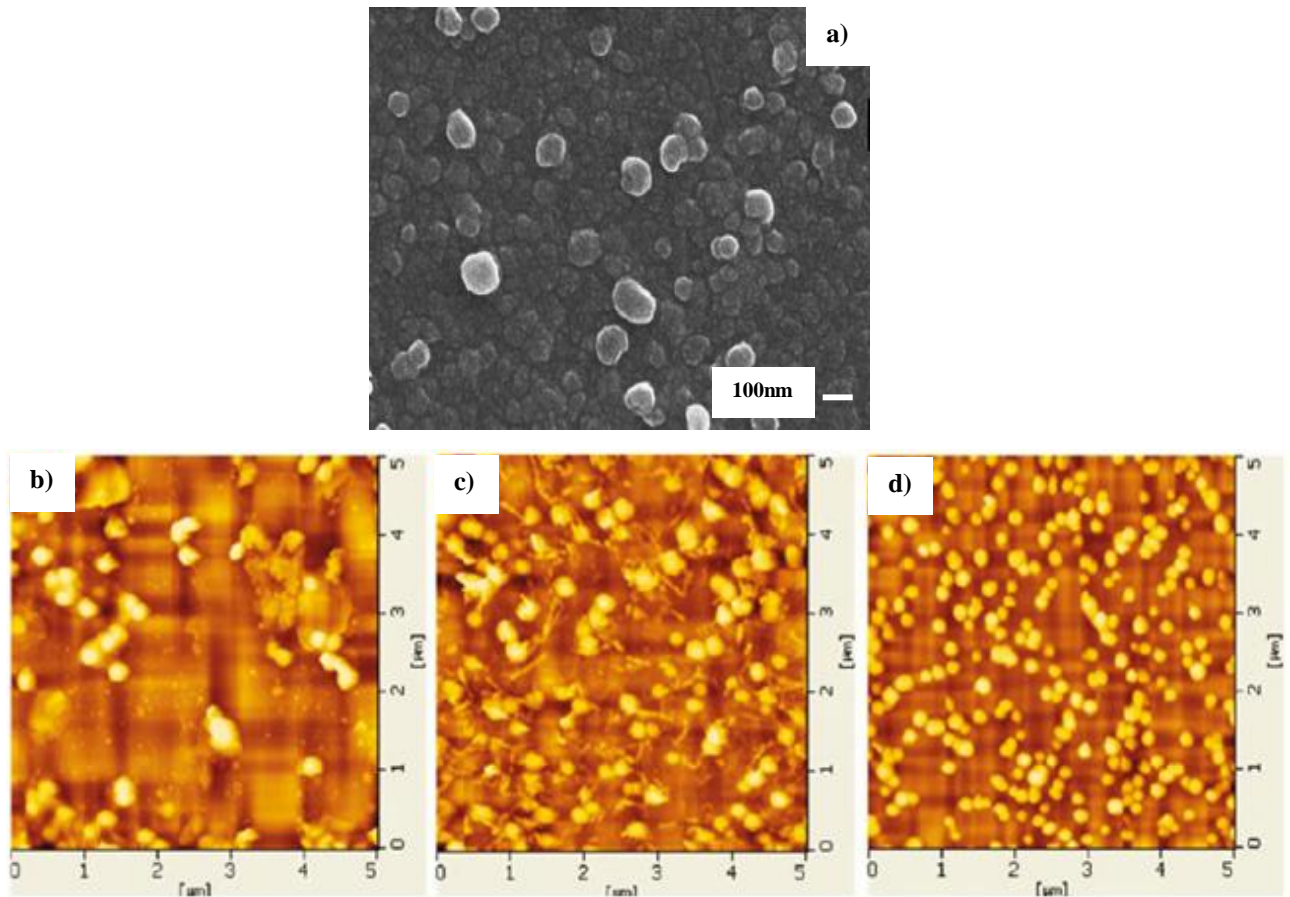
Figure I. 6: a) SEM surface images of the undoped ZnS film [50]*, AFM images (5 µm×5 µm) of the surfaces of ZnS films annealed at temperature of (b) 100°C, (c) 200°C, and (d) 300°C* [39]*.*

The influence of the post-annealing temperature on the surface morphology of the deposited ZnS thin film was reported by Ahn et al. [39], as revealed by AFM images shown in figure I. 6 (b, c and d) not only the annealed films composed of clusters, but they also possess more compact and smoother surfaces as the annealing temperature increases.

Another study was performed, Zhang et al. [52] used H_2S to sulfurize ZnO thin films at 500 °C. The increase of sulfidation time from 0.5 h to 5 h, leads to the enhancement of dense ZnS thin films (which is become slightly great) as shown in figure I. 7. The change in particle size was related to the recrystallization of ZnS and grain growth as well as the S replacement of O in the lattices will occur during sulfidation. Therefore, it is considered that during sulfidation of ZnO, oxygen sites in lattices are replaced by sulfur along with the recrystallization of ZnS, and the resultant ZnS thin films have the nanostructure along the c-axis. Clearly, the sulfur replacement of oxygen and recrystallization behaviors during sulfidation will be responsible for the increase in grain size of the sulfurized films. It had reported that, the grains before and after heating ZnS in sulfur vapor had greater change than in H_2S [53]. This means that ZnS recrystallization will be more favorable in sulfur vapor than in the H_2S-containing mixture. However, the recrystallization in sulfur vapor can form greater grains and thus hamper the sulfur diffusion and replacement of oxygen sites in crystal lattices.
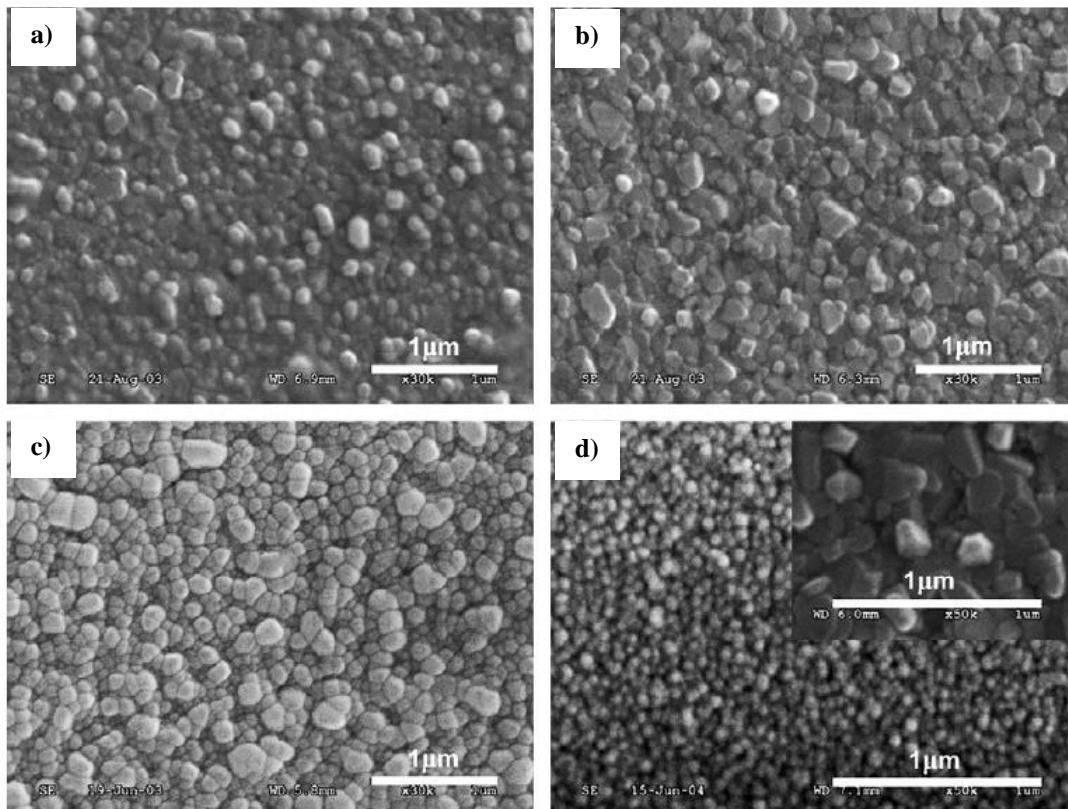
Figure I. 7: Low-magnification SEM patterns of the ZnS thin films produced by sulfidation for a) 0.5 h, b) 2 h and c) 5 h, respectively, and high-magnification SEM pattern of d) annealed ZnO thin film with the inset for it after sulfidation for 2 h [52].

It is necessary to point out that doping a semiconductor has a great effect on the morphology of the obtained thin films. Jayanthi et al. [54] studied the effect Cu doped ZnS thin film. They report that The ZnS:Cu thin films showed compact distribution over the surface and good connectivity between grains figure I. 8, for the Cu= 0.1M shown flake type formation with particle size distribution

about 200nm. In the case of 0.01 M Cu the flake type structure broke in to small size (100 nm), and fluffy mass was spread randomly over the surface.
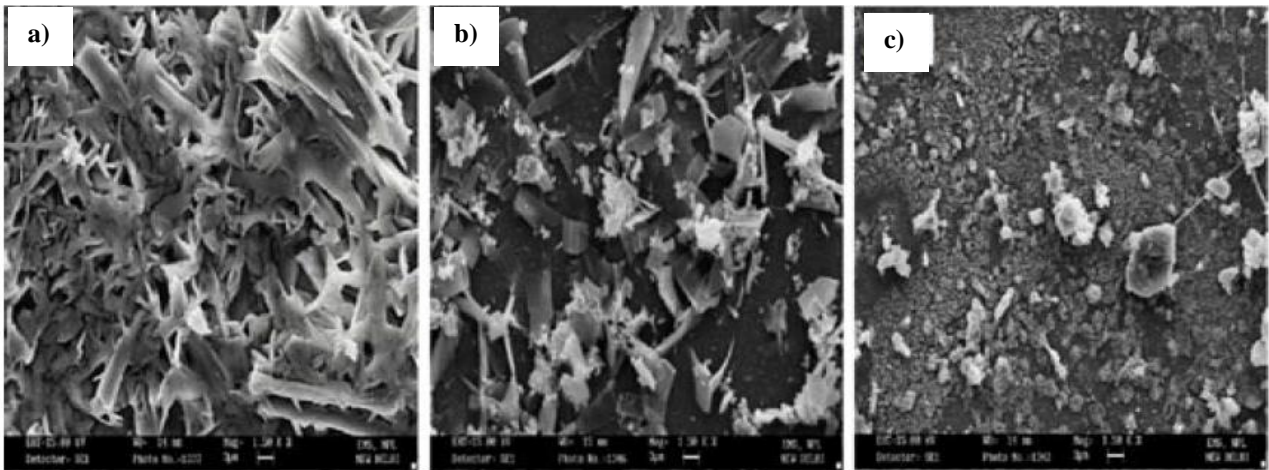
Figure I. 8: *SEM micrographs for ZnS:Cu nanoparticles with Cu concentrations of a) 0.1M, b) 0.01M and c) 0.001M* [54].

When the copper concentration was reduced from 0.01 to 0.001 M, the morphology of ZnS:Cu was totally changed. The particle size was very small, nearly about 50 nm. The fluffy mass was present in cluster form and they were not uniformly distributed. Mukherjeea et al. [55] compared the morphological aspect of two ZnS films deposited at room temperatures, pure and the doped with tin. The SEM images of the two films, pure and Sn-doped ZnS are shown in figure I. 9 no significant change in surface morphology was observed due to tin doping.
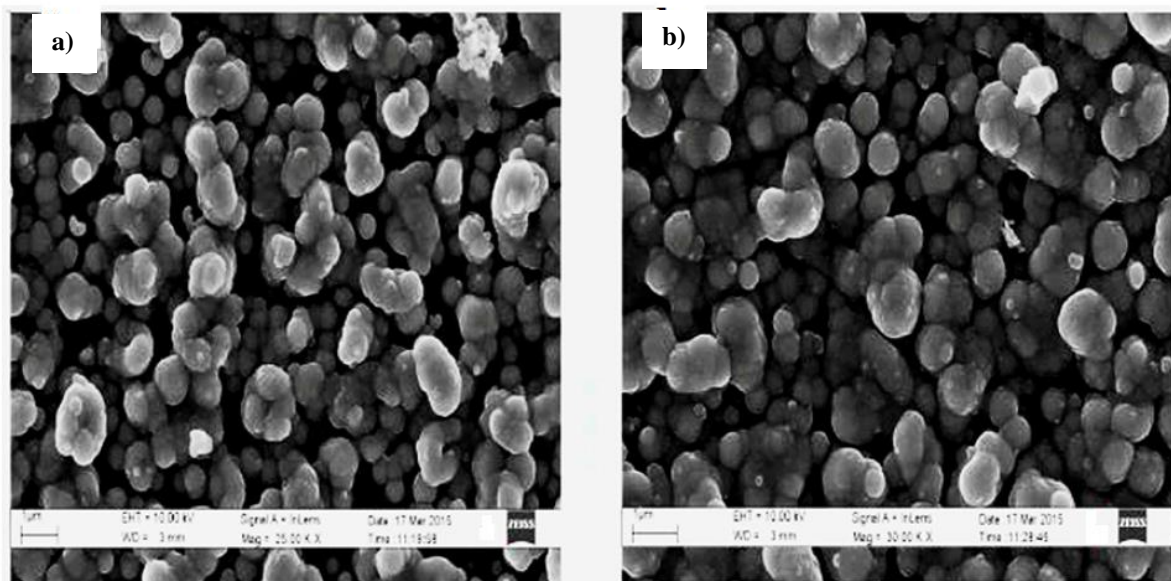
Figure I. 9: *FESEM image of a) ZnS and b) 5% Sn: ZnS* [55].

Nanoscale architectures have attracted strong interests due to their unique properties from large surface-to-volume ratio [56]. Recently, various ZnS 1-D nanostructures, such as nanowires, nanorods, nanotubes, and nanobelts, have successfully been synthesized [57]. Several kinds of nanoscale photodetectors built on 1-D ZnS nanostructures were also fabricated. For example, Fang et al. [58] fabricated individual ZnS nanobelt-based and multiple ZnS nanobelt-based UV-light photodetectors and Yu et al. [59] Also fabricated high-gain visible-blind UV photodetectors based on chlorine-doped n-type ZnS nanoribbons with tunable optoelectronic properties(Fig.I.10). However, due to the low photocurrent, there is still a great challenge to develop ZnS for practical applications.
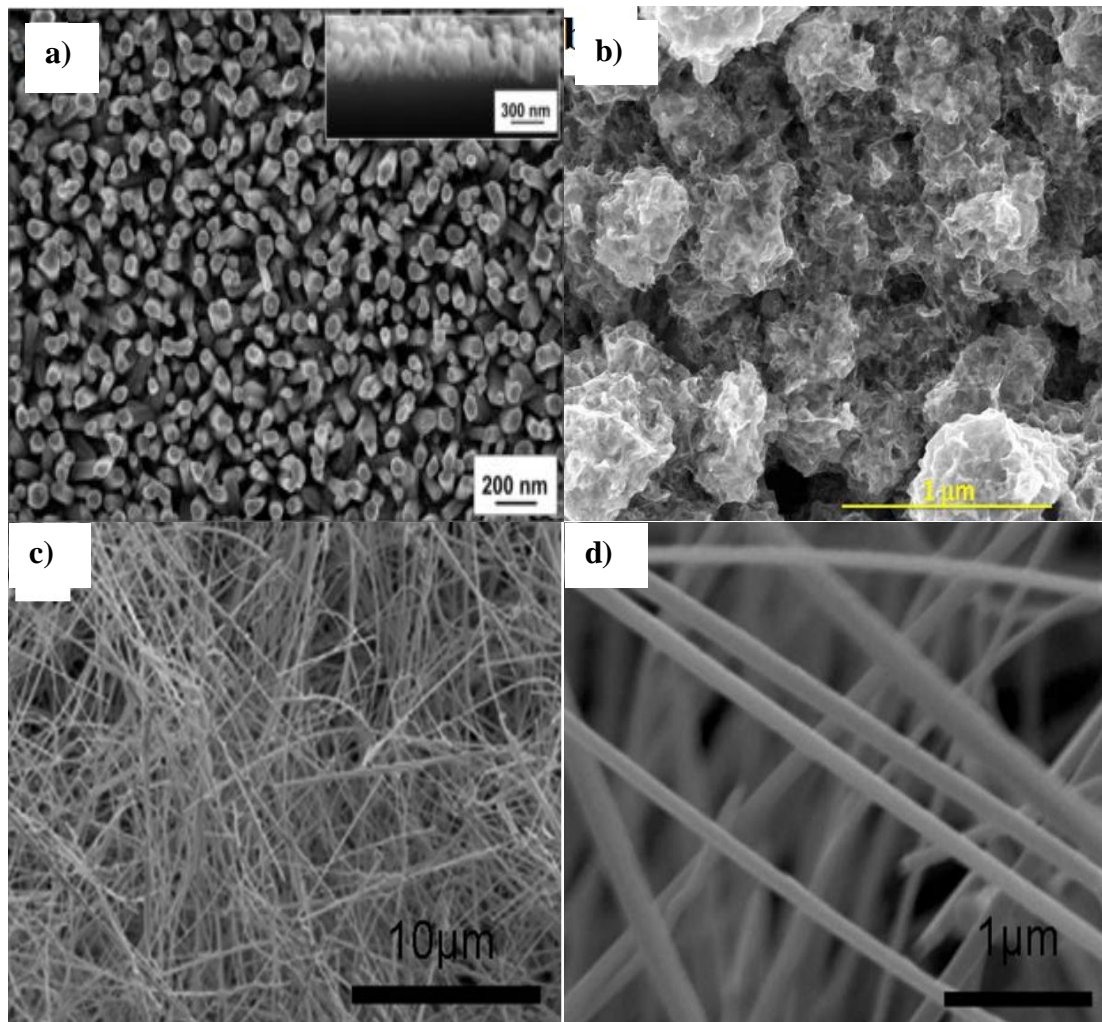
Figure I. 10: *ZnS nanostructures a) Nanorodes* [60] *b) Nanoflower* [56] *c) and d) Nanowires* [57].

7.2 Crytal structure

ZnS has two commonly available structures: one with a zinc blend structure and another one with a Wurtzite structure. The cubic form is the stable phase one at low-temperature, while the latter is going to be formed at high-temperature which forms at around 1296 K [61]. Several experimental and theoretical work has been done to study the effect of temperatures on the phase transformation.

Wurtzite   Zinc blende
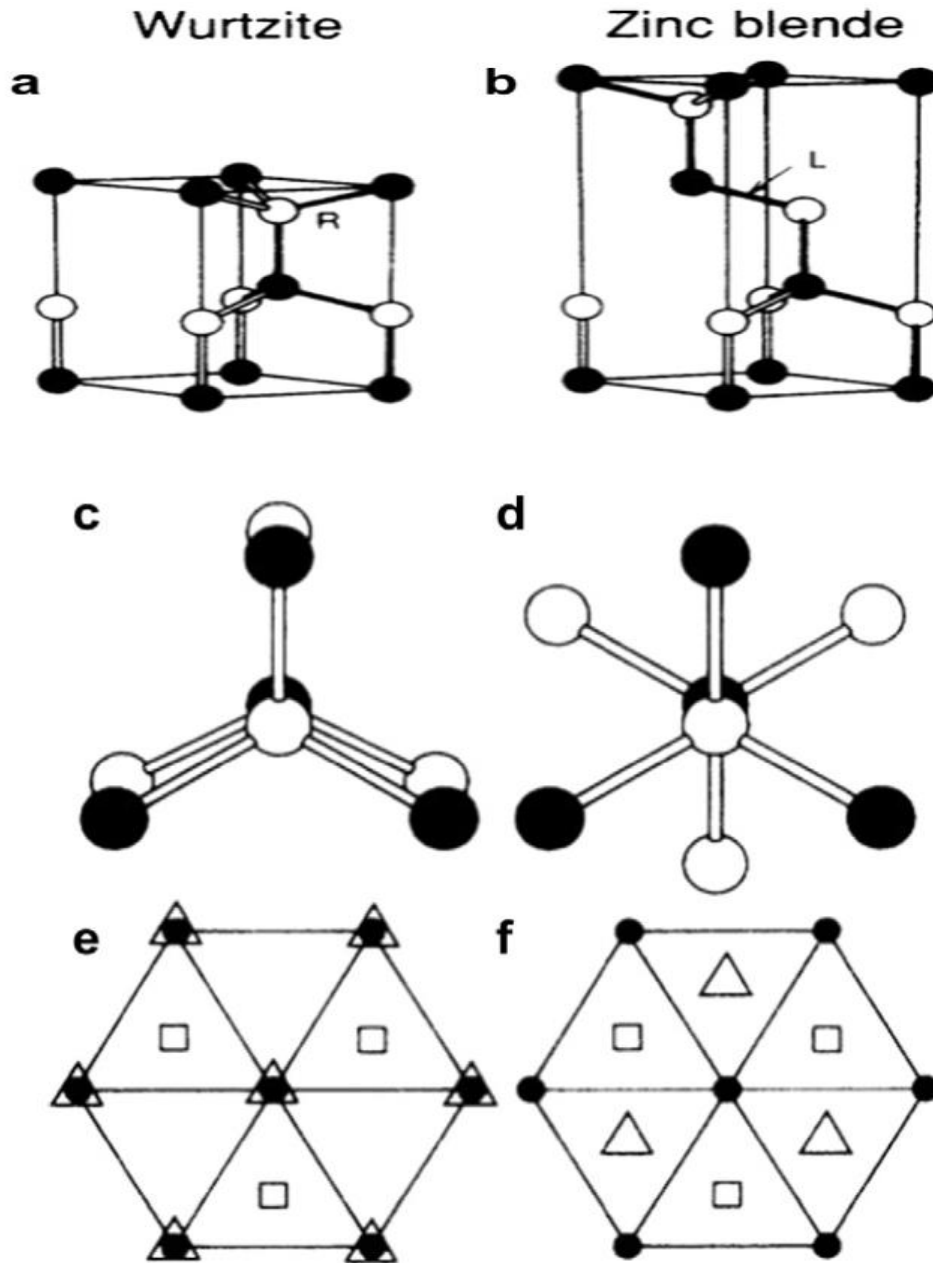
Figure I. 11: *Models showing the difference between wurtzite and zinc blende crystal structures. a) and b) Show handedness of the fourth interatomic bond along the right (R) for wurtzite and along the left (L) for zinc blende. c) and d) The respective eclipsed and staggered dihedral conformations. e) and f) Show atomic arrangement along the close packing axis* [61].

Figure I. 11 shows three different views of these structures, the difference in atomic arrangements leads to large difference in their properties. The differences can be described either in terms of the relative handedness of the fourth interatomic bond or by their dihedral conformations.

Alternatively, ZB consists of tetrahedral coordinated zinc and sulfur atoms stacked in the ABCABC pattern, while in WZ, the same building blocks are stacked in the ABABAB pattern. The

lattice parameters of ZB are a = b = c = 5.41 A, Z = 4 (space group F4-3 m) and that of WZ are a = b = 3.82 A, c = 6.26 A, Z = 2 (space group = P63mc).

The growth of thin films is strongly related to the deposition conditions and methods, different deposition methods leads to different properties of the obtained thin films. Indeed, to obtain a high quality of thin films different parameters should be controlled.

Various methods were used to elaborate ZnS thin film, with different characteristic. Arenas et al. [7] have studied the effect of divers parameters (different bath, temperature and air annealing) on the structural properties of the deposited ZnS thin films. The typical chemically deposited semiconductor thin film was obtained for the film deposited at 50 °C. Thereafter the preparation of the deposition bath, divers equilibrium chemicals and a nucleation layer of $Zn(OH)_2$ was formed over the surface of the substrate followed by the formation of ZnS thin films by the reaction:

$$Zn(OH)_2 + S^{2-} \rightarrow ZnS + 2OH^{2-} \tag{Eq. I}$$

The obtained XRD patterns of the as deposited thin films does not shown any diffraction peak, that is mean that the as deposited films were amorphous. A transformation phase from ZnS to ZnO was obtained, after air annealing at 500 °C for 5min, this phase was not stoichiometric. Kryshtab et al. [62] also studied the effect of annealing in S_2-rich atmosphere at atmospheric pressure. XRD patterns show a sphalerite structure with preferred orientation (111) for the ZnS film annealed at 950 °C, a transition phase for the deposited ZnS: Cu, Cl annealed at 800 °C the presence of Cu and Cl during the annealing process reduce the transition phase temperature. a great effort by several researchers was made to reduce the cost, high annealing temperature used in sophisticated methods strengthen the researchers to work with simple methods to reduce the cost. Hwang et al. [12] deposited.

ZnS thin films by RF magnetron sputtering, the temperature of the deposited substrate was ranged from 100-400 °C, a single crystalline structures with a preferential orientation (111) parallel to the substrate surface was obtained for all the films. When the best-preferred orientation structure was obtained at 350°C.

For the first time Eid et al. [63] obtained a polycrystalline, ZnS thin films prepared by chemical vapor deposition at room temperatures, figure I. 12 shows that the crystallinity of the ZnS thin films decreased as the annealing temperature increased till 200 °C. The overall intensity of the reflections decreased when the temperature of annealing increased without the appearance of any new reflections. This observation agrees with previous reported works [64], [65]. Annealing was not the only parameters that should be controlled during the study of structural properties,
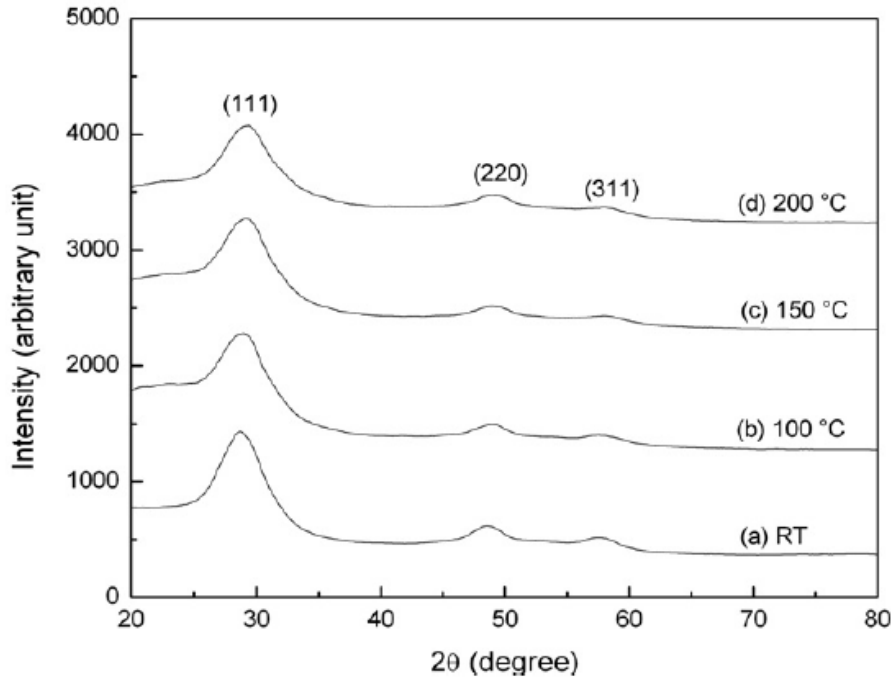
Figure I. 12: *XRD patterns of the deposited ZnS thin films at different annealing temperatures* [63]***.***

Omran Al-khayatt et al. [66] have studied the effect of zinc concentration on the structural properties. An increase in crystallinity by increasing the concentration of the zinc precursor was performed for the obtained wurzite ZnS thin films. The good choice of different parameters of deposition leads to a high crystallinity. Which encouraged researchers to study the role of deposition time [67], type of substrate [68], concentration of the precursor, complexing agent [69], doping [70], [71] and many other parameters.

7.3 Optical properties

Thin films have widely used in different applications such as solar cells, gas sensors ect ..., optical properties is one of the crucial parameters that should be controlled. The most frequently reported optical properties are: transmittance, absorbance and the optical gap.

a) Optical Transmittance

ZnS thin films are practically transparent, It exhibits a high optical transparency over a large region from the ultraviolet (UV) to the infrared (IR), which make it to be a good candidate to be used as a window layer in heterojunction photovoltaic solar cells. These films are uniform, smooth, transparent and a strong adhesion to the substrate. In general, transmittance is related to the deposition parameters thickness, gap, and crystal structure of the film. In figure I. 13 we have reported typical ZnS film transmittance spectra deposited with different pH by chemical bath deposition [11],. It

important to note that as the pH increases, the transmittance of the films increases. This increase is related to the film thickness as report in other study [72].
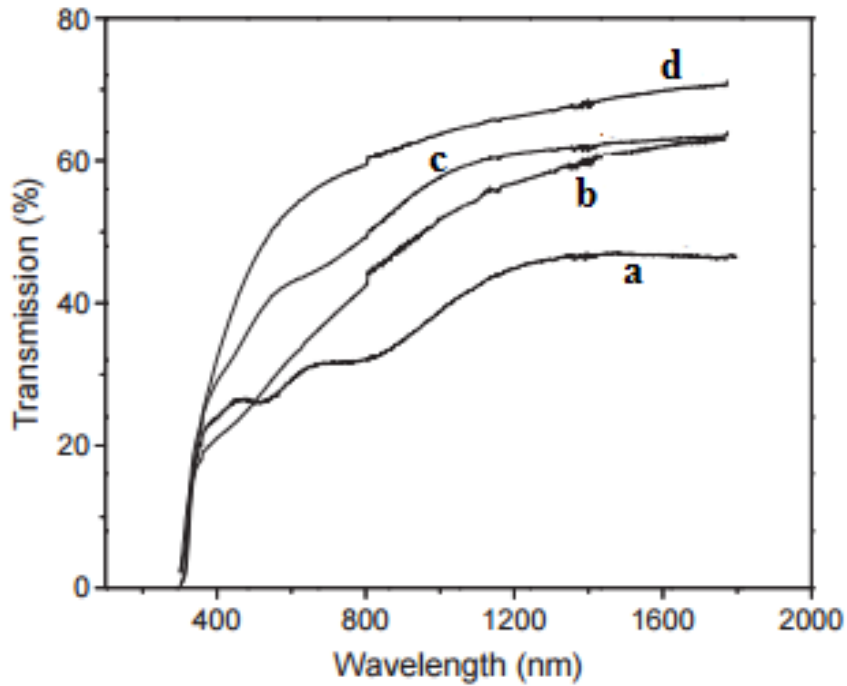
Figure I. 13: *Optical transmission spectra of ZnS thin films deposited at different pH of the chemical bath, a):10, b):10.31, c): 10.99 and d): 11.5* [11].

Figure I. 14 shows the transmittance spectra of the ZnS films coated with different thicknesses, high porosity was obtained which will tend to increase the crystallinity with the increase of the transmittance. This leads to a reduction in the thickness [73].
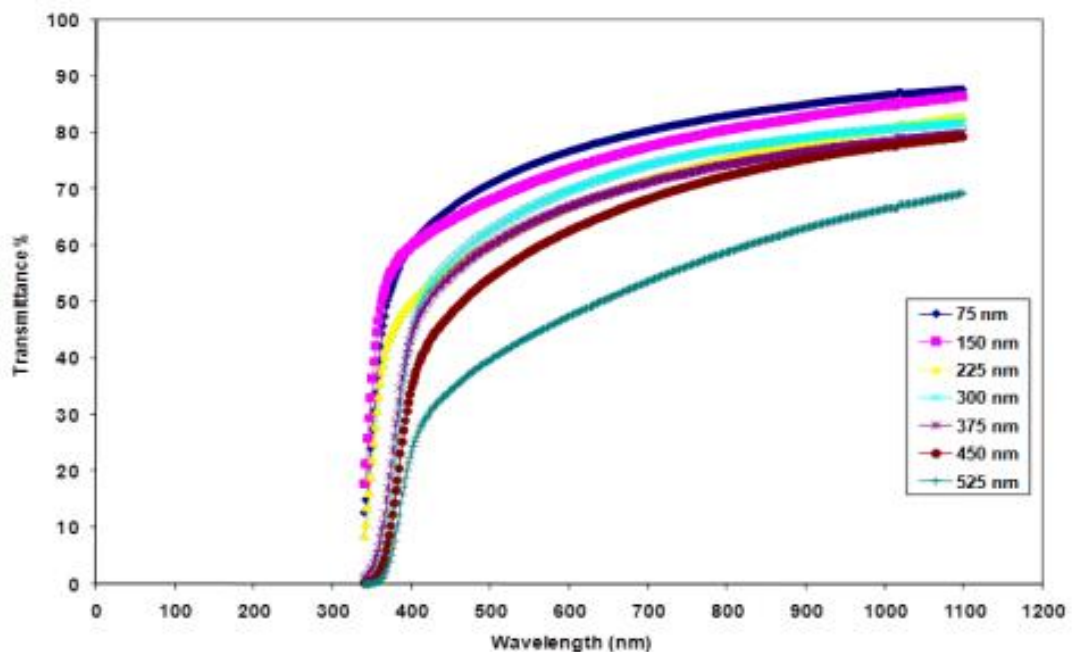
Figure I. 14: Optical transmission of ZnS thin films with different thickness [73].

The presence of interference fringes as shown in Figure I.15, is related to the thickness if it's almost constant and uniform [74].
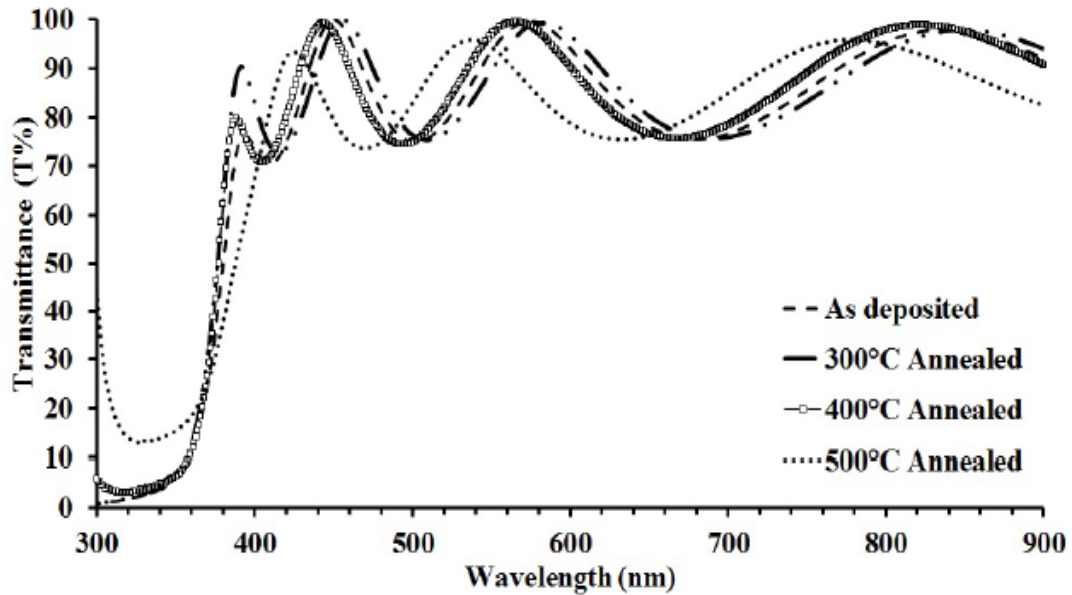
Figure I. 15: Transmittance vs. wavelength spectra of as-deposited and annealed ZnS thin films [74].

b) Band gap

Optical band gap was determinate frequently from the optical transmittance (absorbance). ZnS has a direct transition type band structure. The gap value of zinc sulfide (ZnS) is 3.5-3.7 eV at room temperature, as previously mentioned. In general, the variation of band gap energy values is influenced by several factors such as deposition temperature, film thickness, grains size, carries concentration, doping elements, shifting the stoichiometry of the film, the Urbach energy disorder and the chemical composition of the bath. The refractive index (n) of bulk ZnS is 2.47 at 450.9 nm and 2.32 at 708.5 nm, with the corresponding extinction coefficient (k) varying in the 10^{-5} to 10^{-6} range [5].

In the table I. 2, we have reported the variation of optical band gap for ZnS thin films deposited by CBD at different pH. It was found that the gap broadens as the pH of the solution decreases [11]. The shift to higher values of E_g is related to quantum confinement of ZnS thin films [10].

Table I. 2: *Band gap values of the ZnS thin films for different pH of the chemical bath [11].*

Ph	Optical band gap ($\pm 0.02\ eV$)
11.50	3.67
10.99	3.81
10.31	3.88
10.00	3.78

Jasib et al. [73] Have reported in table I. 3, the variations of the optical constants values, in this case the gap Eg. Increasing the thickness of the thin film causes a greater disorder (queue states) in the structure, which leads to a decrease in the band gap. In case of thick films, these allowed states could well merge with the conduction band resulting in the reduction of the band gap.

Table I. 3: *The values of optical energy gap for ZnS thin film with different Thickness [73].*

ZnS thickness (nm)	Eg (eV)
75	3.62
150	3.54
225	3.5
300	3.42
375	3.41
450	3.4
525	3.38

The doping of the ZnS thin films with other elements have a great effect on the band gap, Mukherjee et al. [55] have reported that Sn doping increases the fundamental absorption edge. The band gap energy increases from (3.69 eV for ZnS to 3.90 eV) for 5% Sn: ZnS. Such enhancement of bandgap might be due to enhancement of relative intensity of the major diffraction peak (100) corresponding to hexagonal wurtzite structure consequently leasing to a more ordered structure.

The doping of ZnS with Al was reported by Nagamani et al. [31] a slight blue shift was observed in the absorption edge with the increase of doping content in the films, leads to enhancement

of energy band gap. This can be attributed to the effective incorporation of Al dopant atoms into the ZnS lattice [31].

7.4 Electronic structure

Studies of materials properties in the vicinity of the gap give a special consideration in physics of solids. The conduction-band minima of the ZnS are much more dispersive than the valence band maxima for both phases (blende and wurtzite). The author's further state that mobility of electrons in these material is therefore higher than that of holes [75]. The electronic structure of zinc and sulfur are:

$$Zn: 3d10\ 4s2$$

$$S: 3s2\ 3p4$$
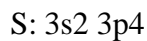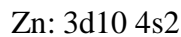
The study of band structure and DOS of ZnS were calculated by Yu et al. [59] an analysis of the band structure, presented in figure I. 16. We observe that both ZB and W phase have a direct band gap at the Γ point, An analysis of the DOS for the bulk ZnS polymorphs shows that uppermost valence band (VB) consists mainly of S 3p orbitals with a lesser contribution of hybrids Zn 4s and 4p orbital states.
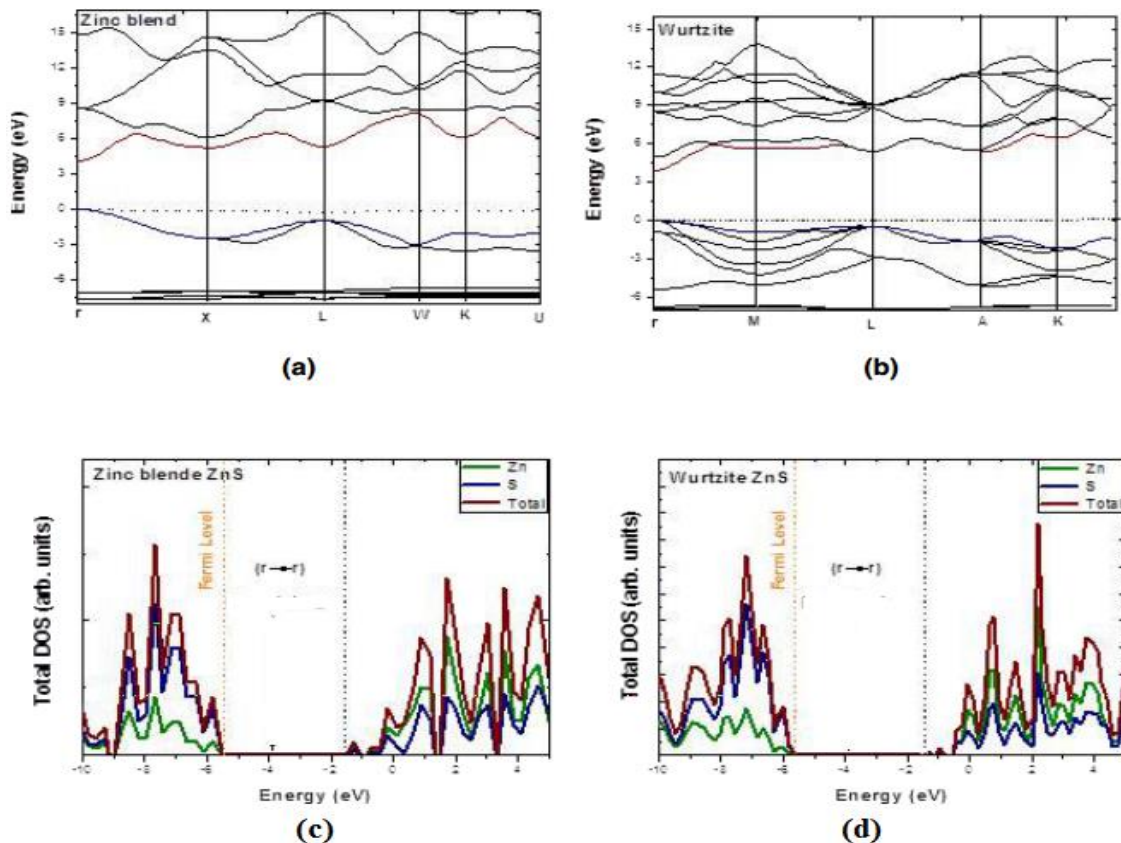
Figure I. 16: Band structures and projected DOS on atomic levels for ZnS polymorphs: a)–c) Zinc blende, b)–d) Wurtzite[59].

The presence of Zn 3d states in the VB in the ZnS polymorphs models reveals a strong bonding character between S and Zn. The conduction band (CB) consists mainly of hybridization of Zn 4s and 4p orbital states with a small contribution of S 3p orbitals. Also, p-electrons forming the topmost valence band states tightly bind to sulfur and make the valence band holes less mobile. Hence, the contribution of the holes to the conductivity is expected to be smaller. The valence band comprises of three regions: a lower region consists of the s bands of Zn and S, a higher-lying region contains well localized Zn 3d bands, and a top broader band originating from the s–p states hybridized with Zn 3d states. The fundamental relationship between the nature of chemical bonding and bulk properties in ZnS polymorphs, showing the presence of mixed ionic-covalent bonding for these materials. The bonding is predominantly covalent for ZB and W phases. While the Zn–S distance is 2.308, 2.313A for ZB, W, respectively [59].

7.5 ZnS conduction mechanism

Investigation of dc conductivity has been developed as a prevailing tool to understand the electrical transport mechanism in nanomaterials. Various conduction models such as space charge limited current (SCLC), Poole-Frenkel (PF) conduction mechanism and Richardson-Schottky (RS) emission have been reported to explain the conduction in nanomaterials. The detailed study of DC conduction mechanism in ZnS nanoparticles is still lacking in literature because no comprehensive report has been found so far. For synthesis of cubic ZnS nanoparticles, there exist several techniques such as solvo thermal method, hydrothermal method, solid state reaction method, sol–gel processing, chemical co-precipitation method and electrodeposition method.

I.8. Applications

ZnS is a promising material for various applications due to the abundance of its components in nature, low-cost production, good thermal stability, and electrochemical properties. Which make a suitable material for various application; electroluminescent devices (ELD), field effect transistor, photocatalysis, sensors, and solar cell [76].
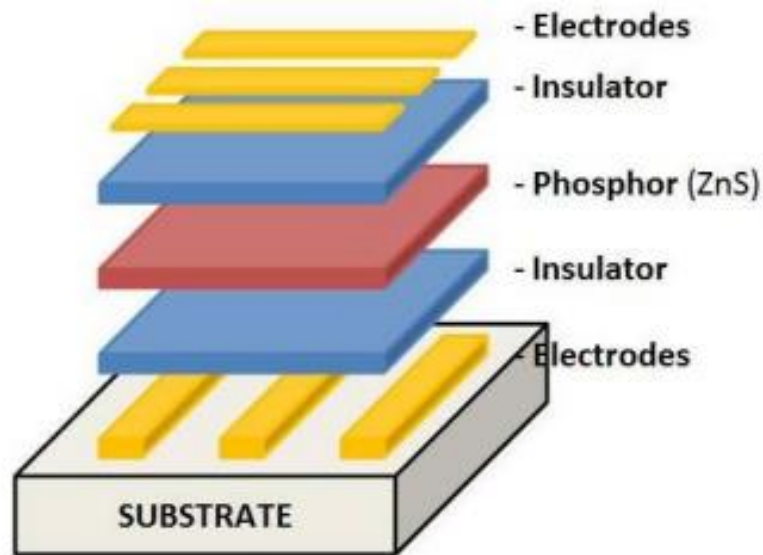
Figure I. 17: *Schematic of an electroluminescent display (ELD) device with ZnS as the phosphor material* [77].

        One of the first uses of ZnS was in nuclear physics as a scintillation detector (scintillation detector measures ionizing radiation), it also used in x-ray screens and cathode ray tubes [77]. ZnS is also an important phosphor host lattice material used in electroluminescent devices (ELD), because of the band gap large enough to emit visible light without absorption and the efficient transport of high-energy electrons [77].

Chapter II

Experimental procedure

Chapter II Experimental procedure

Chapter II Experimental procedure

In this chapter, a short overview of theoretical aspect of the experimental techniques used in this work are given. Cyclic voltammetry (CV) is the most common technique to obtain preliminary information about an electrochemical process. It is sensitive to the mechanism of deposition and therefore provides informations on structural transitions, as well as interactions between the surface and the ad-layer. Chronoamperometry is very powerful method for the quantitative analysis of a nucleation process. Mott-Schottky analysis help us to confirm the type of the obtained semiconductor. In addition, both scanning electron microscopy (SEM) and atomic force microscopy (AFM) were used to study the morphology of the obtained films. X-Ray Diffraction (XRD) analysis was used to study the crystalline content, identify the crystalline phases and preferential order of crystallites. Also, the UV-Vis analysis and the time resolved photoluminescence (TRPL) were employed for the study the optical properties and the life time, respectively. Theoretical background of these techniques will be given in the following pages.

II.1. Electrochemical studies

An Electrodeposition is well known for depositing metals and metallic alloys at the industrial level, such as Zn electroplating for surface treatment, Cu interconnect deposition on electronic chips, and Ni-Fe alloy for magnetic heads. However, an electrodeposition of a semiconductor is still an open challenge. Semiconducting properties are much more difficult to obtain than metallic properties since they control minority carriers at the ppm level, which is a priori much more difficult to achieve from solution processes than from vacuum ones [78].

Nevertheless researches have been devoted for long time to apply electrodeposition to the synthesis of semiconductors such as CdTe [79], CIGS [80], and other metal oxide [81] because of its unique advantages of low cost, low temperature, easy control over parameters, and large area deposition.

An electrodeposition is carried out by passing an electric current between two or more electrodes separated by an electrolyte. This deposition takes place at the electrode/electrolyte interface, which has the electrical double layer with a high potential gradient of 10^5 Vcm^{-1}. In general, the overall electrochemical reaction taking place in a cell is composed of two independent half-reactions. Each half-reaction responds to the interfacial potential difference at the corresponding electrode. Most of the time, one is interested in only one of these reactions, and the electrode at which it occurs is called the working electrode (WE). To focus on it, the other half of the cell is standardized

by using an electrode made up of phases having essentially constant composition, which is called the reference electrode (RE) [78]. The internationally accepted primary reference electrode is the standard hydrogen electrode (SHE) or normal hydrogen electrode (NHE) composed of $Pt/H_2/H^+$ (aqueous).

However, in the scientific experiment, the saturated calomel electrode, $Hg/Hg_2Cl_2/KCl$ (saturated in water) and the silver-silver chloride electrode, $Ag/AgCl//KCl$ (saturated in water) are commonly used as reference electrodes due to SHE's inconvenience in experimental applications. Since the reference electrode has a constant makeup, its potential is fixed. Hence, any potential changes in the cell can be described by the working electrode.

In a typical electrodeposition, the reactant, which is dissolved in the electrolyte, is deposited as a solid product. Consequently, the activity of the reactant decreases as the reaction proceeds. The two important parameters to determine the route of electrochemical reaction are the deposition current and the cell potential. In the galvanostatic mode, the reaction is controlled by applied current leading to deposits with good adhesion and a controlled morphology. However, the cell potential drifts as the reactant activity decreases, leading to multiplicity of products. In the potentiostatic mode, the reaction is carried out by desired cell potential with respect to a reference electrode. Usually, the cell current decreases rapidly as the reaction proceeds due to low rates of diffusion of the reactant molecules to electrode as well as decrease in activity of the reactant. However, the reaction tends to produce a pure single phase product by the properly chosen potential.

Today, a three-electrode cell is commonly used instead of a two electrode cell (W_E and R_E) because of its accuracy for large scale cells with high resistive electrolytes. In this arrangement, a counter (or auxiliary) electrode (CE) is placed into the cell, and the current flows between the working electrode and the counter electrode (instead of the reference electrode in the case of the two-electrode cells). In order to avoid an interfering reaction at the working electrode, any convenient one, which does not produce substances by electrolysis, is chosen for the counter electrode. The reference electrode should be placed near the working electrode surface to minimize a loss of voltage drop in electrolyte between the working electrode and the reference electrode. The device used to observe the potential difference between a working electrode and a reference electrode generally has very high input impedance, so a negligible current flows through the reference electrode. Hence, its potential will remain constant and be equal to its open-circuit value.

II.1.1 Electrochemical experiments

1.1 Electrochemical set-up

In order to realize the main work of this thesis, a sophisticated experimental setup was used (Fig.II.1). It consists of an electrochemical cell with three electrodes connected and controlled by a Potentiostat / Galvanostat (PGZ301, Radiometer Analytical).

Figure II. 1: Schematic representation of the experimental device used for the elaboration of ZnS nanostructures.

1.2 Electrochemical cells and electrodes

The three electrodes used during our work are:

Reference electrode: this electrode is used to measure the potential applied to the working electrode. Which is a saturated calomel electrode (SCE: $Hg/Hg_2Cl_2/KCl$) where the standard potential in respect to the Normal Hydrogen Electrode at 25 ° C is equal to + 0.244 V/NHE.

Counter electrode: is a platinum plate (Pt).

Working electrode: ZnS nanostructures were deposited onto polycrystalline indium tin oxide (ITO) coated conducting glass substrate with an exposed area of 1×2 cm² with resistance (10 -20 Ω/cm² sheet resistance).

The surface of the samples were not activated and were cleaned following a standard procedure, i.e. the glass substrates were cleaned in common organic solvents in an ultrasonic bath. Acetone, Ethanol and distillate water are each used for 10 min. After deposition, the samples were rinsed with distillate water so as to eliminate salts present on their surface and dried in air.

1.3 Chemicals

The electrodeposition of ZnS nanostructures was carried out in an electrochemical cell with a capacity of 50 ml of sulfate bath. Bath composition composition (Bath1: used for the electrodeposition of ZnS at various zinc concentrations, Bath2: collect the bath composition of the two studied effects, cathodic deposition potential and time. While the 3rd Bath presented the chemical bath composition for the Sm and Er doped ZnS) and the experimental conditions used are described in the table below.

Table II. 1: Chemical bath compositions of the electrodeposition of ZnS *nanostructures* at various parameters.

Bath 1

[ZnSO$_4$] mol/l	[Na$_2$S$_2$O$_3$] mol/l	pH
10^{-4}	10^{-3}	2.7
10^{-3}	10^{-3}	2.7

Bath 2

[ZnSO$_4$] mol/l	[Na$_2$S$_2$O$_3$] mol/l	pH
10^{-4}	10^{-3}	2.7
10^{-4}	10^{-3}	2.4

Bath 3

[ZnSO$_4$] mol/l	[Na$_2$S$_2$O$_3$] mol/l	[ErCl$_3$] mol/l	[SmCl$_4$] mol/l	pH
10^{-4}	10^{-3}	10^{-7}	10^{-7}	2.4
		5×10^{-7}	5×10^{-7}	
		10^{-6}	10^{-6}	
		5×10^{-6}	5×10^{-6}	
		10^{-5}	10^{-5}	
		5×10^{-5}	5×10^{-5}	

II.1.2 Electrochemical techniques

1.2.1 Cyclic voltammetry (CV)

Cyclic voltammetry (CV) is a potentiodynamic electrochemical measurement used for the mechanistic study of redox systems in the electrochemical cell [35]. In CV, the voltage is linearly applied to the electrode with a given scan rate (20 mV/sec). During the negative (forward) scan, the current in the electrochemical cell increases when any solute in the electrochemical cell is reduced and reaches the peak, corresponding to the reduction potential of a given solute. Then the current decreases as the concentration of the solute is depleted close to the electrode surface. If the redox

couple is reversible, the product formed in the reduction process can be oxidized when the applied potential is reversed (backward).
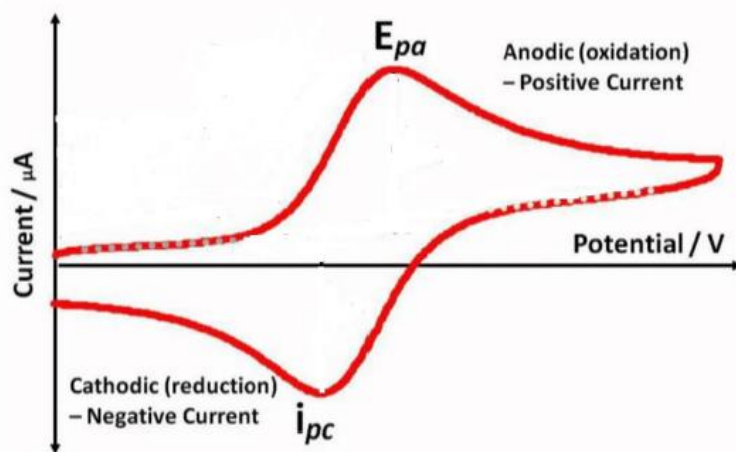
Figure II. 2: Typical cyclic voltammetry curve [82].

The reverse scan also produces a current peak, corresponding to the oxidation potential. The oxidation peak normally has a similar shape to the reduction peak and an opposite polarity to the reduction peak (Fig. II.2). As a result, information about the redox potential and the electrochemical reaction rates of the compounds can be obtained by CV.

1.2.2 Chronoamperometry (CA)

Chronoamperometry (Current-time transients) is very powerful method for the quantitative analysis of an electrodeposition process. This useful technique leads to obtain the initial information about nucleation and growth mechanism, thanks to theoretical models now well established [35]. Additionally, the amount of charge and deposition rate for the deposits can be determined. The recorded current can be analyzed and its nature can be identified from the variations with time. For example: at short times the capacitive current is dominant while at longer time scales, the diffusion limited faradaic current might prevail. Compared to cyclic voltammetry, the use of chronoamperometry is of capital importance in the case of complex processes with the formation of a new phase. It's interesting for the study of the electrochemical formation of semiconductor deposits.

1.2.3 Mott-Schottky Analysis (M-S)

Among other methods, capacitance-potential (C-E) measurements are often used to determine the carrier concentration of undoped and doped semiconductor. The C-E technique used the dependency between the space-charge region (SCR) width of a semiconductor junction and the applied reverse-biased potential. The SCR required in the method is formed when a suitable electrode is connected to the semiconductor, so that a Schottky barrier contact forms. A Schottky barrier contact

with the semiconductor can be achieved for example with a deposited metal electrode or a liquid electrolyte contact [83].

One way to determine the carrier concentration N_D and the flat band potential E_{fb}, based on C-E measurements, is to perform the Mott-Schottky (M-S) analysis. In the M-S analysis, the carrier concentration was calculated from the following expression [84]:

$$\frac{1}{C^2} = \frac{2}{\varepsilon \varepsilon_0 q A^2 N_D}\left[(E - E_{fb}) - \frac{KT}{q}\right]$$ (Eq II.1)

In this equation, **C** represents the interfacial capacitance, **ε** is the dielectric constant of ZnS **ε**= 8.1[85], A is the exposed electrode area (1 cm^2), **ε$_0$** is the permittivity of free space (8.85×10^{-14} F/cm), **k** is the Boltzmann constant (1.38×10^{-23} J/K), **N$_D$** is the number density (cm^{-3}) of donor in ZnS, E is the applied potential, **E$_{fb}$** is the flat band potential, **T** is the room temperature (298 K), and **e** is the elementary electron charge (1.6021×10^{-19}C). The extrapolating on x axis give the potential flat band values as indicated in Figure II. 3.
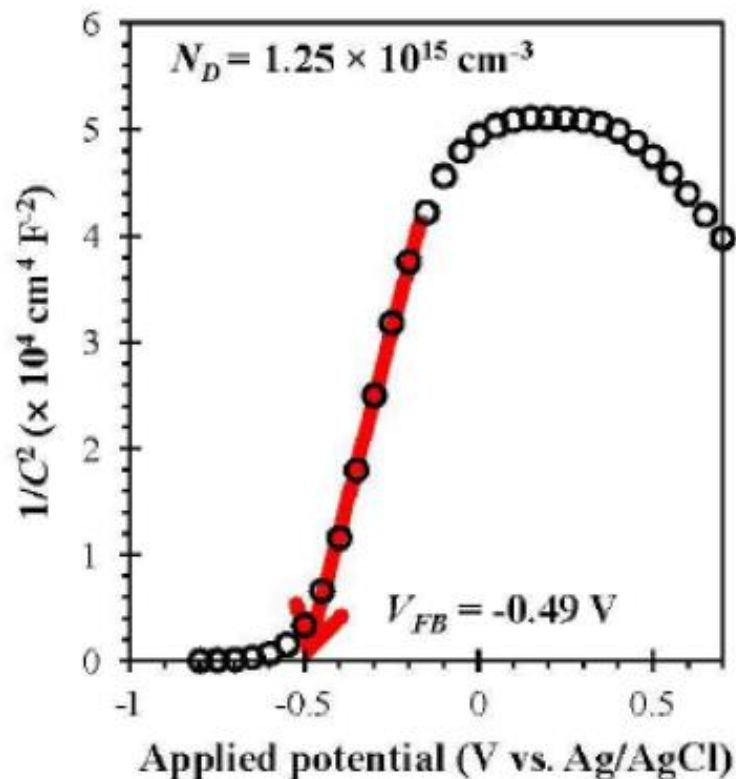
Figure II. 3: *A typical Mott-Schottky plot of an n-type semiconductor* [82].

II.2 Characterizations techniques

2.1. Thickness measurements

Along with ZnS/ITO/glass substrates, the samples are placed in the holder. A part of these samples are masked with Teflon during the deposition to create a step in the deposited film. Film thickness is measured by moving the tip of a Tencor (AltiSurf 500) profilometer (Fig. II.7) across the step in different areas. An average of the values is taken as the film thickness [85].

Figure II. 4: *Photograph of Profilometer AltiSurf 500.*

2.2 Atomic force microscopy (AFM)

Atomic force microscopy is a convenient technique to study the morphological characteristics and surface roughness of semiconductor nanostructures and to observe nanostructures of nanostructures. It is well known that AFM is one of the most effective ways for the surface analysis due to its high resolution and powerful analysis software. Asylum research (MFP-3DSPM) AFM (Fig. II.5) was used for the topography (3D images) and surface roughness along with grain sizes (2D images) of the obtained nanostructures.

Figure II. 5: *Photograph of Atomic force microscopy.*

2.3 Scanning electron microscopy (SEM)

The SEM's principle component is a finely focused electron beam scanned across the surface of the sample generates secondary electrons, backscattered electrons, and characteristic X-rays. The SEM's primary imaging method is through the collection of those secondary electrons (or backscattered electrons) that are released by the sample. These backscattered electrons are detected by a scintillation material, which is a radiation detector that produces flashes of light from the electrons. The light flashes are then detected and amplified by a photomultiplier tube. These signals are collected by detectors to form images of the sample displayed on a cathode ray tube screen [86].

Figure II. 6: *Photograph of Scanning Electron Microscopy.*

While SEM used as image of structure, size of grain and distribution. Especially, the thicknesses of nanostructures were measured by SEM. In order to avoid charging effect caused by secondary

electrons-- black rectangles phenomenon. Morphologies were observed by SEM at an acceleration voltage of 10 kV, probe current of 6×10^{-10} Amp. The samples were measured in 7800F, JEOL SEM equipment (Fig. II.6).

2.4 X-ray diffraction (XRD)

In principal XRD measurement come down to measuring distances between planes with plane x-ray waves. When the bragg condition nλ=2d×sinθ is satisfied and a peak will be measured [86]. The result of an XRD measurement is a diffractogram, showing phase present, phase concentrations (peak heights), amorphous content (background hump) and crystallite size/strain (peak widths). The structure of the ZnS is studied with wide-angle x-ray diffraction. X-Ray diffraction is a versatile, non-destructive analytical technique for identification and quantitative determination of the various crystalline forms (phase), of compounds present in powdered and solid samples. Identification is achieved by comparing the X-ray diffraction pattern or "diffractogram" obtained from an unknown sample with an internationally recognized database containing reference patterns for more than 70,000 phases. Moden computer-controlled diffractometer systems use automatic routines to measure, record and interpret the unique diffractograms produced by individual constituents in even highly complex mixtures. XRD used as analysis of chemical composition, relative percentage of phase and orientation. Samples were carried out using XRD with 50 kV and 40 mA, Cu Kα radiation, λ= 1.5406. A crystal lattice is a regular three-dimensional distribution (cubic, rhombic, etc.) of atoms in space. These are arranged so that they form a series of parallel planes separated from one another by a distance d, which varies according to the nature of the material. For any crystal, planes exist in a number of different orientations-each with its own specific d-spacing. When a monochromatic X-Ray beam with wavelength λ is incident on lattice planes in a crystal at an angle θ, diffraction occurs only when the distance traveled by the rays reflected from successive planes differs by a complete number n of wavelengths. By varying the angle θ, the Bragg's law conditions are satisfied by different d-spacings in polycrystalline materials, plotting the angular positions and intensities of the resultant diffraction peaks produces a pattern which is characteristic of the sample, where a mixture of different phases in present, the diffractogram is formed by addition of the individual patterns

Furthermore, the average crystallites size was calculated using Debye Scherer's Formula [35]:

$$D = \frac{0.94\,\lambda}{\beta\cos\theta} \tag{Eq.II.2}$$

D is crystallites size, λ is the wavelength of the X-ray (1.5456 A), β is the full width half maximum of the diffraction peak in radians and θ is Bragg diffraction angle. The lattice parameter a was calculated from [87]:

$$a = d_{hkl}\sqrt{h^2 + k^2 + l^2} \tag{Eq.II.3}$$

d_{hkl} is interplanar distance and (h k l) is Miller index. The microstrain ε was also estimated using the following formula[88]:

$$\varepsilon = \frac{\beta \cos(\theta)}{4} \qquad\qquad \text{(Eq. II.4)}$$

2. 5 UV-Visible spectrophotometer

The optical properties of the obtained films were studied using V-670 UV-Visible-NIR spectrophotometer.

Figure II. 7: V-670 UV-Visible-NIR spectrophotometer.

The optical band gap, disorder (Urbach energy), Steepness coefficient and the absorption coefficient was also measured using the giving expression:

- *Beer-Lambert law* was used to calculate the absorption coefficient (α) from the following expression:

$$\alpha = -(\frac{1}{d})\ln(\frac{100}{T}) \qquad\qquad \text{(Eq.II.5)}$$

  Where α is absorption coefficient, d is the film thickness and T is the transmittance.

- *The optical band gap (E_g)*: the band gap of the films was determined as the variation of *$(\alpha h\upsilon)^2$* versus (*$h\upsilon$*), the linear nature of the graph indicates the existence of direct transition. The values of E_g are evaluated from the intercept of the straight-line portion at the horizontal axis (α=0) from Tauc relation [89]:

$$(\alpha h\upsilon)^{1/n} = A(h\upsilon - E_g) \qquad\qquad \text{(Eq.II.6)}$$

  Where A is a constant, *$h\upsilon$* is the photon energy, α is the absorption coefficient and depends on the nature of the transition, being = 1/2 for direct transitions.

- We have used the *Urbach Tail (Eu)* as a signature of the disorder, which is related to the disorderin the film, given by the relation [89]:

$$\alpha = \alpha_0 e^{-(\frac{h\nu}{Eu})}$$ (Eq.II.7)

α_0 is the pre-exponential factor, hυ the photon energy and *Eu* is the Urbach tail (disorder energy). Eu can be estimated from the inverse slope of the linear plot of ln (α) versus *hυ.*

2. 6 Time Resolved Photoluminescence

The photoluminescence lifetime was obtained by using time-correlated single-photon counting (TCSPC, DeltaFlex, Horiba Scientific) system. A delta diode with an excitation source of 319 nm, and a 60 picosecond photon detection module (PPD-650) (Fig. II.8) were utilized to measure the photoluminescence lifetime [90].
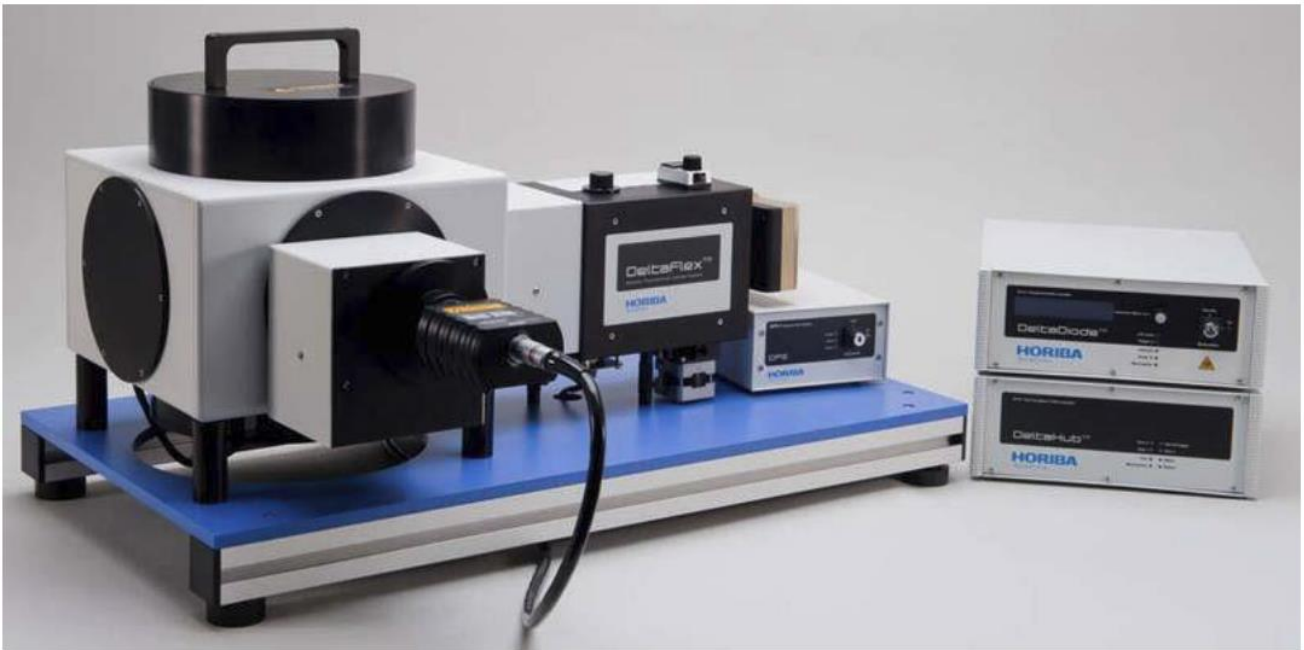
Figure II. 8: *Photograph of Time-resolved photoluminescence (TRPL).*

Time-resolved photoluminescence (TRPL) decay curves of the obtained samples can be well-fitted to a bi-exponential function described by the following equation:

$$F(t) = B_1 e^{(\frac{-t}{\tau_1})} + B_2 e^{(\frac{-t}{\tau_2})}$$ (Eq.II.7)

Where τ_1 and τ_2 represent the shorter and longer lifetime, respectively, and B_1, B_2 is the amplitude of the components.

II.3 Summary

This chapter summarized the experimental conditions and the different characterization techniques used during this work. The electrochemical techniques were used to study the kinetics of the electrodeposited ZnS nanostructures. Followed by the "Ex-situ" characterization methods namely AFM, SEM, XRD, UV-Vis and TRPL are used to characterize the obtained ZnS nanostructures.

In the rest of this work, a detailed study of the different parameters (zinc concentration, pH, potential and deposition time) to optimise ZnS electrochemical deposition study on the deposition of ZnS nanostructures is performed in an electrolytic bath on an ITO substrate.

Chapter III

Growth and optimization of ZnS by electrodeposition

Chapter III Growth and optimization of ZnS by electrodeposition

Chapter III Growth and optimization of ZnS by electrodeposition

It should be noted that an electrode reaction will not be only controlled by a single parameter but, by many other factors, which lead to a large number of trials to optimize the process, keeping in view the product quality. In this chapter, we present the electrochemical, morphological, structural and optical characterizations of the samples carried out in order to study the influence of the preparation conditions such as: zinc sulfate concentration, bath pH, applied potential and deposition time.

III.1 Influence of zinc precursor concentration

In order to identify the effect of the zinc precursor concentration on the electrochemical mechanism of ZnS, several results were presented.

1.1 Electrochemical reaction

In our experiments, ZnS nanostructures were deposited cathodically on ITO glass substrate from zinc sulfate solutions. The general scheme of the electrodeposited ZnS nanostructures from sulfate baths is supposed as follows (Fig. III.1).

The reduction of thiosulfate ions generated the sulfur formation on the cathode as well as the acidic medium enhanced this reaction. Sulfur formation was presented in the following reaction [36]:

$$S_2O_3^{2-} + 6H^+ + 4e^- \rightarrow 2S + 3H_2O \qquad \text{(III.1)}$$

Also, Zinc ions are reduced on the ITO surface to the formation of ZnS nanostructure according to the following reactions [91];

$$Zn^{+2} + 2e^- \rightarrow Zn \qquad \text{(III.2)}$$

$$Zn + S \rightarrow ZnS \qquad \text{(III.3)}$$

The electrochemical mechanism of the electrodeposited ZnS from a sulfate solution was clearly described in the figure III. 1.
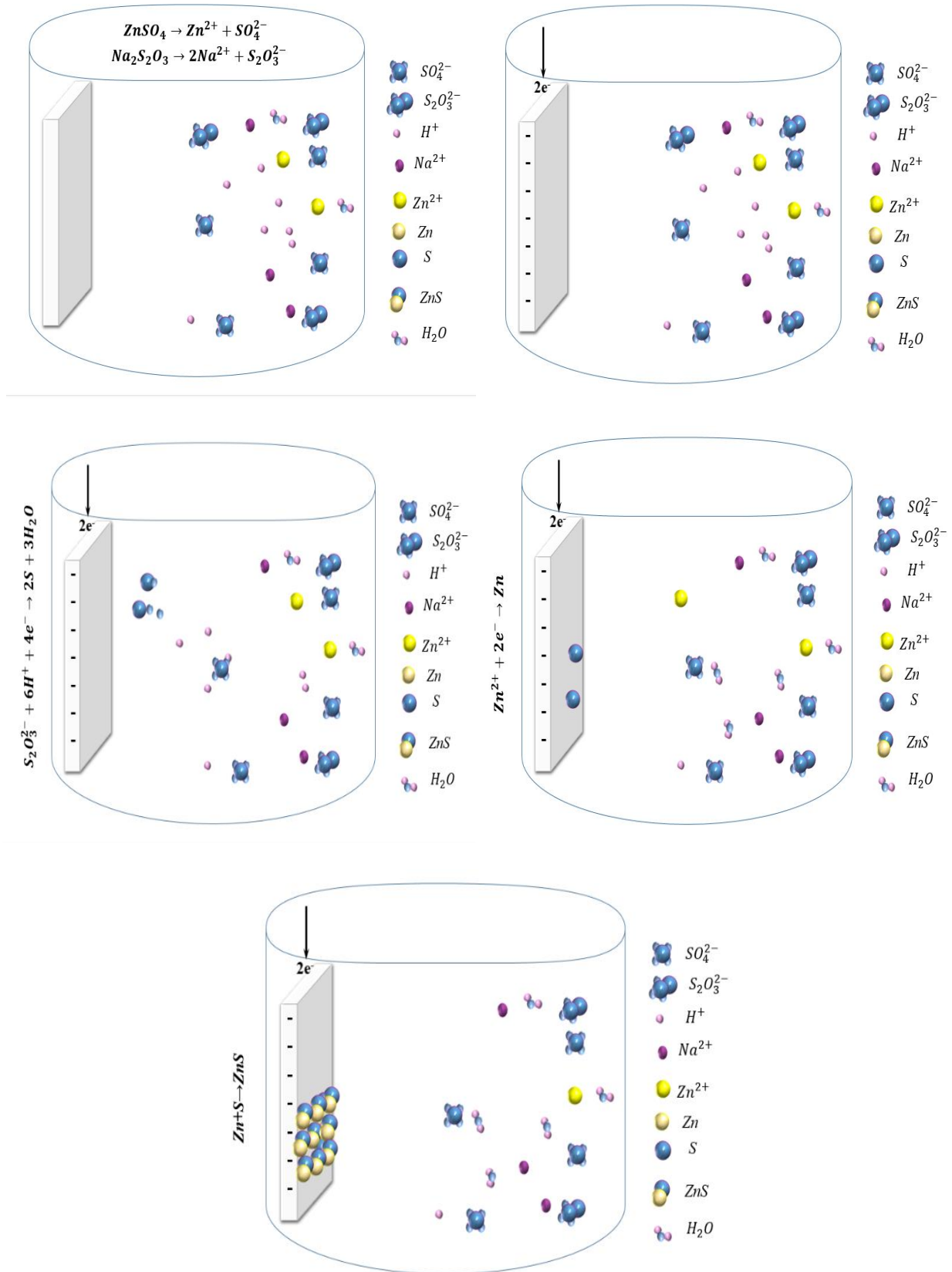
Figure III. 1: Schematic of the ZnS nanostructures electrodeposited on ITO glass substrate from a sulfate bath [92].

In order to study the electrochemical mechanism of ZnS nanostructures obtained on the ITO glass substrate at various $ZnSO_4$ concentrations (0, 10^{-3} and 10^{-4} M), cyclic voltammetry was used and the recorded voltammograms were presented in the figure III. 1. The potential range was varied between 0.2 and -1.4 V vs. SCE, bath temperature, pH and scan rate were fixed at 25 °C, 2.7 and 20 mV vs. SCE, respectively. Firstly, cyclic voltammetry of an aqueous bath of $Na_2S_2O_3$ was studied to give information about the cathodic reaction mechanism at the working electrode. In the absence of the Zn^{2+} ions, a small pic was observed in the range of -0.7 to -0.9 V attributed to the reduction of thiosulfate (Reaction 1), followed by a brutal drop in current due to the hydrogen evolution (H_2) produced by the reduction of water according to the reaction.

$$2H^+ + 2e^- \rightarrow H_2 \qquad\qquad\qquad (Eq.III.4)$$
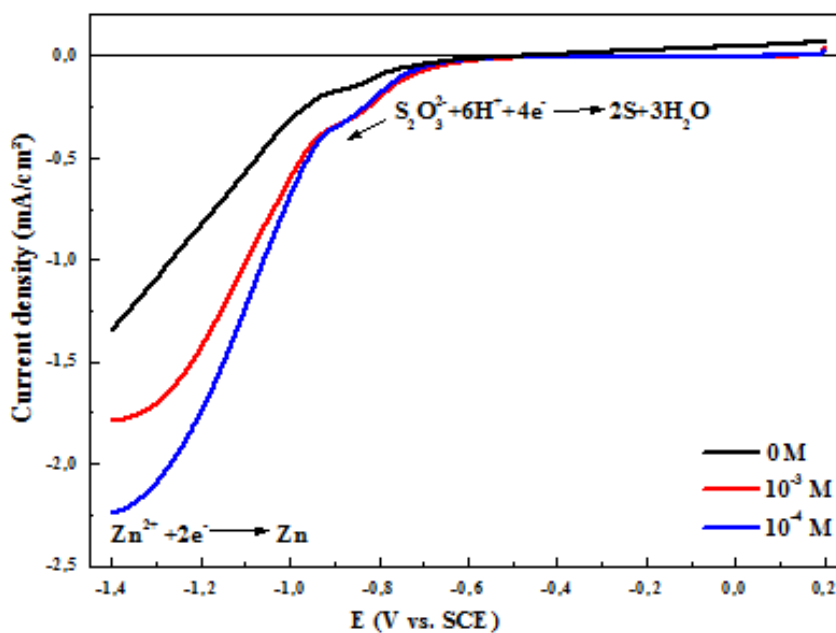
Figure III. 2: Cyclic Voltammetry of aqueous solutions containing 10^{-3} M $Na_2S_2O_3$ with different concentration of $ZnSO_4$

In the presence of various Zn amounts, the cathodic peak potential of the thiosulfate reduction shifted towards less negative values as the Zn concentration of the solution varied from 10^{-3} to 10^{-4} M. In addition, there is a simultaneously and relatively sharp increase of the cathodic current, this phenomenon implies the catalytic role of Zn^{2+} to the reduction of thiosulfate. A second peak was observed in the range of -1 to -1.4 V related to the reduction of Zn^{2+} ions to the Zn metallic. An increase of the cathodic current was observed when the $ZnSO_4$ concentration was varied from 10^{-3} to 10^{-4} M. No major changes can be easily observed in the voltammograms with varying zinc concentration.

For the cyclic voltammetry experiments, we have chosen the cathodic potential for the formation of ZnS nanostructures. This last was elaborated at different zinc concentration with potenstiostatic mod by imposing a cathodic potential of -1.2 V vs. SCE to the working electrode (which is our substrate ITO) for a duration of 5 min. A typical transient of an electrochemical process of three-dimensional nucleation-growth (3D) under diffusional control are characterized by a rapid decrease in current which corresponds to the charge of the double layer at the working electrode/electrolyte interface, and the time required for the formation of the first deposited nuclei on the surface [35]. Then, the current increases in proportionally until reaching a maximum i_{max} for a time equal to t_{max}. This is due to the growth of these nuclei and their recoveries [84]. Then the current decreases to a limit which is imposed by the diffusion of ions through the solution to the surface of the electrode.
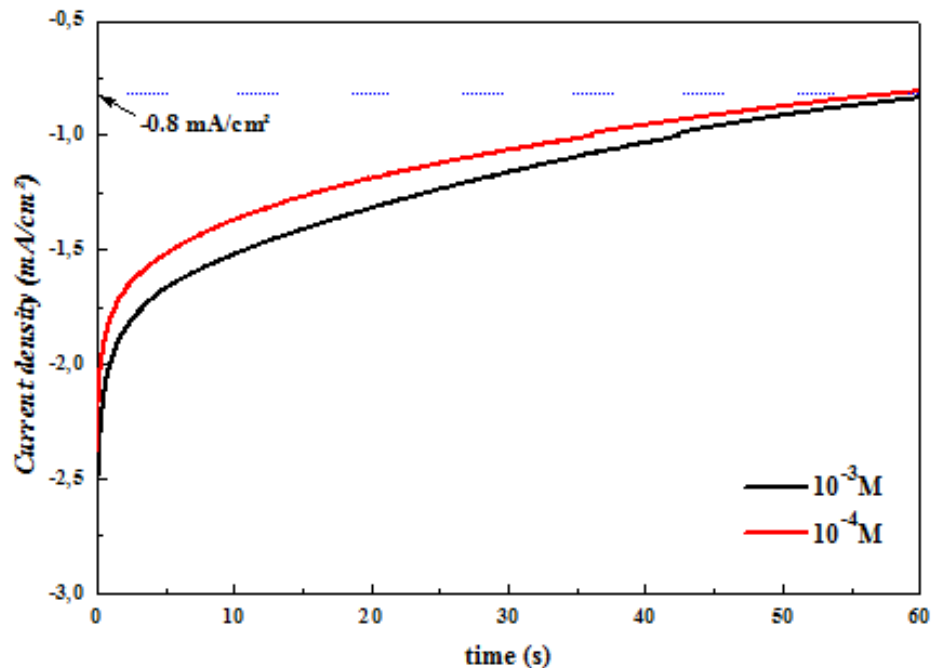
Figure III. 3: Experimental current transients of the electrodeposited ZnS on ITO at two concentration of $ZnSO_4$.

Figure III. 3 presents the chronoamperometric curves of the ZnS nanostructures electrode-posited at various concentrations. A current value close to -2.75 mA was measured at the initial stage of the experiment corresponding to the current of the electrodeposition of the ZnS nanostructures on the ITO glass substrate. After a few seconds, the cathodic current start increasing to reach a maximum value at –0.8 mA, in those curves we didn't observe the charge of the double layer at the beginning, because it's very fast. Also, it is noted from this figure that the current density increases in

proportionally with the variation of zinc ion concentration from 10^{-3} to 10^{-4} M, due to the increase of the ionic conductivity.

1.2 Mott-Schottky measurements

Mott-Schottky (M-S) analysis was employed for our nanostructures to study the effect of Zinc concentrations on the carrier density (N_D) and the flat band potential (E_{fb}). Figure III. 4 presents an M-S plot for the obtained ZnS nanostructures in 0.5 M of Na_2SO_4 as a supporting electrolyte, the frequency was fixed at 800 Hz.
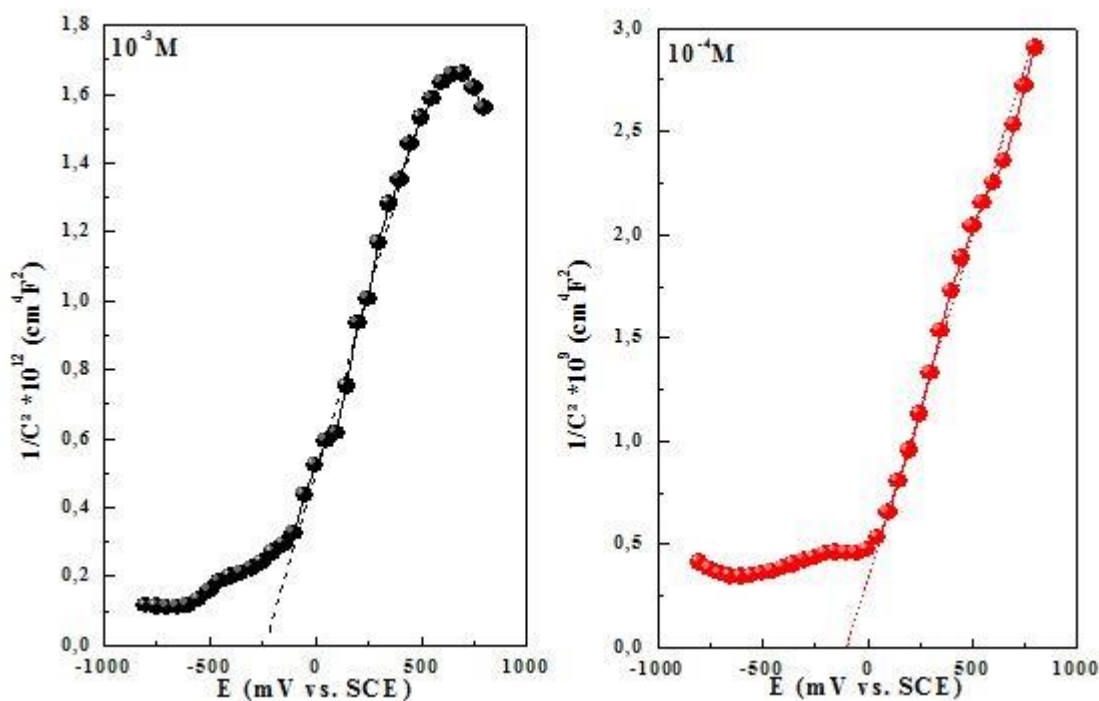
Figure III. 4: *Mott-Schottky plots of the ZnS nanostructures deposited at 10^{-3}M and 10^{-4}M of ZnSO$_4$ at 800 Hz.*

All samples show positive slopes, indicating that those ZnS films are n-type semiconductors. The flat-band potential values obtained from the intercept at $1/C^2 = 0$ at various Zn concentrations are reported to be -0.268 and -0.12 V vs. SCE, respectively. The donor carrier concentrations N_D were calculated to be 10^{18} and 10^{21} cm^{-3} for the films deposited at 10^{-3} and 10^{-4} M of ZnSO$_4$, respectively. We observe that ZnS nanostructures prepared at 10^{-4} M exhibited higher donor density compared to ZnS prepared at 10^{-3} M. The presence of S-rich condition favor the formation of zinc antisites (Zn_S) which leads to an increase in the surface conductivity [93], [94].

1.3 Morphology analysis

In order to study the effect of the Zn^{2+} ions concentrations on the morphological properties of the electrodeposited ZnS nanostructures on ITO-coated glass substrate at room temperature, the surface morphology of all samples was analyzed using SEM (Fig. III.5). From those figures, it is clearly that the film morphology is strongly influenced by changing the $ZnSO_4$ concentration. The films deposited at high concentration of 10^{-3} M show different size and shape of grain and the polydispersed nature of the grain size could be due to an incomplete nucleation and particle growth rate. For the concentration of 10^{-4} M ($ZnSO_4$), SEM image reveal the uniform distribution of grains, the surface is partially covered by a coalescence of the grains to form relatively large aggregates with 3D growth (Fig. III.5).
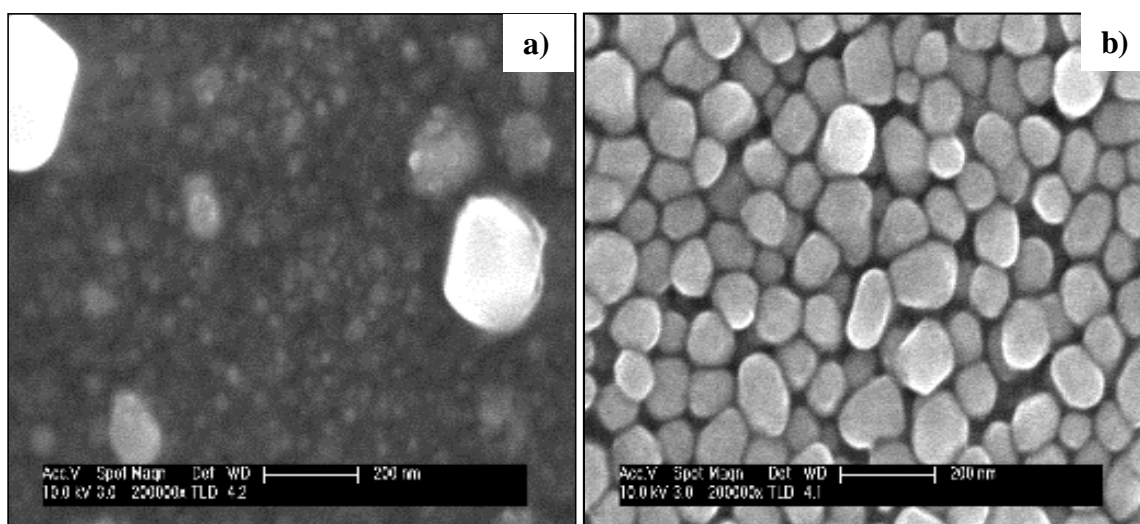
***Figure III. 5*:** SEM images of the electrodeposited ZnS *nanostructures* from an aqueous solution containing 10^{-3} M $Na_2S_3O_3$ with two $ZnSO_4$ concentrations: a) 10^{-3} and b) 10^{-4} M.

1.4 Structural characterisation

Figure III. 6 shows the XRD patterns of samples prepared at two concentration of $ZnSO_4$. It can be seen that the deposited film shows a (200) preferred orientation for zinc-blende phase of the ZnS nanostructures, the intensity of the (200) peak increase inversely with the concentration, It is very strong and it width at half maximum (FWHM) is small, indicating a good crystallization state with a large crystallites size. Hence the apparition of Zinc impurity at $2\theta = 35.74°$ and $39.39°$ correspond to (002) and (100) plan, respectively, is relative to low concentration of zinc sulfate [37]. While the samples deposited from aqueous solution containing 10^{-3} M $ZnSO_4$ show no presence of impurity, these results confirm that obtained by Mott-Schottky measurements.
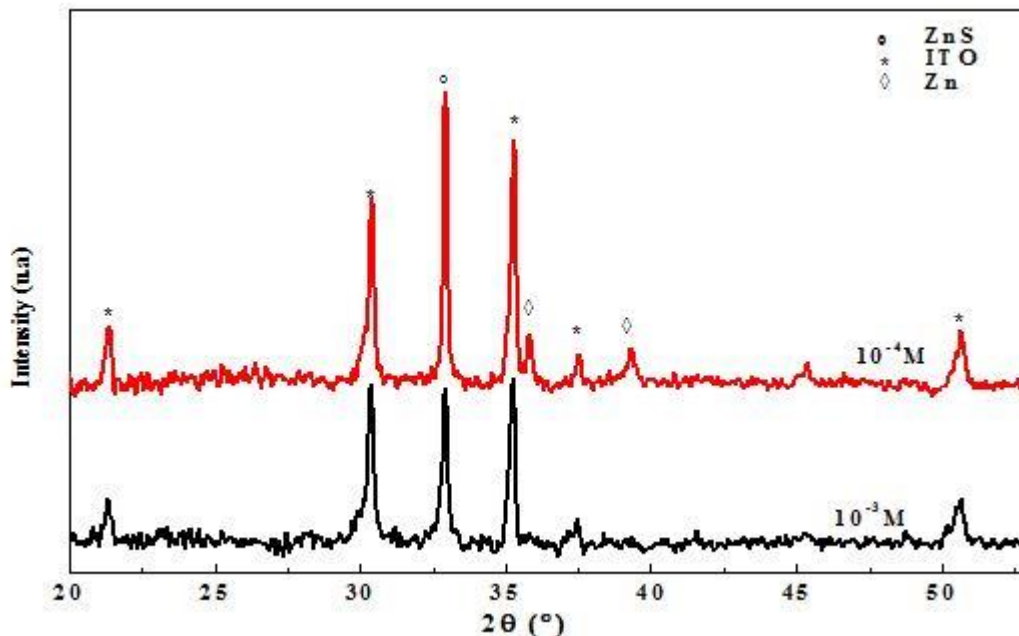
Figure III. 6 : *XRD patterns of the ZnS nanostructures electrodeposited on ITO substrates attwo concentration $10^{-3}M$ and $10^{-4}M$ of $ZnSO_4$.*

The average crystallites sizes (D) has been calculated using the Scherrer's formula (Eq.II.2) and the corresponding values were given in table III.1.

Table III. 1: *Crystallite size and lattice parameters of ZnS nanostructures electrodeposited at different Zn concentration.*

Zn concentration (M)	*2θ (°)*	*a (Å)*	*D (nm)*
10^{-4} M	32.91	5.43	63.48
10^{-3} M	32.93	5.43	93.55

It is quite clear that the average crystalline size of zinc sulfide increases with increasing molar concentration of Zn^{2+} in the electrolyte. In addition, the lattice parameters of the cubic structure has been computed as 5.43 Å, which is very close to the values obtained in the literature [95].

1.5 Optical properties

Transmittance spectrums of ZnS films with two different concentrations of $ZnSO_4$ recorded in the wavelength range from 250 to 800 nm was presented in the figure. III. 7. a. It is indicated that ZnS nanostructures exhibit a low transmittance value varied between 5 and 10 % in the visible range, which may be due to the presence of zinc in the films. These values are near to the values for ZnS derived from the electrochemical deposition process [14]. To improve the transparency of the obtained films, several parameters are going to be discussed.
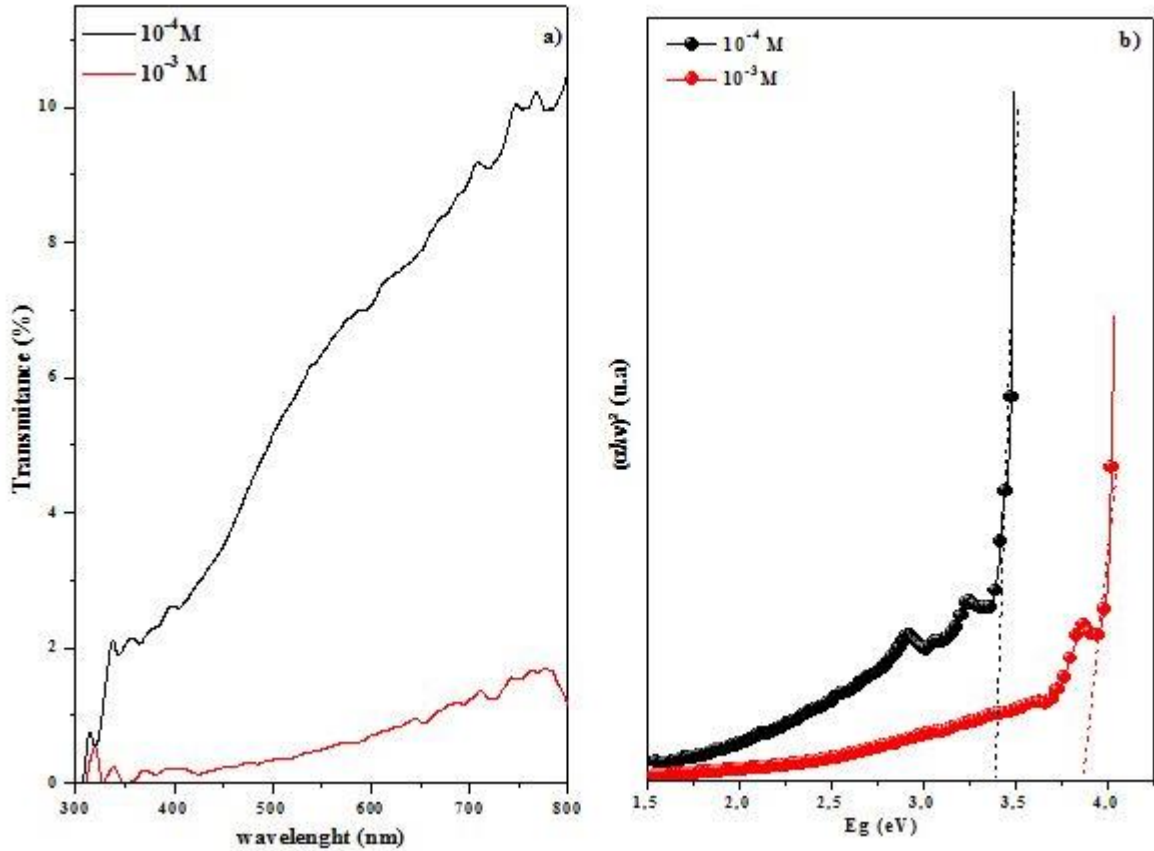
Figure III. 7: *a) Transmittance spectrum and b) (αhυ)^2 vs. energy dependence for the determination of the optical band gap energy of ZnS nanostructures on ITO-coated conducting glass surfaces obtained at two concentrations of ZnSO$_4$.*

The optical band gap (E$_g$) for ZnS nanostructures was evaluated by using the Tauc plot. The values of the optical band gap of ZnS layers are determined from the intercept of the straight-line portion at the horizontal axis when (αhυ)^2= 0 (Fig. III.7). the obtained E$_g$ was 3.40 and 3.85 eV for the films deposited from solution containing 10^{-3} and 10^{-4} M ZnSO$_4$, respectively. This augmentation in optical band gap is related to the defect presented in the obtained nanostructures.

III.2 Influence of pH solution

In electrodeposition, the bath pH can affect the conditions of metal and/or alloy deposition, which usually plays a key role to control the film properties. A modification of bath pH can also affect the structural, optical and morphological properties. Consequently, the electrolyte pH is one of the critical parameters to achieve the desired structural and functional properties.

2.1 Electrochemical studies

Cyclic voltammetry (CV) experiments were performed onto ITO coated glass substrates in 10^{-4} M ZnSO$_4$ and 10^{-3} M Na$_2$S$_2$O$_3$ solution for pH= 2.7 and pH= 2.4 versus calomel reference

electrode (ECS). The corresponding scans are represented in the figure. III. 8. The voltammograms of the two solutions was recorded at 25 °C in the potential range from 0.5 to -1.4 V vs. SCE, to study the reduced species in the solution. The followed reactions that could occur during the electrodeposition of ZnS were previously described.

The cathodic scan in CV measured a very small current with almost no change up to -0.6 V/ECS, as reported for the effect of Zn concentration two reduction peaks were obtained related to the reduction of thiosulfate and zinc ions, respectively. In the present study as presented in figure. III. 8 the reduction peak of thiosulfate for the pH 2.7 is smaller than that of 2.4, as presented in the reaction (III.1), the reduction of thiosulfate ions to sulfur need more much H^+ ions, that mean that when we decrease the pH values we favor the formation of S. While the Zn reduction peak shift to the negative direction when the pH, reduce from 2.7 to 2.4, this shift was also observed by U. Priyanka et al. [96], attributed to the variation in open circuits potential. The plateau region could be suitable for the electrodeposition of Zn which is further expected to react with sulfur present in the electrolyte. A large cathodic current measured for lower pH (2.4) is associated with the availability of more H^+ ions in the bath.
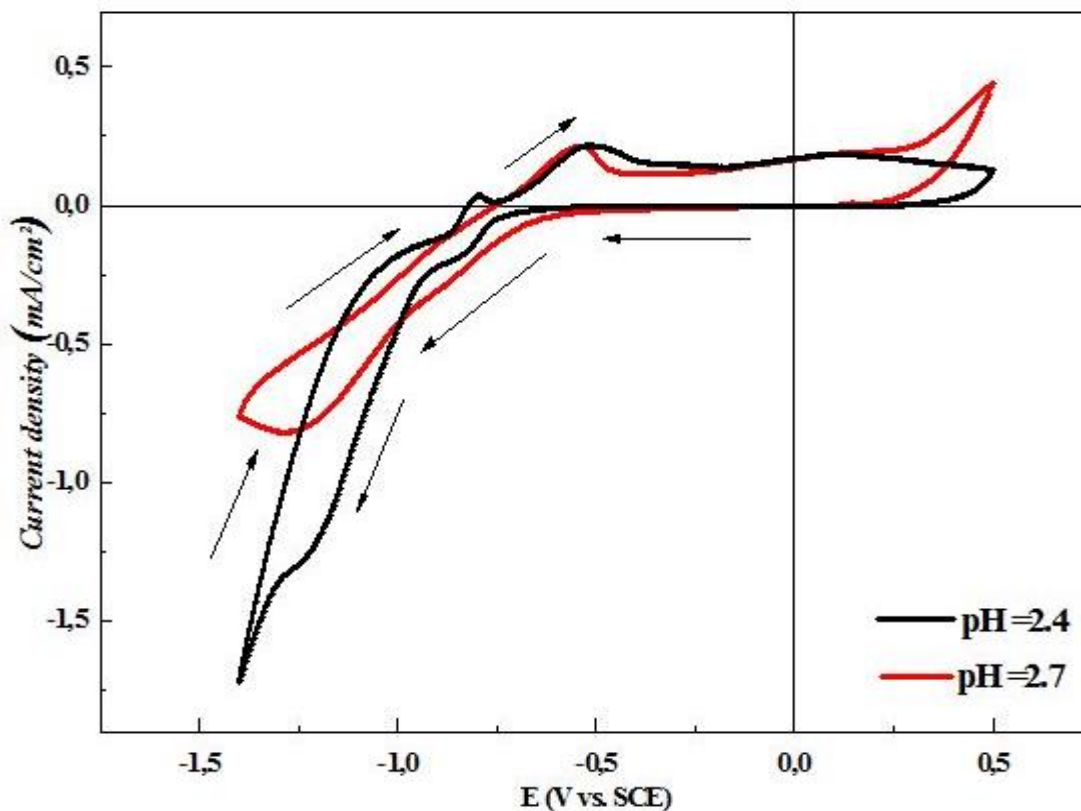
Figure III. 8: Cyclic Voltammetry for the aqueous solutions containing 10^{-3} M $Na_2S_2O_3$ and 10^{-4}M $ZnSO_4$ at two values of pH: 2.4 and 2.7.

The steep rise in cathodic current observed beyond -0.95 V may be due to the over potential deposition of Zn. Since the reduction potential for Zn is -0.76 V vs NHE [97], therefore, metallic Zn is expected to deposit at -1.0 V vs ECS by the reaction (III.2).

The obtained films were deposited by Chronoamperometry at two different pH 2.4 and 2.7, for an applied potential of -1.2 V during 5 min. Figure III. 9 shows the chronoamperometric transient curves recorded during ZnS growth under different bath pH. The current density was found to be increased by increasing the pH of electrolyte indicates the diffusion controlled mechanism dominating over the charge-transfer-controlled process.
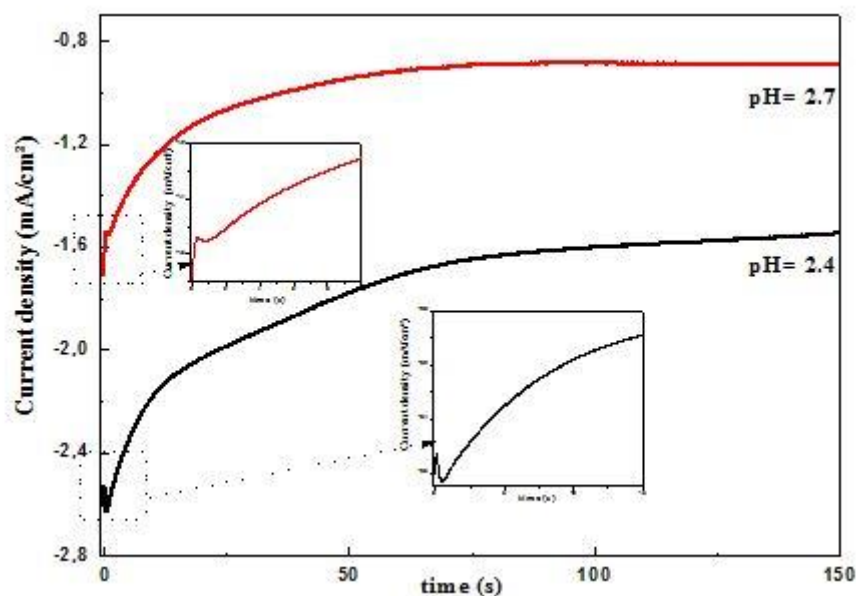
Figure III. 9: *i-t curves of ZnS nanostructures electrodeposited at two values pH: 2.4 and 2.7.*

In figure III. 9, initially for few seconds the cathodic current decays rapidly and subsequently increases. A sharp peak exhibited for pH equal to 2.4 of the bath is proposed due to the nucleation process. However, the broad peak observed for higher pH of the bath could be associated with the mixed nucleation processes. The mixed type of nucleation proposed for high pH value is due to the change of conductivity of the electrolyte which, depending on the formation of proton (H$^+$). The appeared peak in short time at lower pH~2.4 suggests the growth of small size particles.

2.2 Mott-Schottky measurements

The properties of electrodeposited nanostructures can be obtained by examining electronic structures of the semiconductor/solution interface, it is clear from the data presented in figure III. 10 that Mott-Schottky equation is valid within a wide potential range of about 1.6 V, which indicates a well-defined electronic surface state of deposited films. Wider linear potential range, that exceeds 1

V, can be obtained only for high organized solids, namely single crystals [94]. Furthermore a positive slope is an indication of an n-type semiconductor.

At negative potentials (roughly for E< -0.4 V vs. SCE), a significant deviation from linearity is observed. This deviation is very likely related to the presence of surface states because an electronic structure change, as a result of the elementary zinc formation by reduction, would have decreased the depletion region capacitance dramatically. Accordingly, at lowest investigated potentials the reduction process corresponds to the sulfur reduction [94].
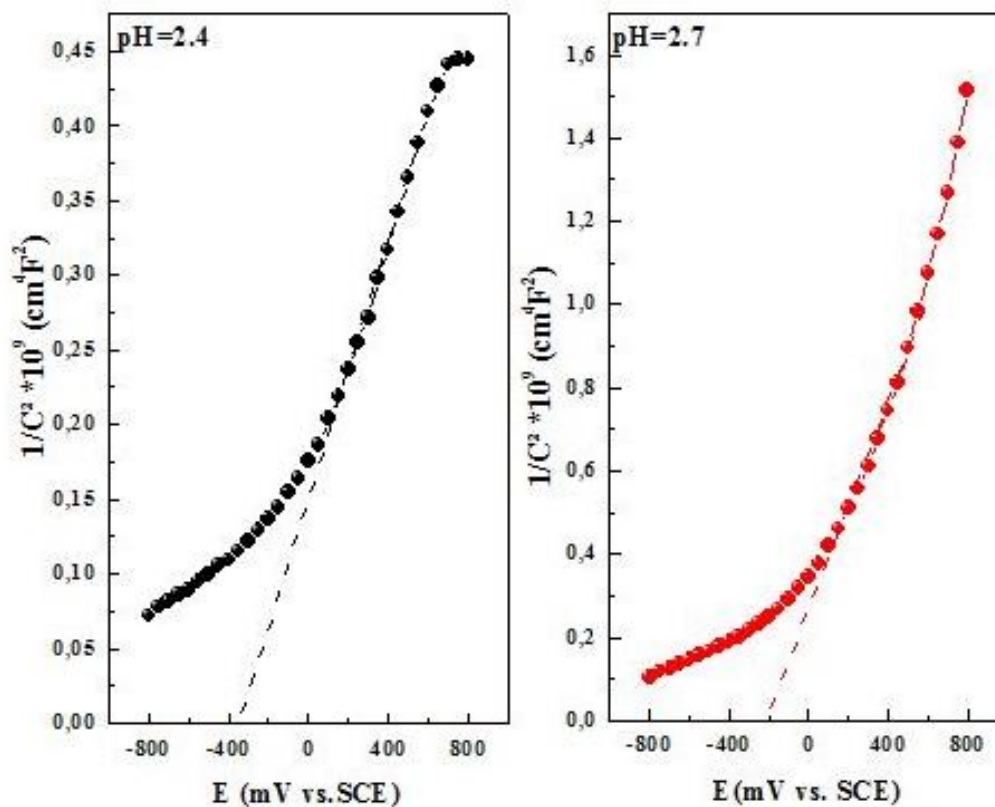
Figure III. 10: *Mott-Schottky plots of the ZnS nanostructures deposited at pH: a) 2.4 and b) 2.7.*

2.3 Morphology analysis

The morphology of the deposited ZnS nanostructures was observed using SEM technique. Figure III. 11 Shows the SEM images of the ZnS films electrodeposited from an aqueous solution containing 10^{-4} M $ZnSO_4$ and 10^{-3} M $Na_2S_2O_3$ at two values pH=2.4 and 2.7 during 5 min. A notable change in the grain size and shape was observed. The sample deposited at pH= 2.4 (Fig. III.11 a) show a random distribution of grain sizes with different shape. While the second sample shows a uniform distribution of grain on the surface of the substrate which is totally covered. The grains are orthogonal to the film surface indicating that the film grows perpendicular to the substrate.
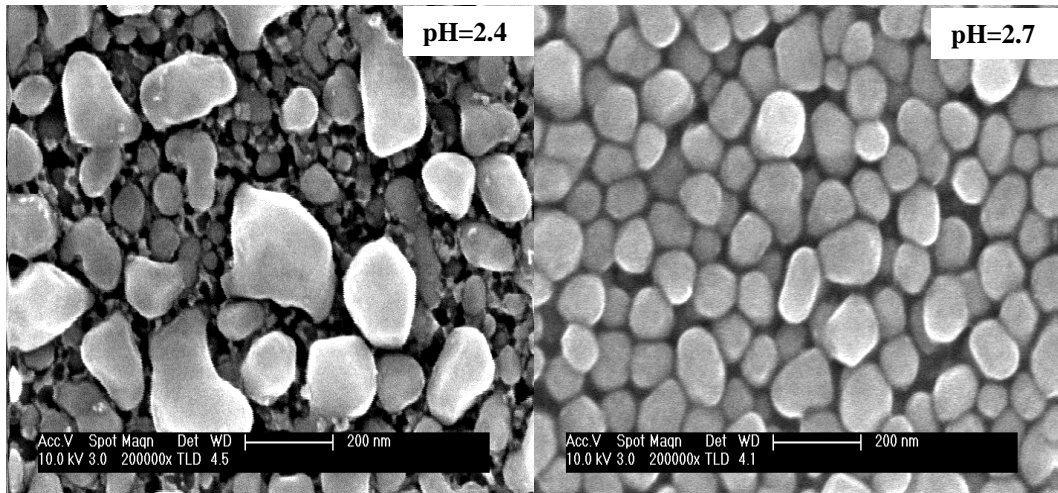
Figure III. 11: *SEM images of the films electrodeposited at values of pH 2.4 and 2.7.*

The atomic force microscopy (AFM) has also been proved to be a convenient method to determine the surface morphology of the films. Figure III. 11 shows AFM images (20×20 µm) of the ZnS nanostructures deposited at two different pH values. The nanostructures prepared at pH= 2.4 show homogenous and well-covered the surface of the substrate, with granular grains. A decrease of grain size for the pH= 2.7 is observed.
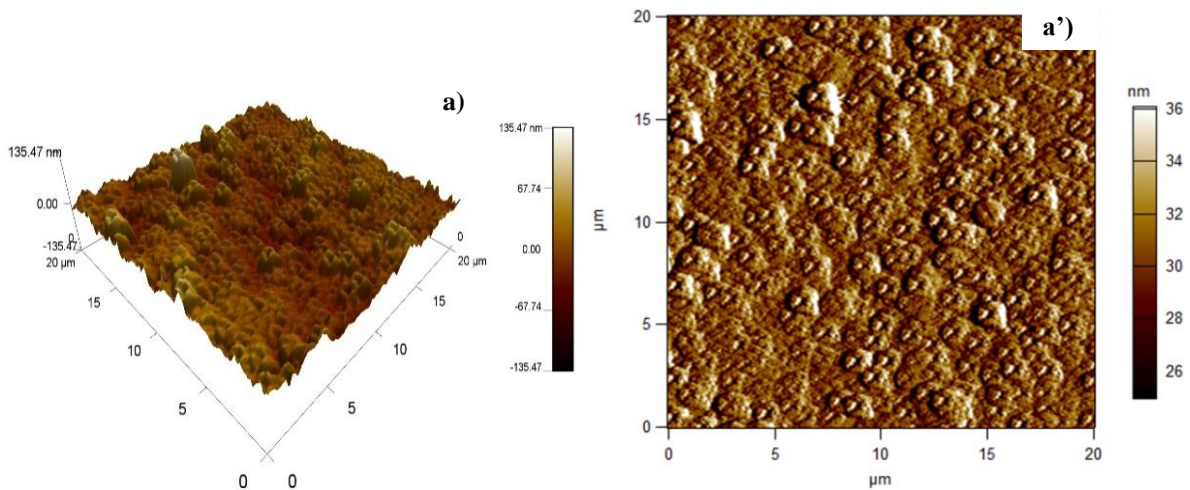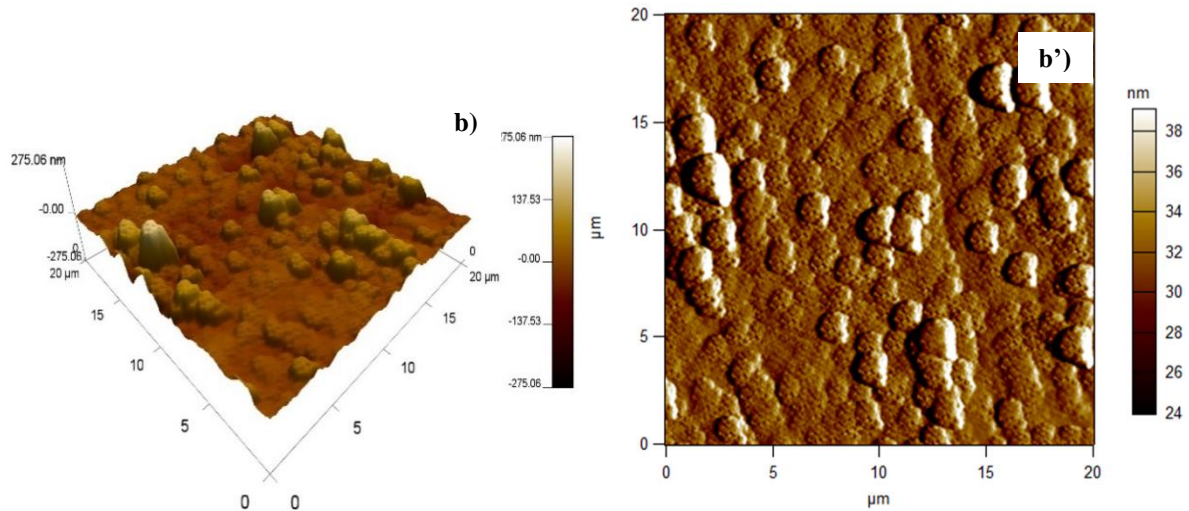
Figure III. 12: *2D and 3D atomic force microscopic images of ZnS nanostructures electrodeposited at two values pH: a), a') 2.4 and b), b') 2.7.*

The root mean square (RMS) was calculated using AFM images. We obtain 16.05 nm for pH~2.4 and 31.63 nm for pH~2.7.

2.4 Crystal Structure

The XRD patterns of the nanostructures prepared at two different pH are shown in figure III. 13, the films deposited exhibits a peak at 2θ= 32.94° and 2θ= 32.94° for the film deposited at pH 2.4 and 2.7, respectively, corresponding to (200) plan (JCPDS card file, 05-0566), the file confirms that our layer crystallized with cubic phase. An increase of the diffraction peak (200) was observed when the pH decreases from 2.7 to 2.4, which indicate an increase in grain size. Low intensity peaks was appeared attributed to S impurity for 2θ= 39.4° related to (310) plan and Zn impurity for 2θ= 35.87°, 54.23° related to (002), (102) respectively [36], [37]. The evaluated lattice parameters were a= 5.43 Å for pH~2.4 and 2.7, respectively.
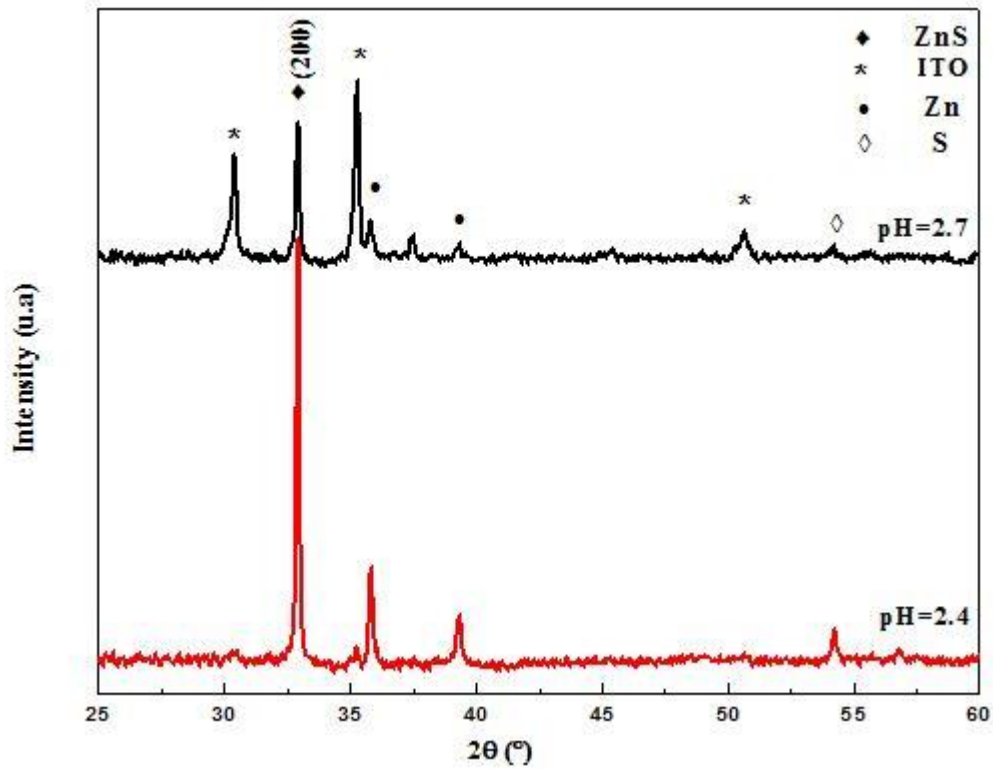
Figure III. 13 : *X-ray diffraction patterns of ZnS nanostructures electrodeposited at two values of pH 2.4 and 2.7.*

The crystallite size was about 115 nm and 96 nm for the samples deposited at pH~ 2.4 and 2.7, respectively. Those results are in good argument with that obtained in SEM and AFM.

Table III. 2: *Crystallite size and lattice parameters of ZnS nanostructures electrodeposited at pH ~2.4 and 2.7.*

pH	2θ (°)	d_{hkl}	a (Å)	D (nm)
2.4	32.941	2.7168	5.433	115.05
2.7	32.934	2.7173	5.434	96.36

III.3. Influence of the deposition potential

3.1 Determining the potential window

Figure III. 14 shows a typical cyclic voltammogram of an ITO electrode immersed in a sulfate bath containing 10^{-4} M $ZnSO_4$ and 10^{-3} M $Na_2S_2O_3$. These voltammograms were carried out at different potential range with a scanning speed of 20 mV/s recorded at room temperature. All the obtained voltammograms reveals two reductions peak, the first related to the reduction of thiosulfate ions and the second correspond to zinc ions reduction [98], [99]. The reduction of the thiosulfate ions is followed by a sharp fall in the current from -1 V, which is attributed to the hydrogen evolution (H_2), this one covered the reaction of reduction for Zn^{2+} ions to Zn metal. The increase in the potential range towards more cathodic values, lead to a strong evolution of H_2 due to the high acidity of the medium. According to figure III. 14, a rise in the reduction of thiosulfate ions was observed (increase in the reduction peak).
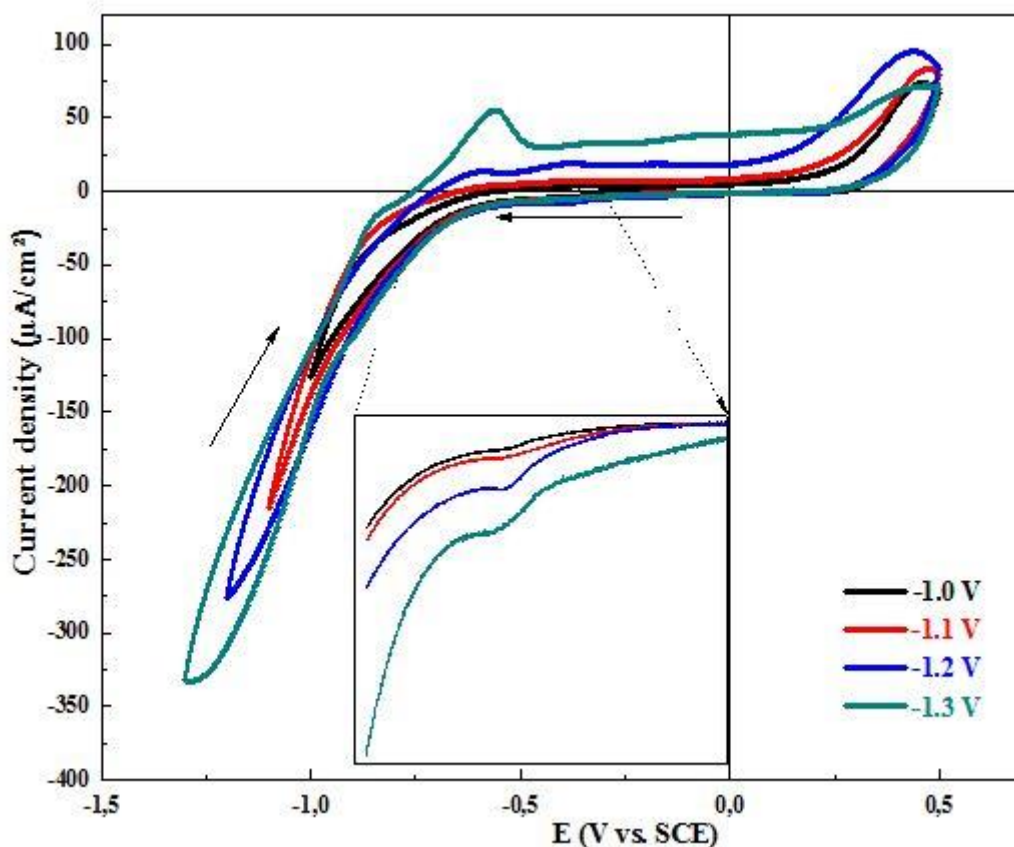
Figure III. 14: Cyclic Voltammetry for ITO substrate immerging in an aqueous solution containing 10^{-3} M $Na_2S_2O_3$ and 10^{-4} M $ZnSO_4$ at different potential range. Insert image represent the zoom of the reduction peak of thiosulfate.

At all potential values, the cathodic and anodic current density increased with increasing value of switching potential, which indicated that more ZnS were deposited in the cathodic region with a higher cathodic applied potential. In addition, these results are confirmed by experimental chronoamperometric.

Electrochemical deposition of ZnS was also carried out by chronoamperometry. Current-time transients at different applied potential were shown in Figure III. 15. The shape of the film growth curve can clearly indicate the nucleation-growth mechanism [100]. As seen from this figure, for a short time, a high cathodic current is observed, which corresponds to charging of the double layer, this is followed by an increase in current due to the growth of zinc sulfide on the electrode surface [101]. As the cathode potential is increased, the current also increases. The curves, current–time show also a strong dependence with the applied potential, an increase of the current density with the applied potential was observed which confirmed the cyclic voltammetry results.
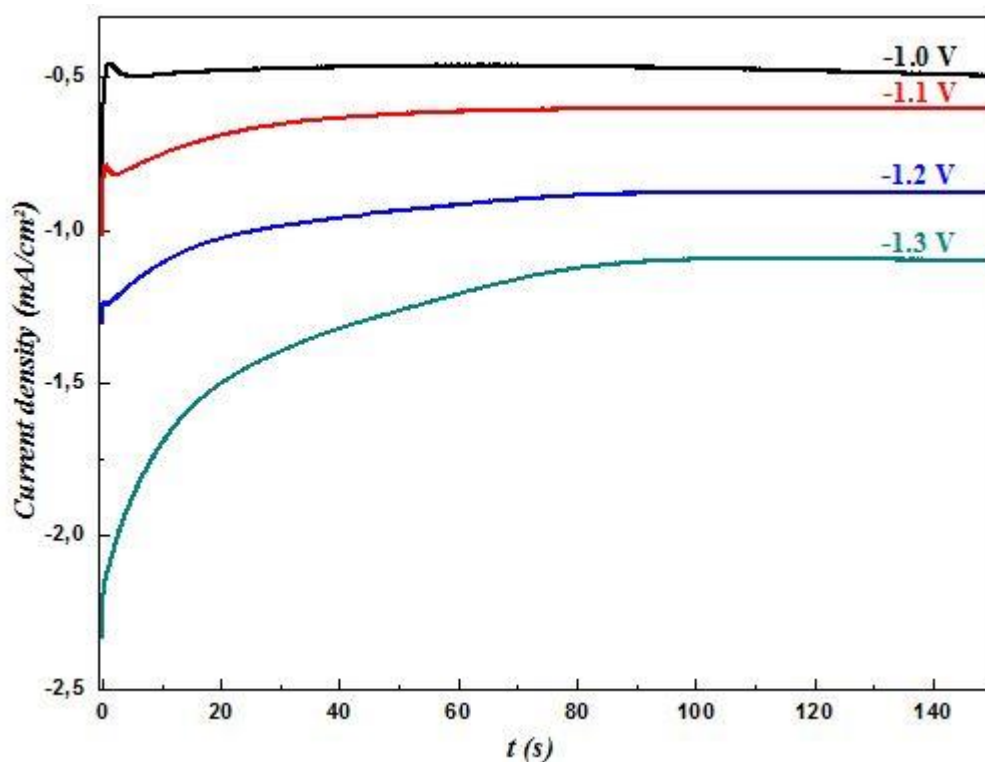
***Figure III. 15**: Experimental current transients recorded at different applied potentials for ZnS on ITO.*

3.2 Mott-Schottky measurements

In order to determine the effect of applied potential on the charge carrier density of the ZnS nanostructures, Mott-Schottky (M-S) analysis was performed. The $1/C^2$ versus E plots for the electrodeposited ZnS nanostructures obtained at a working frequency of 0.8 kHz. The positives

slopes for all samples indicate the n-type conductivity of the ZnS nanostructures. The flat band potential is found to shift from −0.699 V for films deposited at -1.0 V to -0.106 V for films deposited at -1.3 V. The shift to a more negative flat-band potential leads to some sort of surface or structural modification in ZnS nanostructures which was confirmed by XRD results. However, it is important to note that the shift of flat-band potential to positives values is also observed for ZnS nanostructures [102], [103]. Further study is required to understand this negative shift of flat band potential.
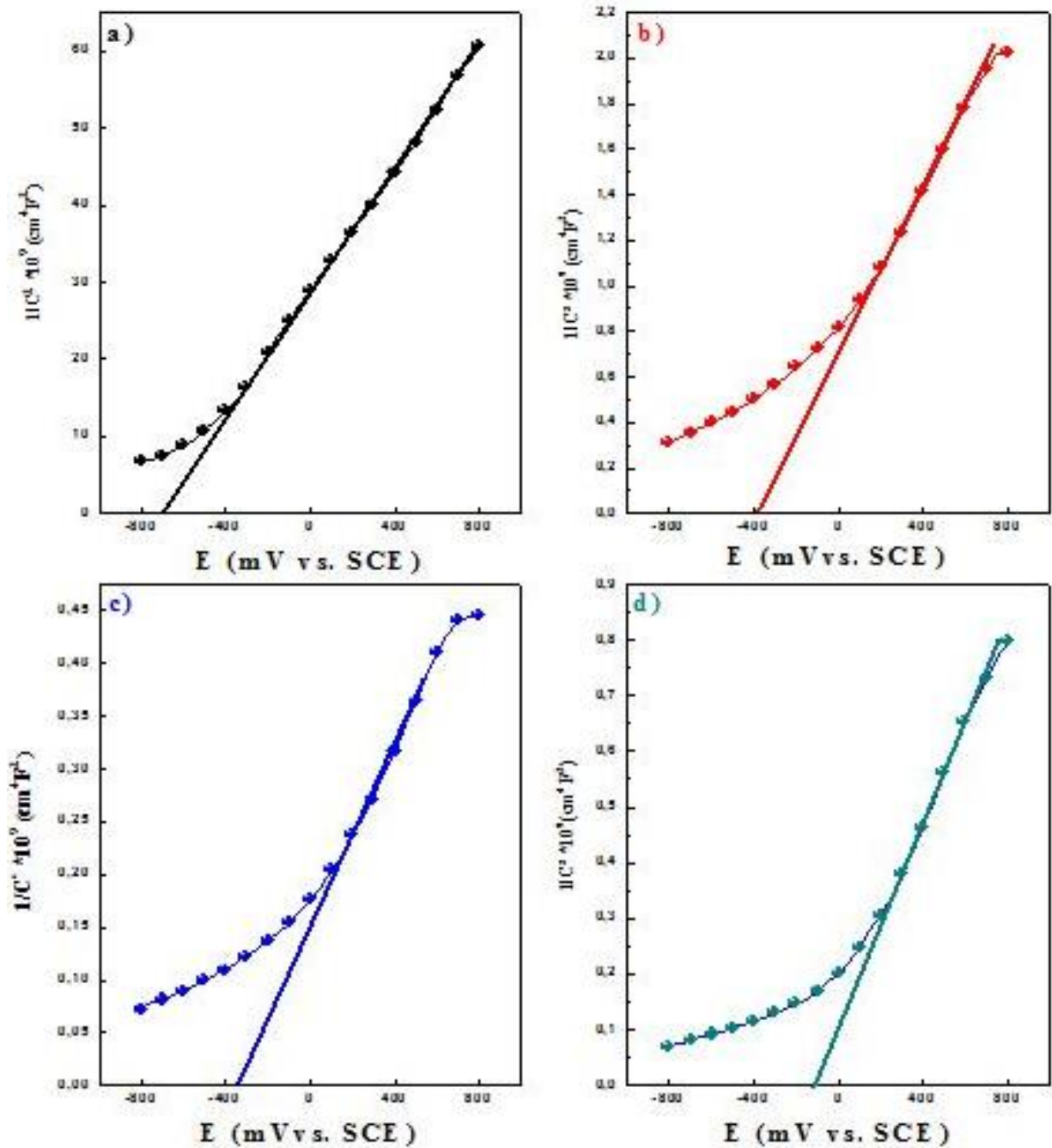
Figure III. 16: *Mott-Schottky plots of the ZnS nanostructures electrodeposited at a) -1, b) -1.1, c) -1.2 and d) -1.3V recorded at 0.8 kHz.*

The estimated of the charge carrier density of the ZnS nanostructures were found to be in the range of 4.33×10^{20} to 3.21×10^{22} cm^{-3}. It can be noticed that these values are two order of magnitude higher with more negative deposition potentials (Table III. 3).

Table III. 3: *Displays effect of applied potential on carrier density and optical band gap energy.*

E (V vs. SCE)	N_D (cm^{-3})	E_{fb} (V)
-1	4.33×10^{20}	-0.699
-1.1	9.80×10^{21}	-0.426
-1.2	2.47×10^{22}	-0.364
-1.3	3.21×10^{22}	-0.106

3.3 Morphology analysis

Surface morphology was determined through SEM and AFM images of the deposits. The observations by SEM indicate the film surface homogeneity and the shape of the grains and aggregates. SEM micrographs were taken for ZnS nanostructures deposited at different applied potential. However, the films deposited with lower precursor concentration are smoother. This can be related to the increase in film thicknesses, which, confirms the extinction of interference fringes in transmittance spectra.

The AFM images of the electrodeposits ZnS nanostructures are shown in figure III. 18. It was found that the crystallite size of the deposits was found in the nanometer range.
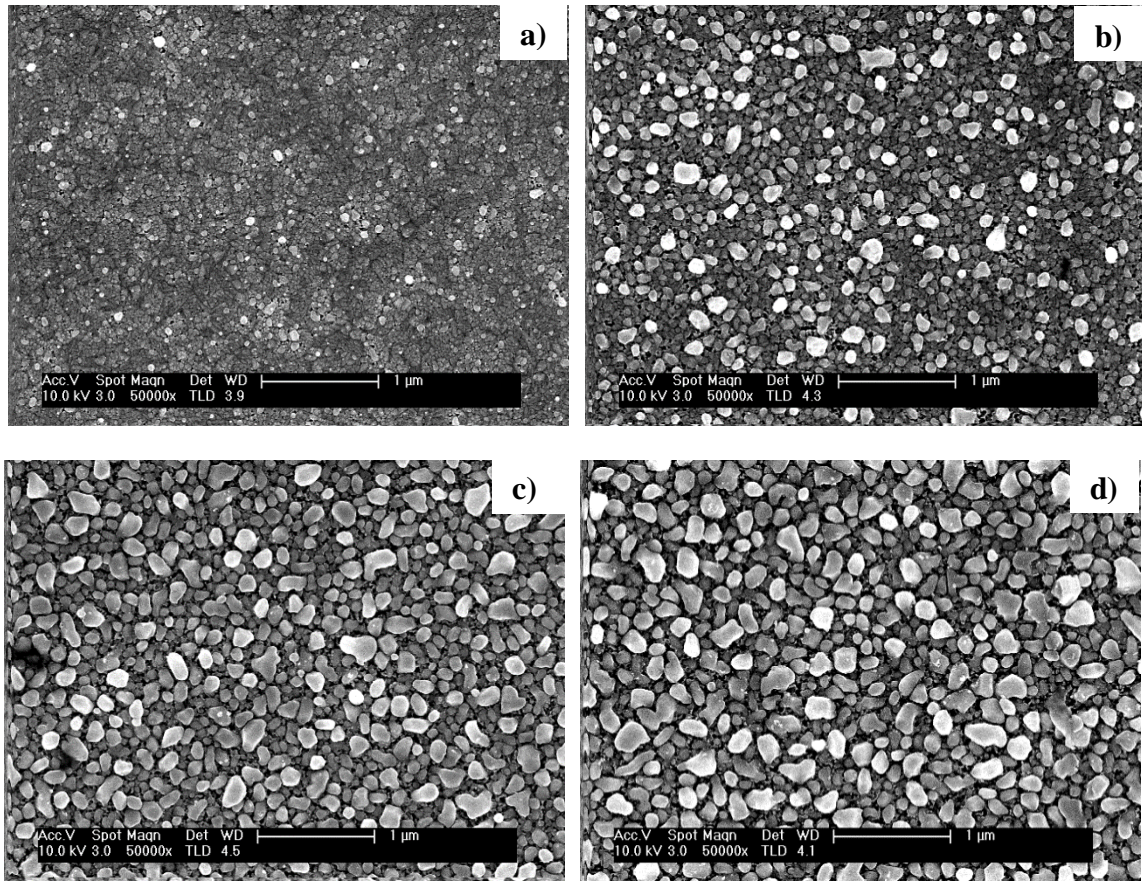
Figure III. 17: *SEM images of ZnS nanostructures at: a) −1.0, b) −1.1, c) −1.2 and d) −1.3 V vs. SCE.*

As the deposition potential increased from -1 to -1.3 V, the crystallite size increased from 37.60 nm to > 100 nm. By comparing these values of average crystallite size obtained from Scherrer's formula and those obtained from AFM measurements (Table III. 4), it was found that the inclusion of strain has a significant effect on the average crystallite size of ZnS nanostructure. This variation was caused by the difference in averaging the particle size distribution [104].

Table III. 4: *Grains size obtained from AFM images.*

E(V vs. SCE)	AFM analysis (nm)
-1	37.60
-1.1	37.80
-1.2	53.173
-1.3	104.053
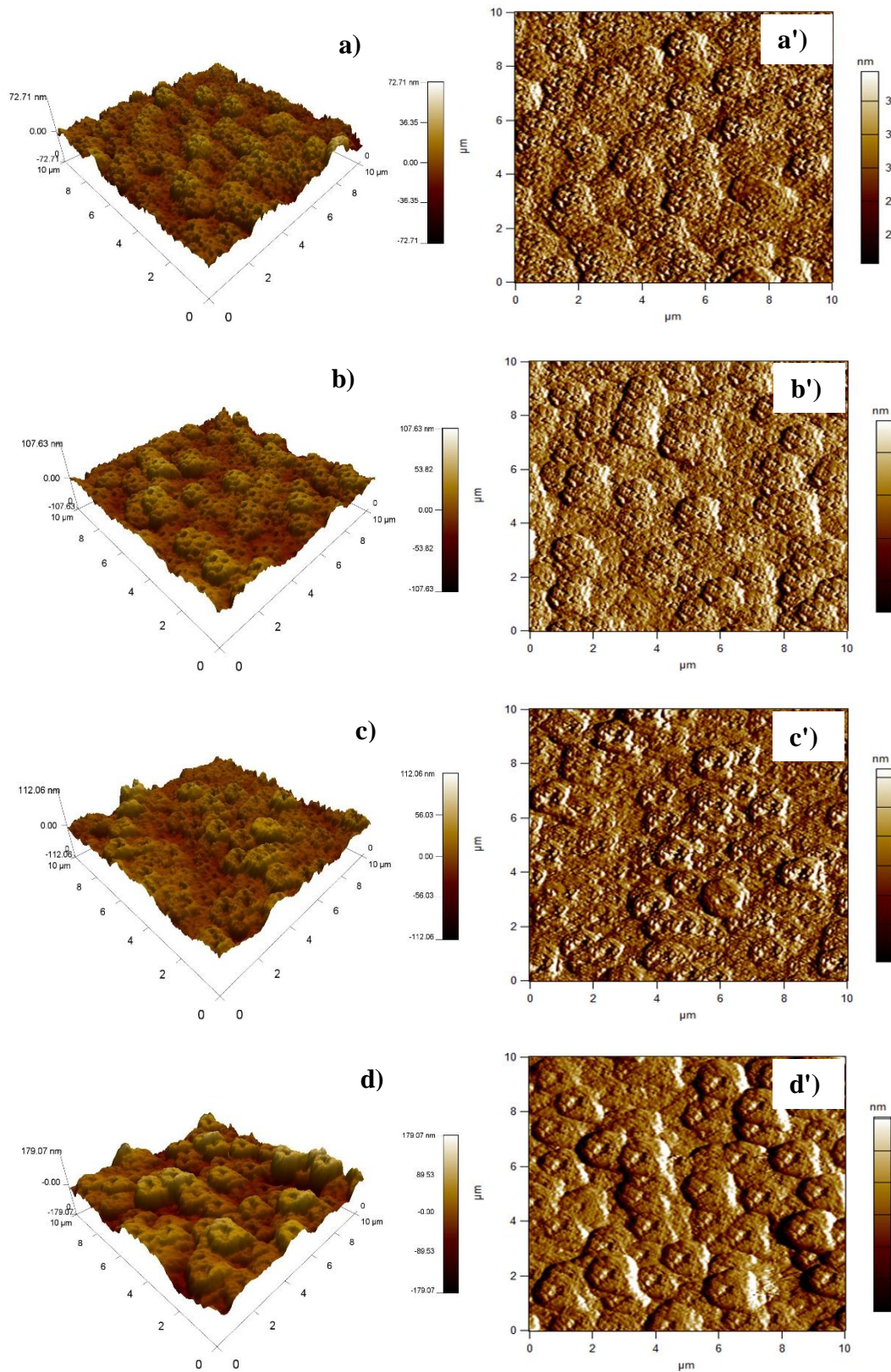
Figure III. 18: *2D and 3D atomic force microscopic images of ZnS nanostructures electrodeposited at different applied potential: a, a') −1.0 b, b') −1.1 c, c') −1.2 and d, d') −1.3 V/SCE.*

It was determined that samples with higher thickness and larger grains exhibit a very rough surface due to the increased differences in height (*Z* range) at their boundaries as compared to the smaller grains.

However, the morphology of the films prepared at potentials ranging from -1 to -1.3 V is shown in figure III. 17, the particles are seen to be agglomerated leading to increasing the applied potential and were found to be homogeneously distributed. These results show clearly that the morphology of ZnS nanostructures depends on the applied potential.

3.4 Crystal Structure

Figure III. 19 shows the XRD patterns of ZnS nanostructures formed by electrochemical deposition at different applied potential ranging from -1 to -1.3 V vs SCE in the diffraction angle ranging from 25° to 55°, the peaks marked with a star (*) are assigned to the ITO substrates. In all cases, one dominant peak observed at $2\theta \approx 33.01°$ correspond to (200) orientation of the zinc blende structure of ZnS (JCPDS 05-0566). As the applied potential increased, the intensity of this peak increased drastically indicating better crystalline phase for the films deposited at -1.3 V.
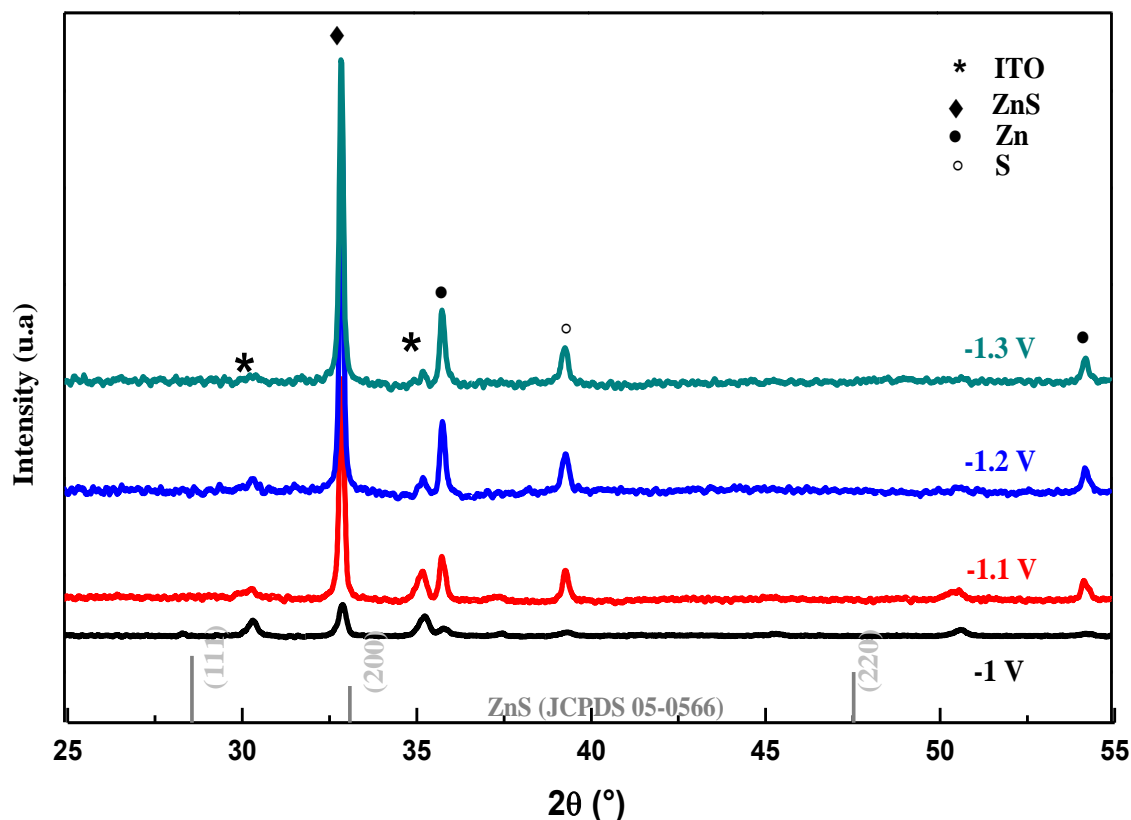
Figure III. 19: *XRD patterns of the ZnS nanostructures electrodeposited at different applied potentials.*

Moreover, it is interesting to note that for all ZnS nanostructures, the XRD patterns showed the presence of some impurity such as sulphur at $2\theta = 39.41°$ related to (310) plane [14] and metallic zinc at $2\theta = 35.89°$ and $2\theta = 54.31$ related to (002) and (102) planes, respectively [37].

Table III. 5: Calculated values of the microstructural parameters of ZnS nanostructures electrodeposited at different applied potentials.

potential (V vs. SCE)	2θ (•)	d_{hkl} (Å)	Lattice constant (Å)	Average crystallite size (nm)	Microstrain $(\varepsilon) \times 10^{-2}$	dislocation density (δ) $(\times 10^{10}$ lines/cm$^2)$
-1.0	32.94	2.71	5.42	65.87	22.80	2.30
-1.1	33.05	2.70	5.41	96.40	15.30	1.07
-1.2	32.94	2.71	5.43	>100	12.20	0.75
-1.3	32.93	2.71	5.43	>100	12.00	0.74

These patterns showed that the structure of the deposited films was sensitive to deposition potential used for the elaboration of ZnS nanostructures. In order to determine the variation of the average crystallite size (D), the size of the crystallite oriented along the (200), different microstructural lattice parameter was summarized in table III.5.

In general, the larger crystallite size, the smaller lattice strains at a given applied potential [105]. The increase in crystallite size is due to the increase in the thin film thickness by increasing the potential. The rate of the deposition reaction increases with increasing the deposition potential and the crystallites grow faster resulting in a larger grain size.

For further study, we have calculated the thickness of the obtained nanostructures using profilometer AltiSurf 500, as well as, the growth rate was calculated using the following equation:

$$G_R = \frac{d}{t}$$ (Eq. III.1)

While G_R(nm/s) is the growth rate, d thickness(nm) and t deposition time(s).

It is clear from table III. 5, that the small size of crystallite 65.87 nm to 96.40 nm were observed in the ZnS nanostructures of thicknesses 202.60 nm to 229.92 nm, respectively. This small grain size was observed due to the slow growth rate of the crystallite. However, large grain >100 nm has been observed for the films with the thickness 365.50 nm to 401.54 nm. This could be attributed to the differences in the growth rate under the applied potential. This latter was estimated from the

thickness measurement of ZnS nanostructures grown in the same deposition time. The growth rate was found to be increased significantly from 0.67, to 1.33 nm/s (Table III.6). Therefore, the nucleation frequencies of ZnS nanostructures tend to be higher when the deposition rate increases and the grain size is increasing consequently. The increase in grain size with thickness, reported in the present work, is in good agreement with those reported by other workers [104], [106].

Table III. 6: Displays effect of the applied potentials on growth rate, thickness and roughness of ZnS nanostructures.

Potential (V vs. SCE)	*Growth rate (nm/s)*	*Thickness (nm)*	*Roughness (nm)*
-1	0.67	202.60	08.67
-1.1	0.76	229.92	13.23
-1.2	1.218	365.50	12.82
-1.3	1.338	401.54	33.11

The strain in thin film is defined as the disarrangement of lattice created during their deposition and depends upon the deposition parameters. In this work, the strain decreases from 6.11×10^{-2} to 3.21×10^{-2} with an increase of ZnS crystallite size (Fig. III.20) and thin film thickness. The low strain indicates the best lattice arrangement in the film deposited at -1.3 V. It is reported in the literature that the decrease in strain shows a decrease in lattice imperfections that favors the formation of an excellent crystalline quality.
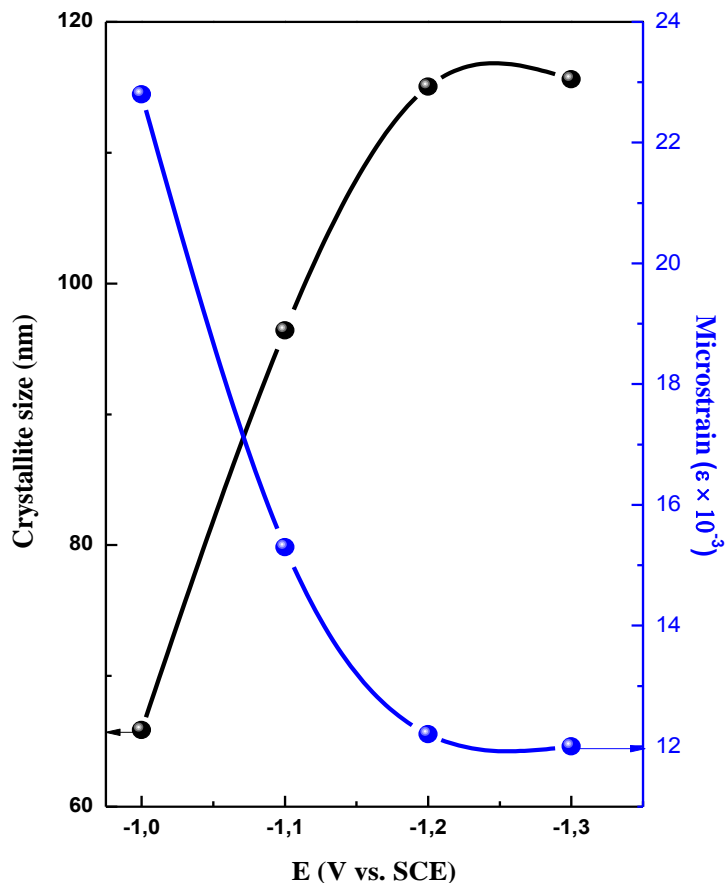
Figure III. 20: *Crystallite size (left axis) and microstrain (right axis) of electrodeposited ZnS nanostructures as a function of applied potential.*

The lattice constant for ZnS thin film deposited at different applied potential is found nearly equal to 5.41 to 5.43 Ǻ. The observed lattice constant in the present study is in good agreement with the standard value of 5.40 Ǻ (JCPDS05-0566). The slightest deviation in the values of the lattice parameter of the ZnS nanostructures from the bulk value indicates the presence of small strain in the deposits. The strain in the ZnS nanostructures may arise due to the change of lattice nature, the concentration of native imperfections and the pressure of ions of different sizes during the electrodeposition process [88].

The dislocation is imperfection in the crystal, which is created during the growth process of the ZnS thin film. The determination of the dislocation density of nanostructures is crucial for studying the crystallographic properties of nanostructures. The dislocation density decreases from 2.30 10^{-10} to 0.748 10^{-10} line cm^{-2} with an increase of film thickness at higher cathodic deposition potential. The minimum dislocation density (2,30 10^{-10} line cm^{-2}) is observed in the films with higher thickness deposited at -1.3 V. These obtained dislocation density values are lower by one order of magnitude than those reported by other investigators [107]. The decrement in the dislocation density

with applied potentials indicates diminution in the lattice imperfections and may be attributed to the lattice misfit in the film and improvement in the crystallinity [108].

3.5 Optical properties

The optical transmittance was measured in the wavelength range of 300-800 nm. Figure III. 21 shows the transmittance spectra of prepared ZnS films at different applied potential on ITO glass substrate. The absence of interference fringes in films transmittance spectra indicates that they have a rough surface morphology. At first sight, we observed that all samples of ZnS nanostructures have a lower transparency in the visible range, it's due to the presence of Zinc element which give a gray color to the resulted film. Also, when the samples have a lower transmittance they use annealing to increase their transparency. The optical transmittance was decreased with the increase of potential from -1 to -1.3 V.
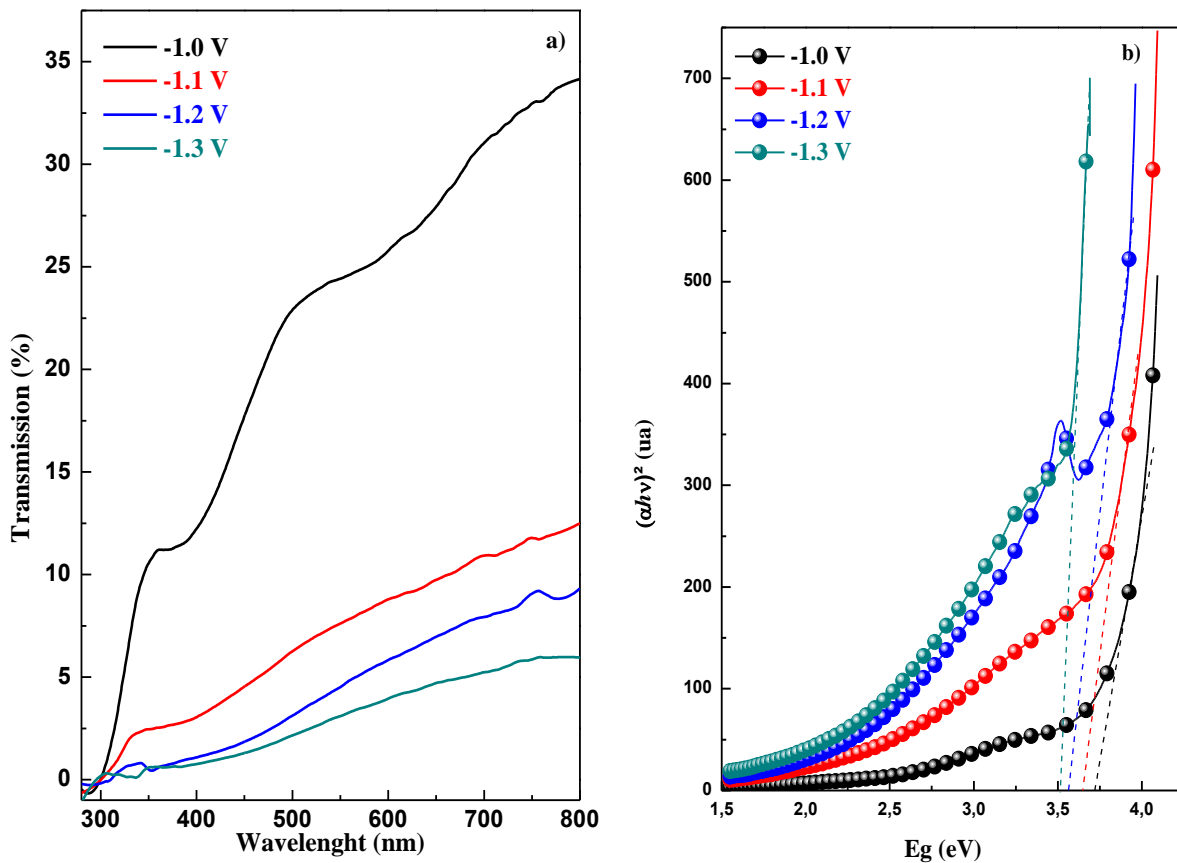
Figure III. 21: *a) Transmittance spectrum and b)* $(\alpha h \nu)^2$ *vs. energy dependence for the determination of the optical band gap energy.*

From the optical absorption spectra measured in the wavelength range of 300- 800 nm, the band gap of the films was determined as the variation of $(\alpha h \nu)^2$ versus $(h \nu)$ (Fig. III.21), the linear nature of the graph indicates the existence of direct transition. The values of Eg are evaluated from the intercept of the straight-line portion at the horizontal axis ($\alpha = 0$) from the relation (Eq.II.6) used

the Urbach Tail (E_u) as a signature of the disorder, which is related to the disorder in the film network calculated from the expression (Eq. II.7) Eu can be estimated from the inverse slope of the linear plot of *ln (α)* versus *hυ*.

The *Eg* values of ZnS at different applied potentials and the calculated values of Urbach energy are presented in Figure III. 22. As it can be seen, the variations of both *Eg* and *Eu* correlate very well, the *Eg* values were found to decrease from 3.74 to 3.50 eV while the disorder varies inversely. This indicates that the optical gap variation is mostly controlled by the disorder in the film and confirmed the more realignment in orientations and improvement in crystallinity which was confirmed before by XRD analysis.
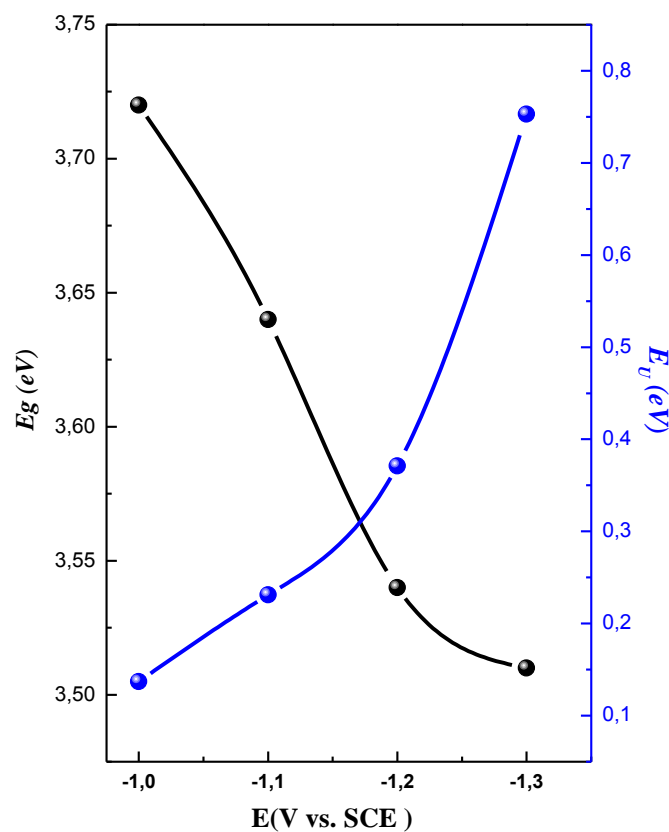
Figure III. 22: *Variation of the band gap energy and the disorder of ZnS thin film electrodeposited at different applied potentials.*

It's well known that the variation of the optical gap and the variation of the crystallite sizes reveals that the gap has an opposite behavior regarding the crystallite variation and as already mentioned above, due to the large crystallite size obtained at more negative applied potential, the optical gap is compressed. The compression of the gap is due to the increase of the disorder in the film. The disorder is characterized by the band tail width (valence and conduction). The optical gap

is the energy difference between the two band tail bands. Therefore, a disorder increasing is accompanied by a compression of the optical gap[109].

III.4 Influence of the deposition time

4.1 Mott-Schottky measurments

As reported before M-S measurements were employed to determine the carrier concentration, band plat potential and the thickness of the space charge area (W) at the ZnS/electrolyte interface. figure III. 23 shows the Mott-Schottky curves of the ZnS nanostructures obtained at different deposition time achieved in a supporting electrolyte of 0.5 M Na_2SO_4, while the frequency and amplitude are set at 800 Hz and 10 mV/s. As it was reported in the previous M-S results, the linear part of the curves of capacitance as a function of the applied potential in the depletion zone is positive, this indicates that all the samples are n-type semiconductors. While the n-type conductivity origin is attributed to Zn_S defect presented in the films, this last was reported in S-rich condition [93],[45].
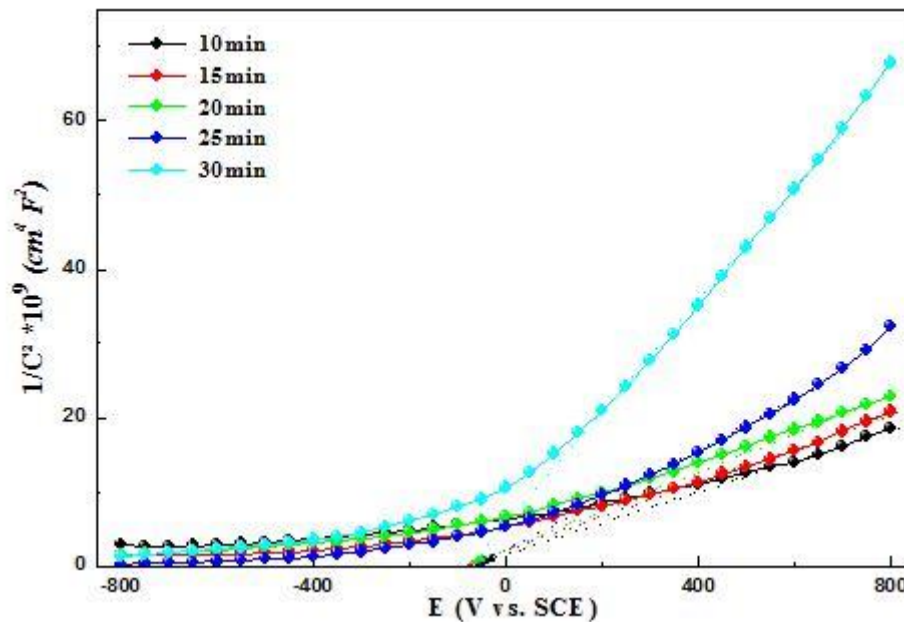
Figure III. 23 : Mott-Schottky plots of the ZnS films deposited at different deposition times a)10, b) 15, c) 20, d) 25 and e)30 min.

Indeed, the determination of the value of the flat bands potential E_{fb} is done by extrapolation of the partial linear curves of Mott-Schottky to $\frac{1}{C^2} = 0$ ($E_{fb} = E - \frac{KT}{q}$). When the carrier concentration was estimated from the slope of this line. The deposition time have no effect on the flat band potential, but influence the carrier concentration density as illustrated. The obtained values of E_{fb} and N_D, calculated at different deposition times are summarized at the table below.

Table III. 7: Experimental values of E_{fb} and N_D obtained at different applied potential.

Times (min)	N_D (10^{20}cm^{-3})	E_{fb} (V/ECS)
10	6.80	
15	7.41	
20	8.39	-0.0678
25	5.26	
30	2.43	

4.2 Morphology analysis

AFM is a convenient technique to study the morphological characteristics and surface roughness of semiconductor nanostructures and to observe nanostructures of zinc sulfide nanostructures. It is well known that AFM is one of the most effective ways for the surface analysis due to its high resolution and powerful analysis software. The topography (3D images) and surface roughness along with grain sizes (2D images) of the ZnS nanostructures deposited at different deposition time are represent in Figure III. 24.

Table III. 8: Effect of the deposition time on the roughness of ZnS nanostructures.

times (min)	RMS (nm)
10	23.39
15	26.97
20	26.99
25	38.54
30	24.81

With the electrodeposition time of 10 and 30 min, the films showed a granular structure with the same shape and different size of the grain, which is different from the films electrodeposited at 15, 20 and 25 min we see that the grains doesn't deposited regularly. The ZnS films show a better coverage of the ITO substrate in the case of the films deposited at 15 and 30 min.
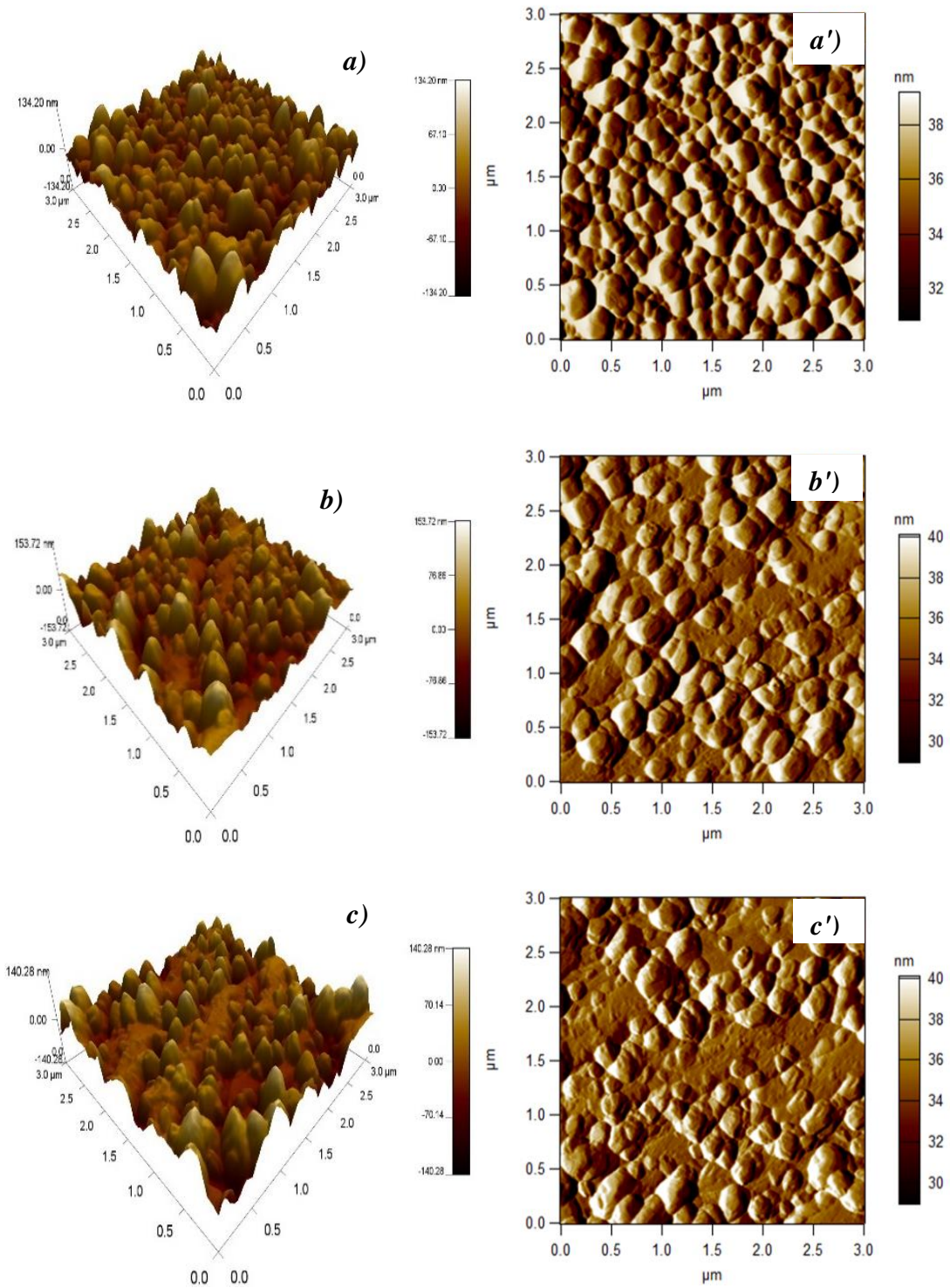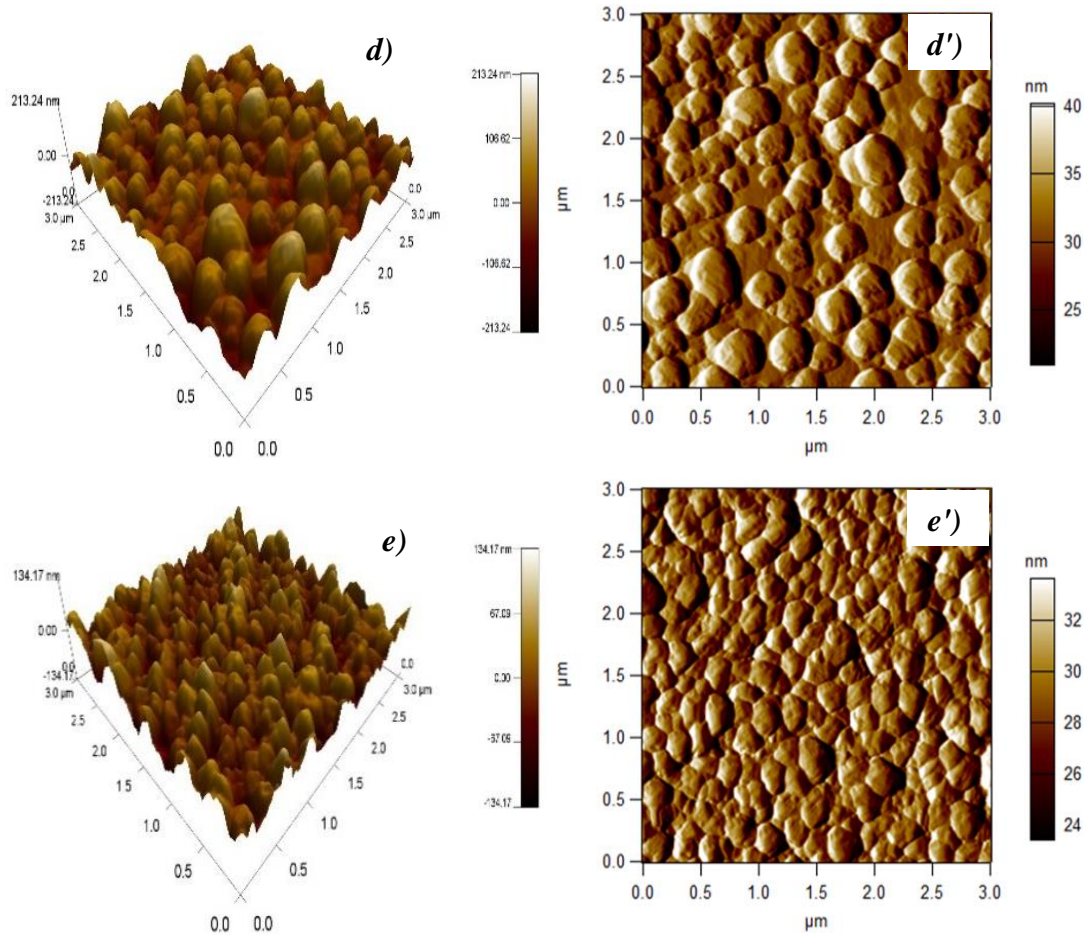
Figure III. 24: *2D and 3D atomic force microscopic images of ZnS nanostructures electrodeposited at different deposition time: a, a') 10, b, b') 15, c, c') 20, d, d') 25, e, e') 30 min.*

The three-dimensional atomic force microscopy images (3D) were used to understand the orientation of the grains and to estimate the root mean square (RMS) surface roughness. At the left side of AFM images, an intensity strip is shown, which indicates the depth and the height along the z-axis. It can be highlighted that AFM observations depict rough films (RMS ranges from 26.97 to 38.54 nm), with a non-uniform growth over the range of 15–25 min (Fig. III.24) show a disturbed surface with randomly oriented crystallites showing. Then, a relatively uniform distribution of spherical agglomerates and a relatively good connectivity over the substrate surface is clear from the electrodeposited film at 10 and 30 min (Fig. III. 24). This suggests that the growth mechanism of electrodeposited ZnS is of two types: ion-by-ion and cluster-by-cluster. This influences the change of the orientation observed by XRD analysis. Similar results were found by several researchers [110]–[113]

4.3 Crystal Structure

Figure III. 25, shows the XRD patterns of ZnS nanostructures formed by electrochemical deposition at different time ranging from 10 to 30 min, in the diffraction angle ranging from 20° to 70°.

Table III. 9: Calculated values of the microstructural parameters of ZnS nanostructures electrodeposited at different deposition times.

Samples		FWHM (°)	2Θ (°)	d (Å)	a (Å)	D (nm)
10 min	(111)	0.32	28.57	3.12	5.407	50.03
	(200)	0.25	33.11	2.70	5.406	64.74
15 min	(111)	0.29	28.56	3.12	5.408	56.22
	(200)	0.25	33.14	2.70	5.401	65.26
20 min	(111)	0.26	28.71	3.10	5.381	61.55
	(200)	0.21	33.18	2.69	5.395	66.05
25 min	(111)	0.29	28.60	3.11	5.401	51.83
	(200)	0.24	33.05	2.70	5.416	60.97
30 min	(200)	0.21	33.01	2.71	5.422	75.43

Different diffraction pic was observed at 2θ~ 28.87°, 33.2°, and 51.30° corresponds to the orientation (111), (200) and (311) [110], [113], respectively. Which indicate, the formation of Zinc blende structure, the pic marked with a star are the peaks of the substrate, only one other pic at 2θ: 36.46 attributed to Zn impurities [37]. The main characteristics of the patterns remain the same for all the samples, an increase in the intensities of the diffraction peaks with the thickness for the samples deposited at 10, 15, 20 and 25 min. Which is proportional to the number of crystallites in the formed films, the orientation (111) disappeared for the samples deposited at 30 min. The preferential orientation of the ZnS nanostructures prepared is according to the plane (200), from to the results of X-ray, it is concluded that the growth is mainly following the plane (200) having the lowest surface energy.
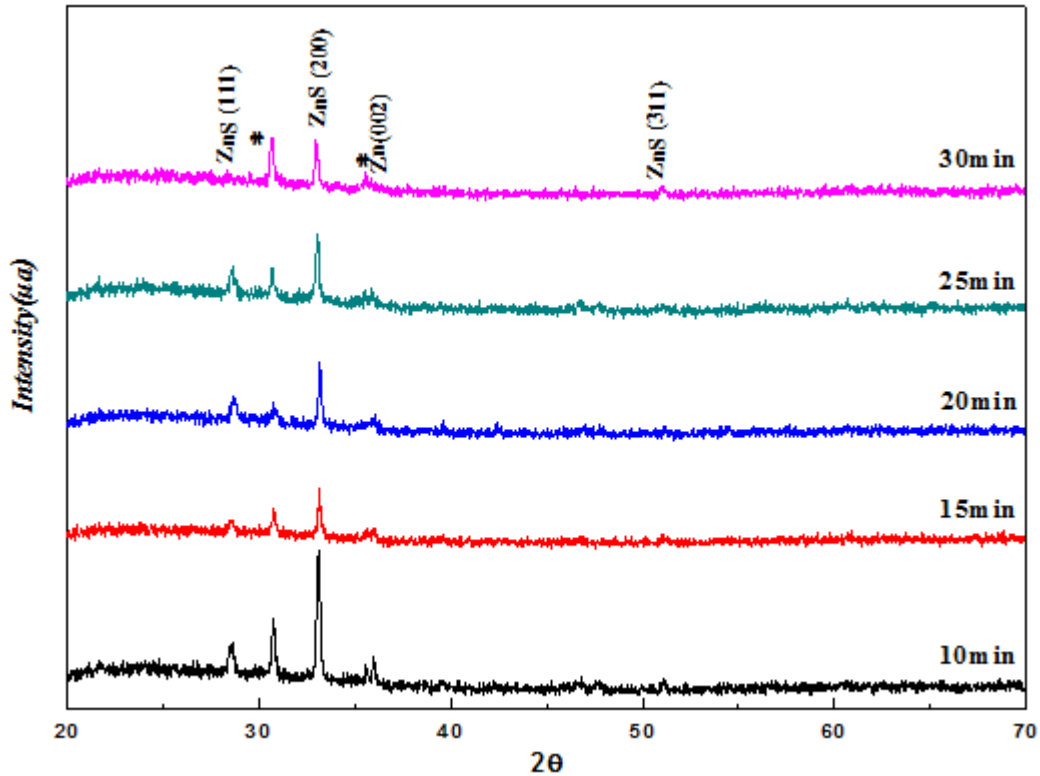
Figure III. 25: *X-ray diffraction patterns of ZnO films deposited at different time.*

4.4 Optical properties

4.4.1 Ultra Violet Visible spectroscopy

In Figure III. 26. a) we report the variation of the optical transmittance in the UV-VIS-NIR of the deposited nanostructures deposited at different time. It is clear that the deposited nanostructures exhibit a relatively high transmission ranged from 40 to 70 % for wavelengths greater than 350 nm. In the UV region, all the films exhibit a sharp fundamental absorption edge.

By exploiting the transmittance curves of the deposited films, the energy of the optical gap was estimated using the Tauc formula [92], taking into account the direct optical transition process of ZnS. Figure III. 26. b) shows the variation in bandgap energy as a function of deposition time. The measured optical gap values range from 3.54-3.73 eV, which is in the range of the massive ZnS [11], [22], [66].
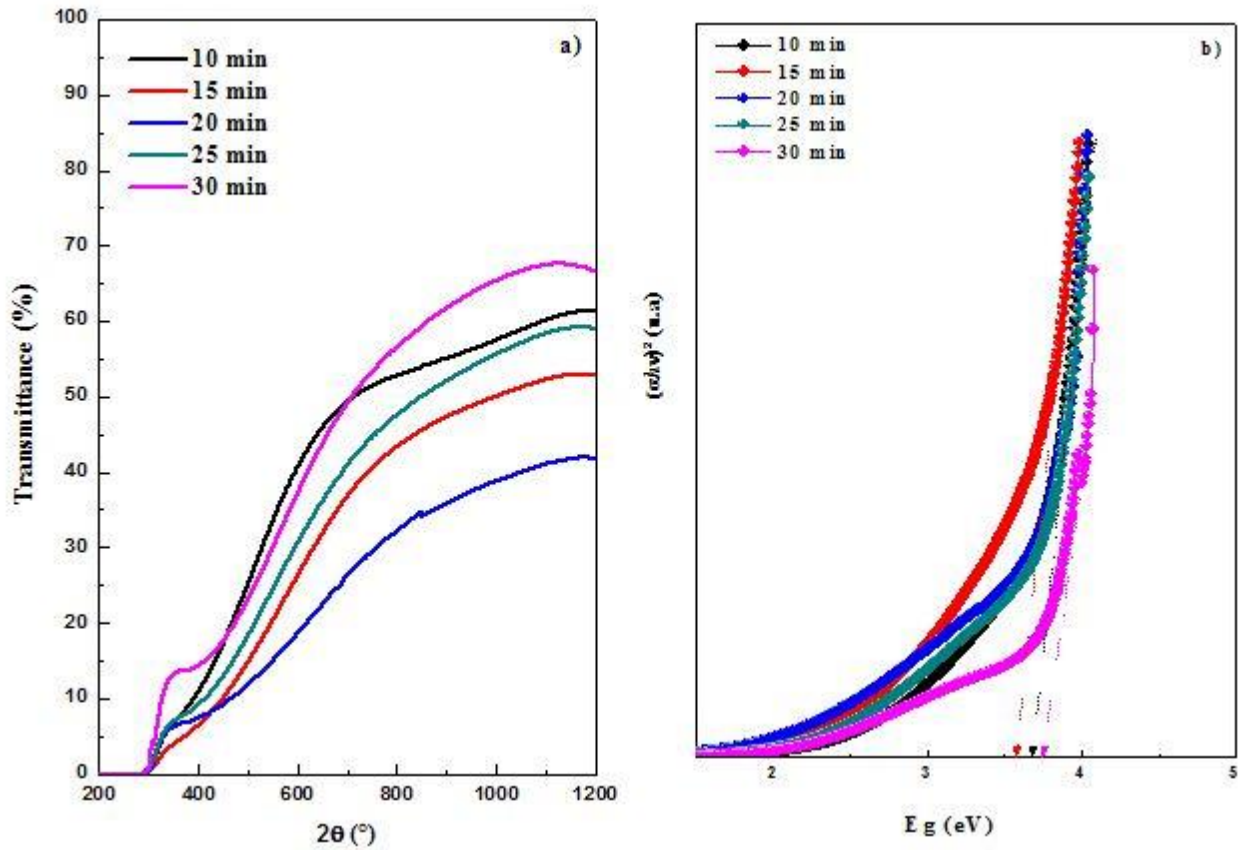
***Figure III. 26:** a) Optical transmission spectra b) Tauc plots of ZnS nanostructures electrodeposited at different deposition time.*

4.4.2 *Time Resolved Photoluminescence*

Time-resolved photoluminescence (TRPL) decay curves of the ZnS/ITO/glass samples collected for ZnS nanostructures using 325 nm pulsed diode laser with a 60 ps, are shown in Figure III. 27. a-d). The Best fits to the decay curves are achieved with double exponential decays, described by the equation as follows [114]–[116]:

$$F(t) = B_1 e^{(\frac{-t}{\tau_1})} + B_2 e^{(\frac{-t}{\tau_2})} \qquad \qquad \text{IV.1}$$

Where τ_1 and τ_2 represent the slow and fast lifetime, respectively, and B_1, B_2 is the amplitude of the components. The shorter lifetime is on a time scale of several nanoseconds, and the longer lifetime is on a time scale of tens of nanoseconds. The shorter lifetime is generally attributed to the intrinsic recombination of initially populated internal core states. However, the possible origin of the longer lifetime remains relatively uncertain [117]. The obtained results are summarized in table III. 10.

Table III. 10: *Best Fit Values of* τ_1*, and* τ_2 *and of the Relative Weights A$_1$ and A$_2$ for the films deposited at different time.*

Samples	$\tau_1(s)$	B_1 (%)	$\tau_2(s)$	B_2 (%)
10 min	$4.39*10^{-11}$	92.48	$1.51*10^{-9}$	7.52
15 min	$1.44*10^{-10}$	90.42	$2.58*10^{-9}$	9.58
25 min	$4.82*10^{-11}$	92.79	$1.71*10^{-9}$	7.21
30 min	$4.5*10^{-10}$	98.61	$2.64*10^{-9}$	1.39

A random variation of the slow and fast lifetime with the increase of the deposition time are observed. The fast and slow decay of orange luminescence are attributed to two different relaxation processes. The fast decay is assigned to the direct recombination of electrons and holes at luminescent sites. The slow decay is due to the trapped electrons, which is captured by shallow defect states first and then relax to the luminescent sites. The total quantity of defect states change dramatically as the deposition time increases. The decrease in defect states makes the relaxation processes through shallow defect states accelerate. The excited electrons and holes are generated in conduction and valence bands of ZnS, respectively, when the excitation light is 325 nm [118]. The recombination processes through shallow defect states are mutable for the different analyzed samples, since the amount of shallow defect states is changed. Thus, the relative content of the slow lifetime relaxation process change. On the other hand, the trapped electrons are generated directly near the luminescent sites when 325 nm light is used as excitation source [118]. More defect states make more trapped electrons relax nonradiatively. Consequently, less defect states in ZnS obtained for the sample deposited at 15min mean that more trapped electrons can contribute to the emission. As a result, the relative content of slow lifetime process change with the increase of the deposition time. Orange luminescence are generally caused by donor–acceptor recombination [119].
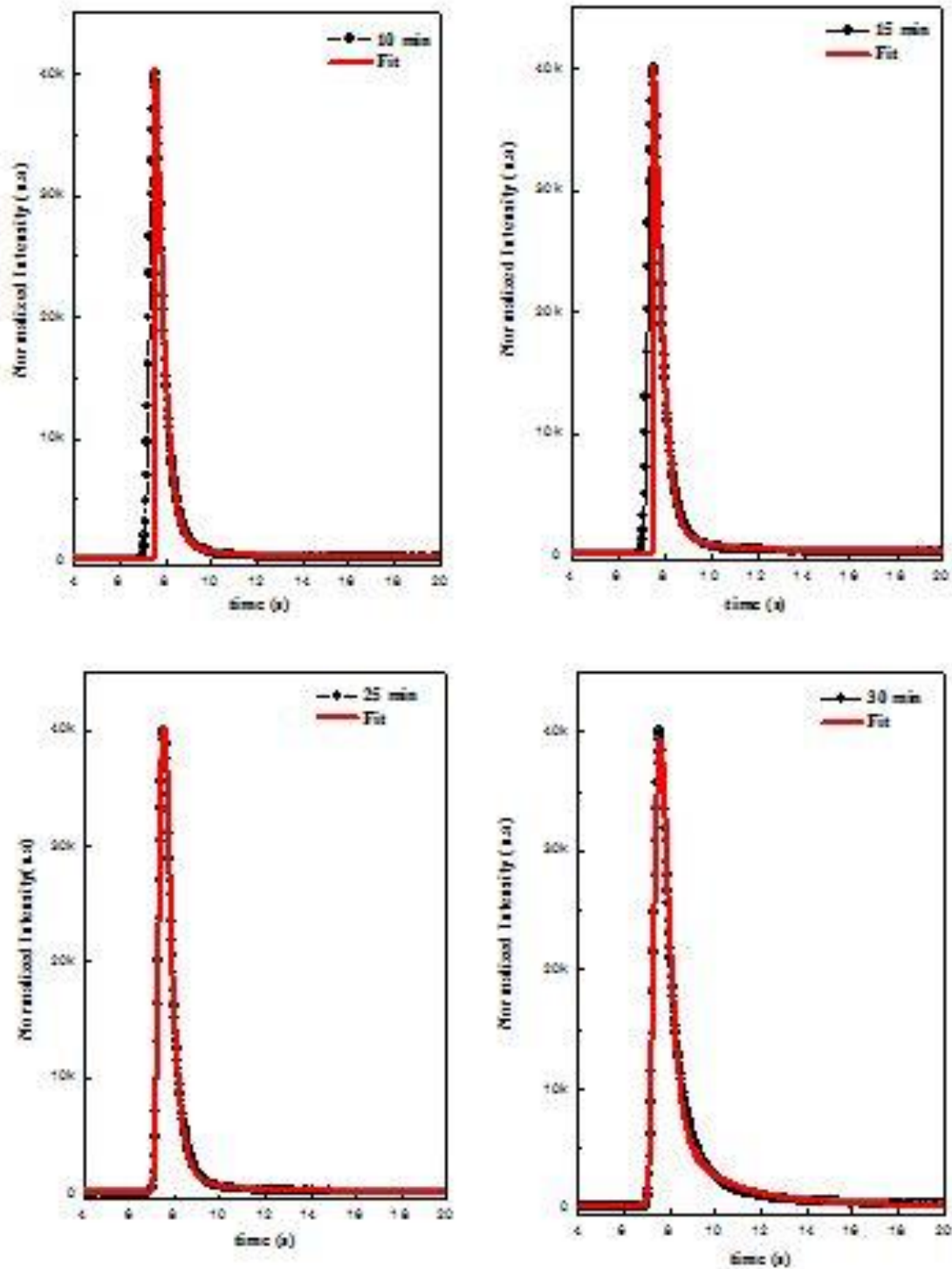
Figure III. 27: *A set of spectrally integrated Time resolved photoluminesence curves of the ZnS nanostructures measured at room temperature for samples electrodeposited at different times. The symbols are measurement data, and the solid lines are corresponding bi-exponential fit.*

III.5 Influence of annealing under sulfurization

To remove the metallic zinc impurities presented in the obtained nanostructures, some annealing experiment was carried out. Firstly, the oven was prepared by; putting the samples and the sulfur powder in two different holders in the tube of the oven, as shown in figure III. 28; after that the Tube of the oven was cleaned using Ar gas for 5 min to eliminate all the impurities, even all impurities dispersed we reduce the gas flow. This inert gas was used to prevent the formation of oxide in the annealed films (ZnO), two different experiment were carried out in order to study the effect of annealing under sulfurization;

- Annealing at 500 °C for 1 hour at 250 mg of sulfur.
- Annealing at 300 °C for 1 hour at 60 mg of sulfur.

Figure III. 28 : *Tube furnace for annealing under a sulfurized atmosphere*

The first annealing test was carried out for the samples deposited at 15, 20 and 25 min at 500°C for 1h hour under sulfurization atmosphere. The obtained annealed films were characterized using XRD and UV-Vis analysis. As first view the obtained nanostructures after annealing has a yellow color, which may be related to the presence of high amount of sulfur in the samples.

5.1 Annealing at 500 °C

As a first test we had fixed the annealing temperature at 500 °C, and the S amount at 30 mg, after passing 1h of annealing, a yellow color of the obtained nanostructures was obtained, in order to study the influence of annealing under sulfurization at 500 °C a structural and optical characterization are represented;

X-ray diffraction patterns show that the samples annealed at 500 °C exhibit the presence of ZnS and S structure, the samples before annealing shown the presence of Zn and ZnS peaks. For the samples deposited at 15 min. The presence of sulfur peaks confirms that the yellow color was attributed to the excess of sulfur in the films. This result must be explained by the high quantity of sulfur placed on the holder compared to the concentration of sulfur used for deposition, thus the melting point of sulfur is very small compared to the temperature used for annealing. At the first time of annealing before reaching 500 °C, the sulfur deposits directly on the film surface. The decrease in the intensity of ZnS peaks was followed by the appearance of high sulfur peaks as shown in Figure III. 29. Three diffraction peak (206), (213) and (006) confirms the presence of high amount of sulfur in the obtained nanostructures. While, the (111) and (200) peak intensity decreases compared to the samples before annealing. The desperation of Zn with the decrease of ZnS plan intensity, might be explained as follows, the low melting temperature of sulfur [120] allow us to explain that at the first annealing time when the temperature begins to increase the sulfur start to deposits to the surface of the films. While the flow of inert gas circulates on the furnace tube no other phases (such as oxides) was formed. When the temperature reached 500 °C which is the melting temperature of Zn [121], all the impurities of Zn have disappeared and the weak Zn-S bond is evaporated [67]. High annealing temperature favors the disappearance of Zn [121], the same results were observed for the two other samples as shown in figure III. 29.
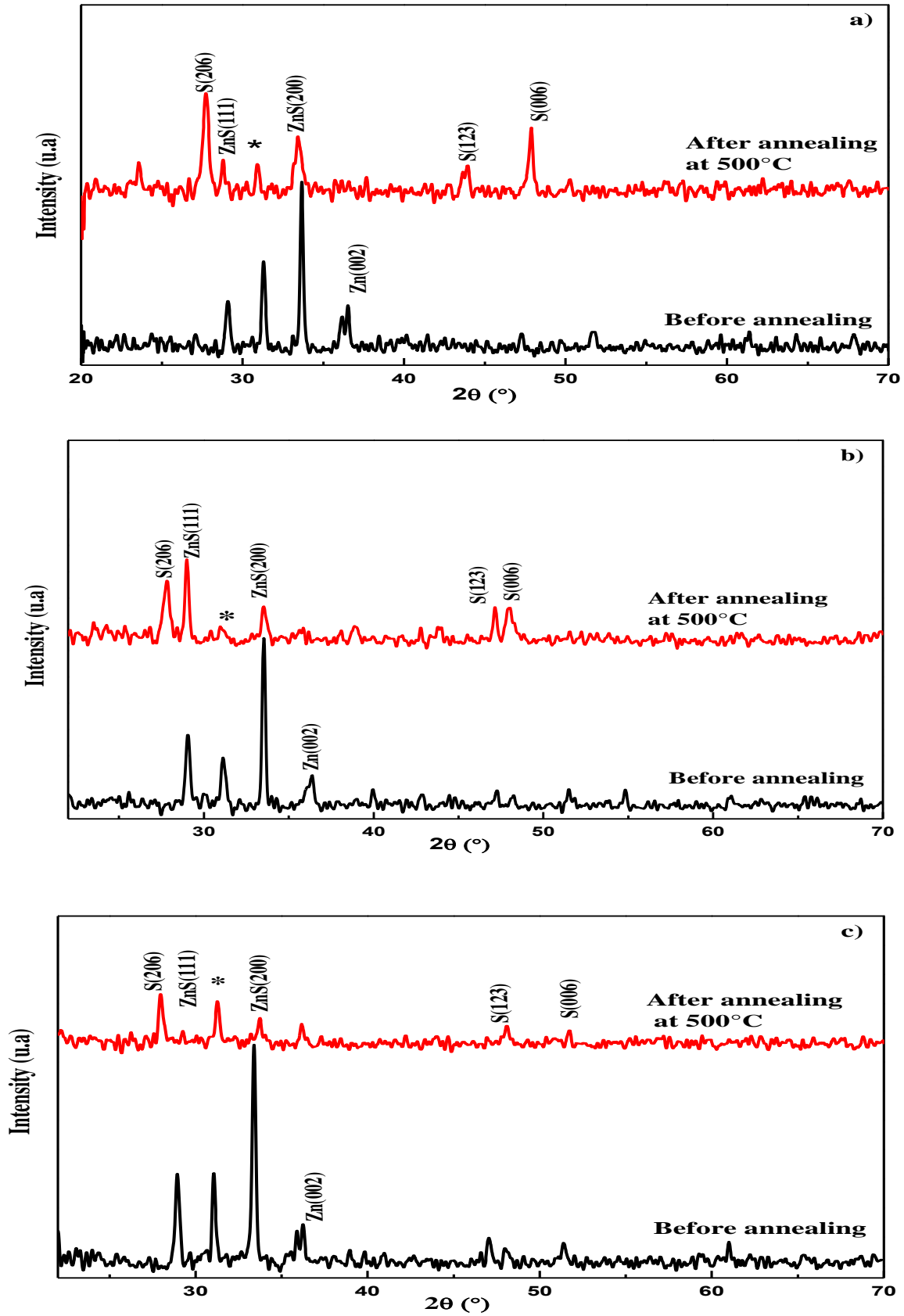
Figure III. 29: *XRD-patterns of the samples deposited at different time deposition a) 15, b) 20 and c) 25min before and after annealing.*

The optical measurements of the ZnS before and after annealing were carried out at room temperature by UV-visible spectrophotometer, in the spectral range extends from a 200 nm to 1500 nm. The transmission spectra of the samples before and after annealing are present in figure III. 30. The shape of the set of spectra is identical for all the samples before and after annealing. According to the transmittance curve, the samples after annealing absorbed in the UV range and had a low transmittance in the range 320 nm to 450 nm, an increase in transmittance in the N-IR (800 nm-1500 nm) Intel 80% was obtained. From the transmittance spectrum, figure III.30, a shift toward longer wavelengths was obtained after annealing for all the annealed nanostructures, this is probably related to the presence of a high sulfur there.
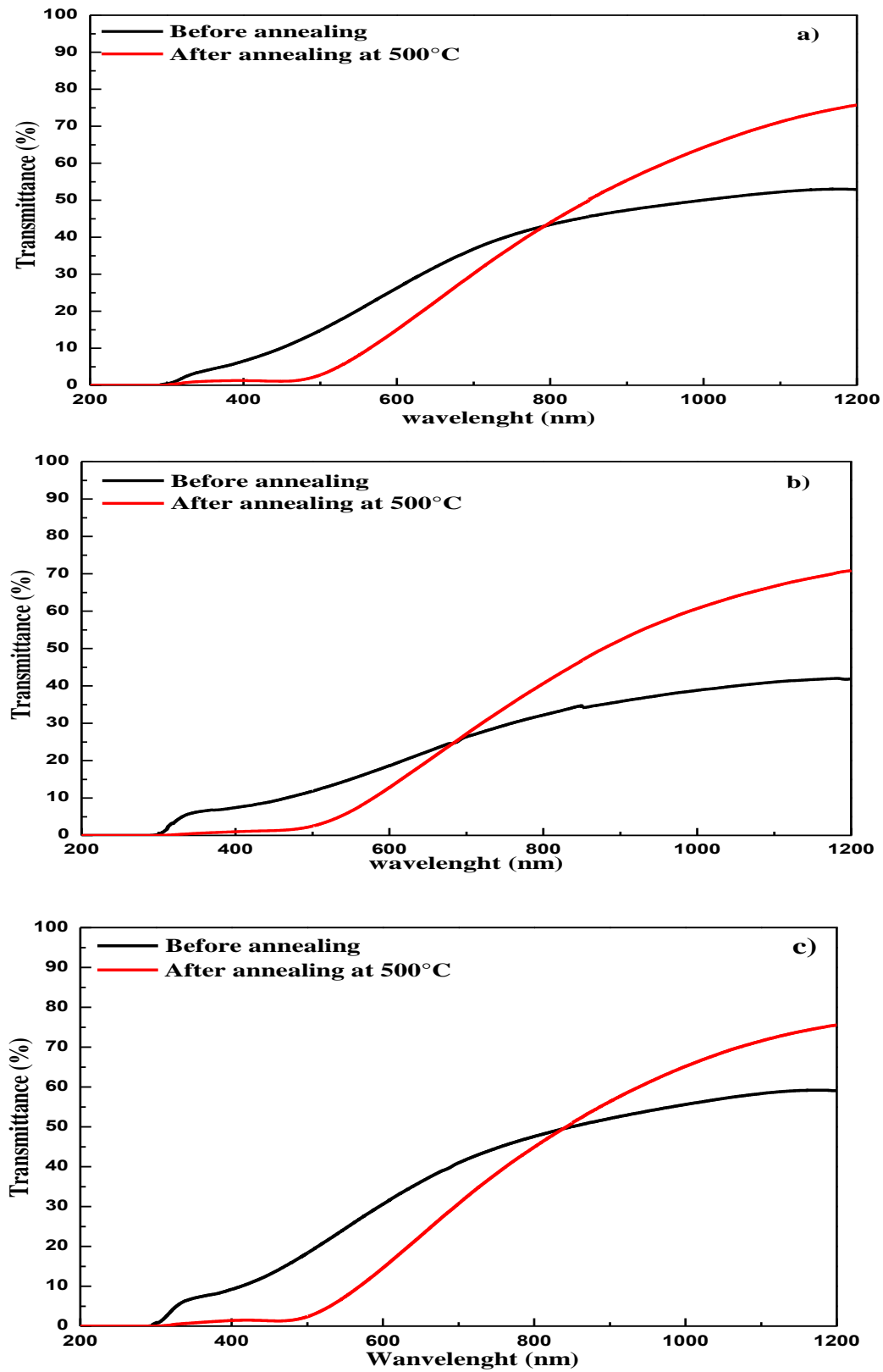
Figure III. 30: *Optical transmission spectra of ZnS nanostructures electrodeposited at a) 15, b) 20 and c) 25 min before and after annealing at 500°C for 1h.*

5.2 Annealing at 300 °C

After carrying out the first annealing test, an excess of sulfur was obtained, so we suggest to reduce the amount of sulfur and the annealing temperature to 60 mg and 300 °C respectively, this time we have used only one sample (20 min). The annealing was carried out for a duration of 1 h. While, the Ar gas was circulated in the tube to avoid any impurity.

The obtained film has a light yellow color, a series of characterization by XRD and UV-Vis was done and the results will be presented:

Figure III. 31 shows the XRD pattern of the sample deposited at 20 min before and after annealing at 300 °C for 1 h, almost we found the same result that we obtained in the first test before, the presence sulfur peak was obtained after annealing. We note that in this second test the peak of zinc has not disappear, while the ZnS decrease dramatically. The big challenge was, that the melting temperature of sulfur is small compared to the annealing temperature of the sample. We have made two test it doesn't work, then we suggest to use to tube-oven, where we put in the first one the sulfur in small temperature and in the second one we put the samples with high annealed temperature.
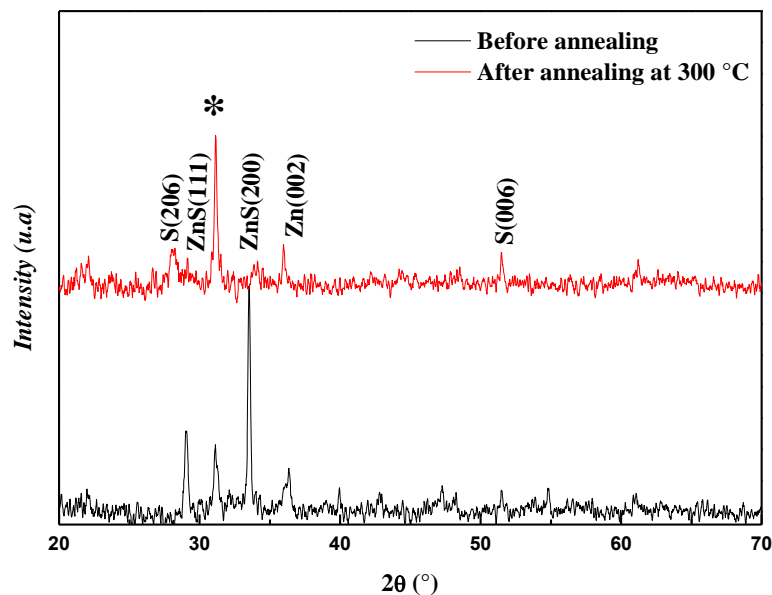
Figure III. 31 : *XRD-patterns of the samples deposited at 20 min before and after annealing.*

In the laboratory, we haven't more than one oven that's why we didn't do more much test. Thus, the quantity and the temperature of sulfur aren't the only parameters to be controlled during annealing experience, many other parameters should be controlled.

The optical transmittance of the deposited annealing is shown in Figure III. 32. The obtained ZnS film deposited after annealing exhibited the maximum transmittance of 70 %, compared to that

obtained before annealing, we conclude that annealing improves the transparency of the obtained films
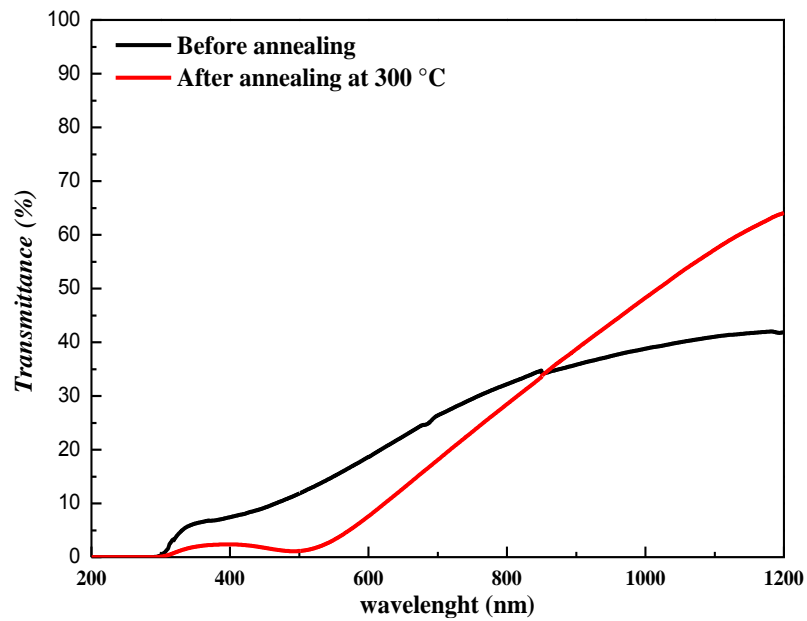
Figure III. 32: *Optical transmission spectra of ZnS nanostructures electrodeposited at 20 min before and after annealing at 300°C for 1h*
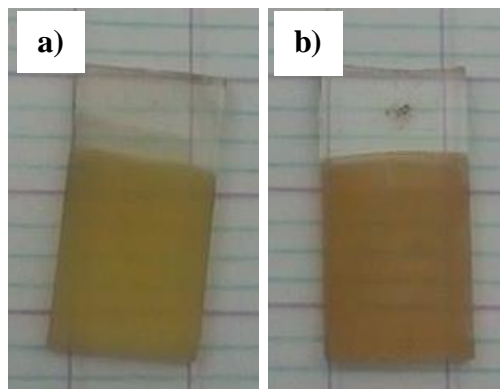
Figure III. 33: *photograph of the samples obtained after annealing at a) 500°C and b) 300°C.*

III.6 Summary

The main objective of this chapter is to study the influence of the different parameters (concentration, pH, potential, deposition time and annealing at sulfurization atmosphere) on the elaboration of ZnS nanostructures, the obtained results allow us to draw some conclusions:

➢ This study has shown that the deposition of ZnS nanostructures at the substrate interface has been well achieved by electrodeposition method under well-defined conditions.

➢ The zinc concentration has a great influence on the reduction of thiosulfate ions as well as the deposition potential was estimated from the cyclic voltammetry, the Mott-Schottky analysis confirms the n-type conductivity of the obtained ZnS nanostructures. A uniform distribution of grains was obtained by SEM for the high concentration of Zinc, while the XRD shows a (200) preferred orientation for zinc-blende phase, with the presence of some impurity.

➢ The variation of the bath pH doesn't influence the conductivity type, whereas the morphology of the obtained nanostructures is completely changed by decreasing the pH of the solution.

➢ The applied potential has a significant influence on the different properties of the obtained ZnS nanostructures.

➢ The crystallinity of the obtained nanostructures increase by increasing the deposition time, in addition the transparency of the obtained nanostructures was improved. The slow and fast lifetime collected from the time-resolved photoluminescence curves are in good agreement with the result obtained in the literature.

➢ At the end of this chapter, a short study on the influence of annealing under sulfurization doesn't successfully make.

Chapter IV

Doping ZnS nanostructure by electrochemical deposition

Chapter IV Doping ZnS nanostructures by electrochemical deposition

Chapter IV Doping ZnS nanostructures by electrochemical deposition

This chapter is devoted to study the effect of rare-earth dopants (Erbium and Samarium) on the properties of the electrodeposited ZnS nanostructures:

The characterizations of our doped nanostructures were conducted by different electrochemical methods, namely cyclic voltammetry, chronoamperometry and Mott-Schottky.

The atomic force microscopy was used to study the topography of the obtained (Er:ZnS and Sm:ZnS) nanostructures.

The XRD technique was used to study the influence of the rare-earth dopant on the structure and the average crystallites size.

The fundamental optical properties were studied using Ultra Violet-Visible spectroscopy and time resolved photoluminescence (TRPL).

IV.1 Erbium doped ZnS nanostructures (EZS)

1.1 Electrochemical reactions and doping

Sufficient Knowledge of the defect properties, which can be donors or acceptors, has an essential interest for doping semiconductor nanostructures. Doping semiconductor by different elements (Er, Sm, Al, Sn, In or Ga) has been the subject of several researches [122]–[129]. The electrodeposition of rare earth (Er and Sm) doped ZnS nanostructures will be reported for the first time in our work. For this, a systematic study was carried out, first we performed a series of voltammograms at different concentrations of erbium chloride. The following table shows the different concentrations of Er used in this study.

The addition of erbium chloride to the solution introduced several Er phases such as the Er^{3+} and $Er(OH)_3$ this last gives rise to the formation of a new erbium oxide phase (Er_2O_3). The E-pH diagram allow us to identify the different phase present in the solution, it has been presented in the figure VI. 1 [130]. In the range of pH from 5-10 the predominated species presented is $Er(OH)_2$. Therefore, the reaction occurring during the deposition process is:

$$Er(OH)_2 + OH^- \rightarrow Er(OH)_3 \qquad \text{(Eq IV.1)}$$

While in the acidic medium, the Er^{3+} ion is predominant more than 80 % of the species presented in the solution. The obtained results were calculated at room temperature.

In the present study, the ErCl$_3$ was added with different concentration to an acidic solution containing ZnSO$_4$ and Na$_2$S$_2$O$_3$, while the pH of the solution was adjusted 2.4 using H$_2$SO$_4$. As the first view, no other phases will be presented during the experiment the Er^{3+} acts like dopant.
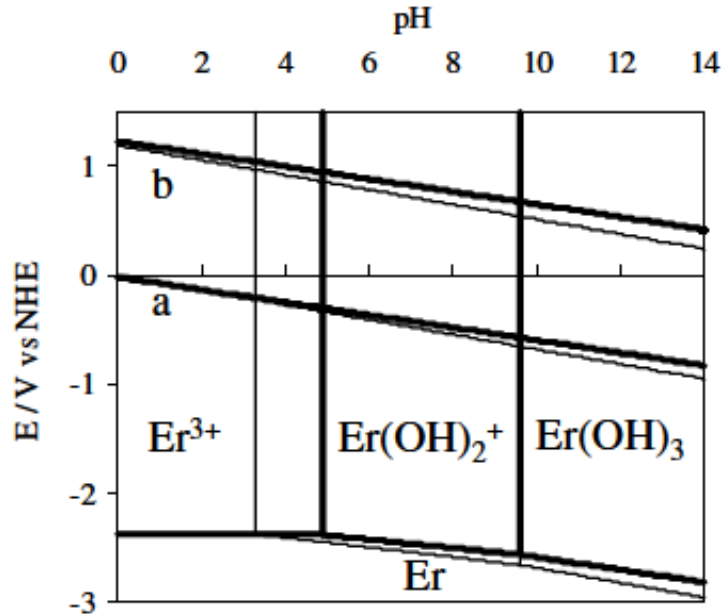
Figure IV. 1 : *E-pH diagram of Er-Cl-H$_2$O system at room temperature* [130]**.**

Figure IV. 2.a) shows a representative example of cyclic voltammograms of a sulfate medium (ZnSO$_4$, Na$_2$S$_2$O$_3$) with different concentration of ErCl$_3$. The obtained curves of the undoped and Er-doped ZnS seems similar, with an increase of the cathodic current density, the current value was -0.28mA/cm² for the undoped ZnS (collected from figure III.14). And the values of the doped film increase from -1.69 to -2.02 mA/cm² by increasing the Er concentration. A similar result was obtained by Goux et al [130]. They studied the effect of Er dopant elements on the ZnO nanostructures. A well-marked cathodic wave is observed below -0.69 V vs. SCE related to the reduction of thiosulfate in to sulfur, a shift of this peak to anodic potential was observed in the curve when the Er^{3+} concentration increase from 10^{-7} to 5.10^{-5}M , that's confirm that the Er^{3+} ions play a catalytic role in the reduction of the thiosulfate ions. This phenomenon is surprising since Er (III) is reported as electrochemically stable over the potential range investigated as mention in the equation below [99]:

$$Er^{3+} + 3e^- \rightarrow Er \quad E_\circ = -2.333V/ENH \qquad \text{(Eq IV.2)}$$
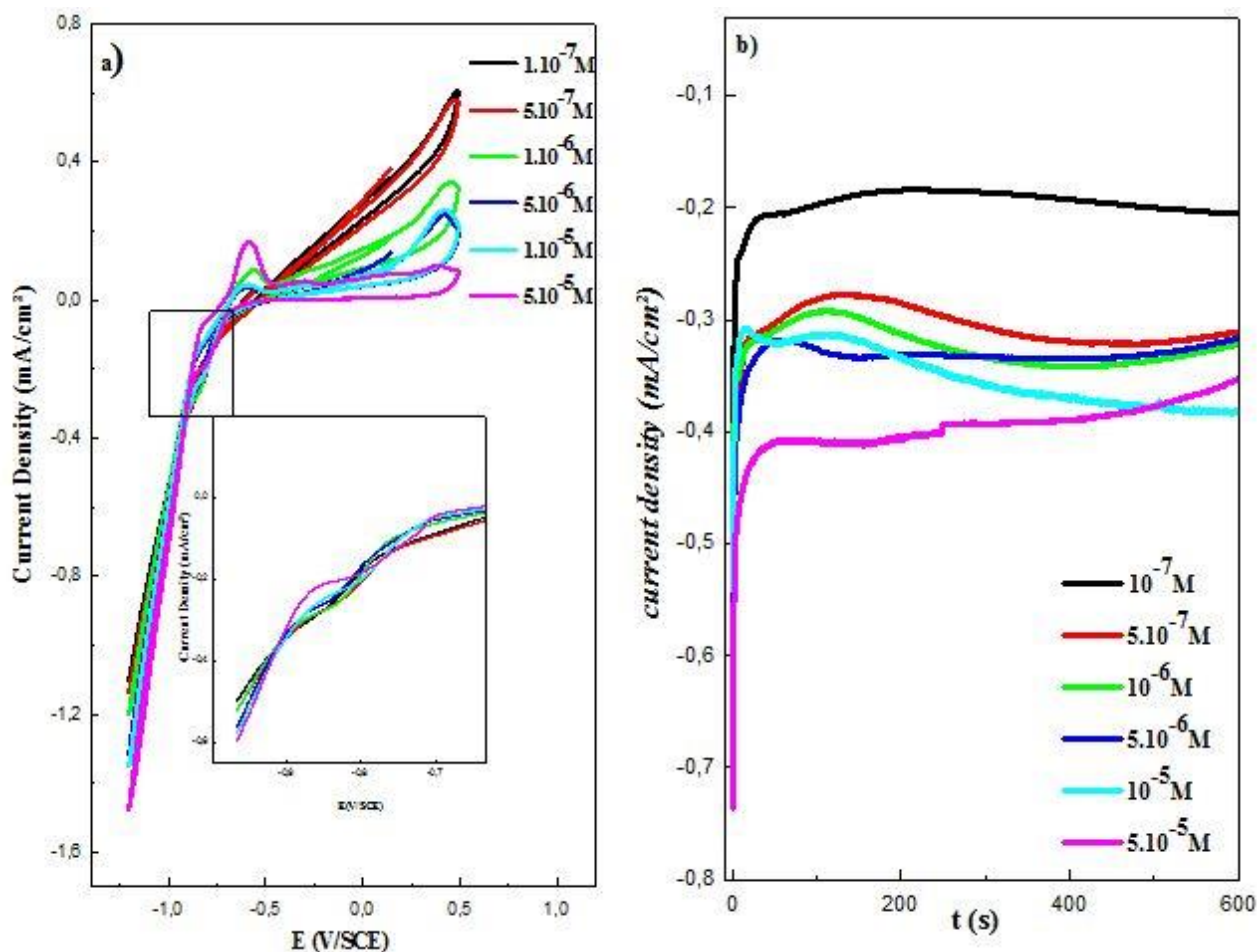
Figure IV. 2: *a) Cyclic voltammograms and b) Typical chronoamperometric curves obtained from bath containing $10^{-3}M$ $Na_2S_2O_3$, $10^{-4}M$ ZnS_4 at different concentrations of $ErCl_3$.*

Figure. IV.3.b shows the evolution of current density after the application of a constant potential of −1V vs SCE. In the presence of erbium in the solution, the deposition bath gives rise to a well-defined nucleation growth behavior. Above 10^{-7} M $ErCl_3$, after a slow decline of the cathodic current density, reaches a constant value. From the previous study (fig. III.15) we can observe that the cathodic current density is higher in the presence of erbium (III). The obtained results confirm that observed by CV.

1.2 Mott-Schottky measurements

Mott-Schottky analysis were used to study the effect of different erbium concentration on the carrier concentration N_D, the flat band potential E_{fb} and the thickness of the space charge area (W) at the ZnS/electrolyte interface. Figure IV.4 shows the Mott-Schottky curves of the ZnS nanostructures obtained at different concentration of $ErCl_3$, achieved in a supporting electrolyte of 0.5 M Na_2SO_4, while the frequency and amplitude are set at 800 Hz and 10 mV/s. The obtained result show that

doping ZnS nanostructures with Erbium has no influence on the conductivity type confirmed by the linear slope of the obtained curves. The origin of n-type conductivity for the undoped ZnS samples has been reported in Chapter III, adding Er as a doping agent causes some changes in the electrical properties of ZnS. A decrease of carrier concentration from 2.63×10^{20} to 0.4×10^{20} cm^{-3} by increasing the Er^{3+} concentration from 10^{-7} to 5×10^{-6} M. Furthermore, the carrier concentration increase. A study has been done to study the effect of rare earth on II-VI semiconductor [131]. From the obtained results, it is expected that Er^{3+} in zinc blende (ZB) cubic ZnS lattice enters in Zn^{2+} sites, in such a way that n-type ZnS layers can be obtained.
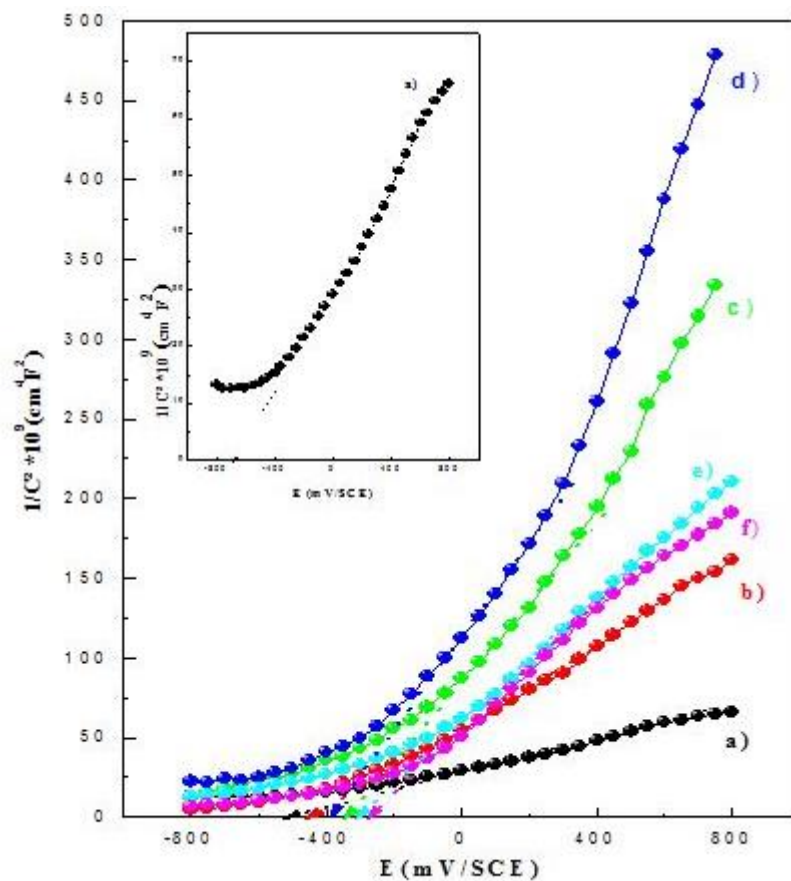
Figure IV. 3: Mott-Schottky plots of the ZnS nanostructures electrodeposited at different concentration of ErCl₃: a) 10^{-7}, b)5.10^{-7}, c) 10^{-6}, d) 5.10^{-6}, e) 10^{-5} and f) 5.10^{-5} M ErCl₃. Insert image is the zoom of the electrodeposited ZnS nanostructures at a) 10^{-7} M ErCl₃.

It is clear that the increase of Er^{3+} concentration from 10^{-7} to 5.10^{-6} M in the ZnS nanostructures causes a shift of the curves towards the positive values of potential while the shift to negative values was obtained for the concentrations greater than 10^{-5} M. Flat band potential can be converted to Fermi level energy using the following equations [132]:

$$E_{fb}(V \ vs \ NHE) = -E_F(eV \ vs \ Vaccum) + V_H(V) - 4.5 \qquad \text{(Eq IV.3)}$$

$$V_H(V) = 0.059(pH_{PZZP} - pH) \qquad \text{(Eq. IV.4)}$$

Where V_H is the Helmholtz layer potential drop and pH_{PZZP} is the point of zero zeta potential. When a literature pH_{PZZP} value of ZnS is (1.7) is used [133], The calculated Fermi levels of n-ZnS may differ slightly from the values estimated from the Mott–Schottky plots. The obtained values of N_D, E_{fb} and E_F was recorder in table IV.1.

Table IV. 1: *Electrical values calculated from M-S plots obtained at different concentrations of $ErCl_3$.*

Sample	E_{fb} *(V/SCE)*	E_{fb} *(V/NHE)*	E_F *(eV vs Vaccum)*	N_D $(10^{20} cm^3)$
00	-0.06	0.17	-3.25	2.43
10^{-7}	-0.51	-0.27	-3.69	3.84
5. 10^{-7}	-0.44	-0.20	-3.62	1.30
10^{-6}	-0.34	-0.09	-3.51	0.62
5. 10^{-6}	-0.38	-0.13	-3.55	0.40
10^{-5}	-0.30	-0.05	-3.47	0.98
5. 10^{-5}	-0.26	-0.01	-3.43	1.01

In the rest of M-S measurements, the flat band potential was also used to calculate band energies (valence band and conduction band) at the ZnS/electrolyte interface according to the following formula:

$$E_{V,S} = E_{C,S} - E_g \qquad \text{(Eq. IV.5)}$$

The ZnS band gap Eg is known (Eg = 3.6 eV) and the energy of the conduction band at the interface of the semiconductor $E_{C, S}$ can be calculated according to the equation [99]:

$$E_{C,S} = q \ E_{fb} + KT \ln\frac{N_C}{N_D} \qquad \text{(Eq. IV.6)}$$

Where N_D is the carrier concentration of donors and N_C is the effective density of conduction band state, calculated using the following equation [134]:

$$N_C = 2\left(\frac{2\pi \ m_e^* kT}{h^2}\right)^{3/2} \qquad \text{(Eq. IV.7)}$$

Where m_e^* is effective mass of electron, k Boltzmann constant, T Temperature, h Planck constant, and $N_C = 6.10 \times 10^{18} cm^{-3}$ [135].

In order to compare the energetics of a redox reaction with those of a semiconductor, we need to express electrochemical potential ($E_{e,\,redox}$) of electrons in solution on a vacuum or absolute scale. As it was reported, $E_{e,\,redox}$ of a redox system is equivalent to the Fermi level $E_{F,\,redox}$ that is [136]:

$$E_{F,redox} = -eE^0_{(SO_4^{2-}/SO_3^{2-})} - 4.5 \qquad\qquad \text{(Eq. IV.8)}$$

The -4.5 represents the energetic level of NHE compared to energy of electron in the vacuum, $E^{\circ}_{(SO_4^{2-}/SO_3^{2-})} = -0.93$ is measured in volts vs NHE. Which gives E^0 the value -3.57 eV.
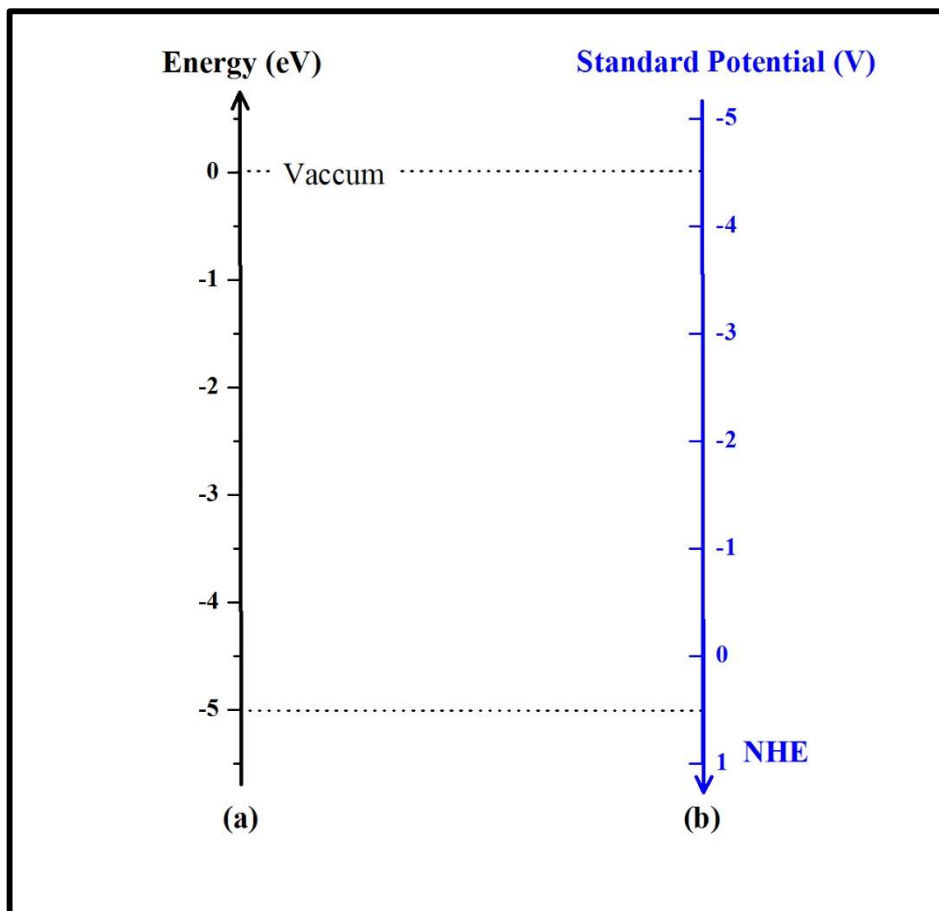
Figure IV. 4: *Correspondence between the two scales of energy; a) In the solid (reference: immobile electron in the vacuum) and b) in the electrolyte (reference: NHE).*

Table IV. 2 : *Experimental values of some physical parameters.*

Concentration	E_{fb} *(V/NHE)*	W (Å)	E_C (eV)	E_V (eV)	U_{bs} (eV)
00	0.17	7.70	-3.03	-6.63	0.54
10^{-7}	-0.37	7.72	-3.47	-7.07	0.10
micro	-0.25	11.25	-3.42	-7.00	0.15
10^{-6}	-0.09	11.09	-3.25	-6.85	0.32
5.10^{-6}	-0.13	16.6	-3.27	-6.87	0.30
10^{-5}	-0.05	6.57	-3.22	-6.82	0.35
5.10^{-5}	-0.01	2.89	-3.17	-6.77	0.40

The calculation of those parameters, allow us to draw the diagram of band energy corresponding to the interface ZnS, (SO_4^{2-}/SO_3^{2-}) redox couple. Figure IV. 5 shows afterward the energy representation of all the quantities defined above in case of ZnS as well as for the (SO_4^{2-}/SO_3^{2-}) redox couple before the contact to the electrolyte. Dipping the semiconductor electrode to the electrolyte, introduce an exchange of the electrons between the two phases until the equilibrium condition is reached. Indeed, electrons are transferred by tunneling effect from the phase with a smaller work function to that with higher work function. For the semiconductor, the work function of electrons is given by Fermi level in the semiconductor. While that of electrolytes is determined by the couple redox potential, this redox potential is also identified with Fermi level of the electrolyte. The callibration of the two Fermi levels occurs by transfer of electrons from the semiconductor to the electrolyte, this produces a positive space charge region in the semiconductor. While, in the electrolyte side a negative zone is developed, thus it appears a potential barrier for the electrons "in the electrolyte side". The height of Schottky potential barrier U_{sb} is given by the difference between the electrochemical potential of the solution (E_e) and the electronic affinity χ [133].

$$U_{bs} = E_e - \chi \qquad \qquad \text{(Eq. IV.9)}$$

The calculated values of U_{bs} was recorded in the table IV. 2.
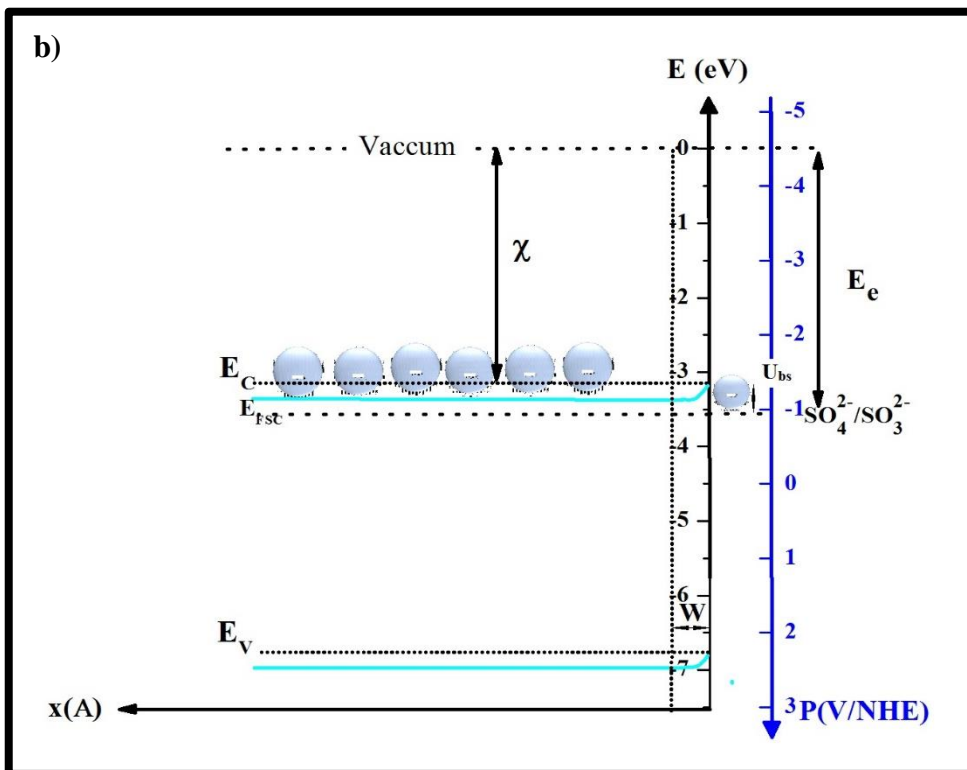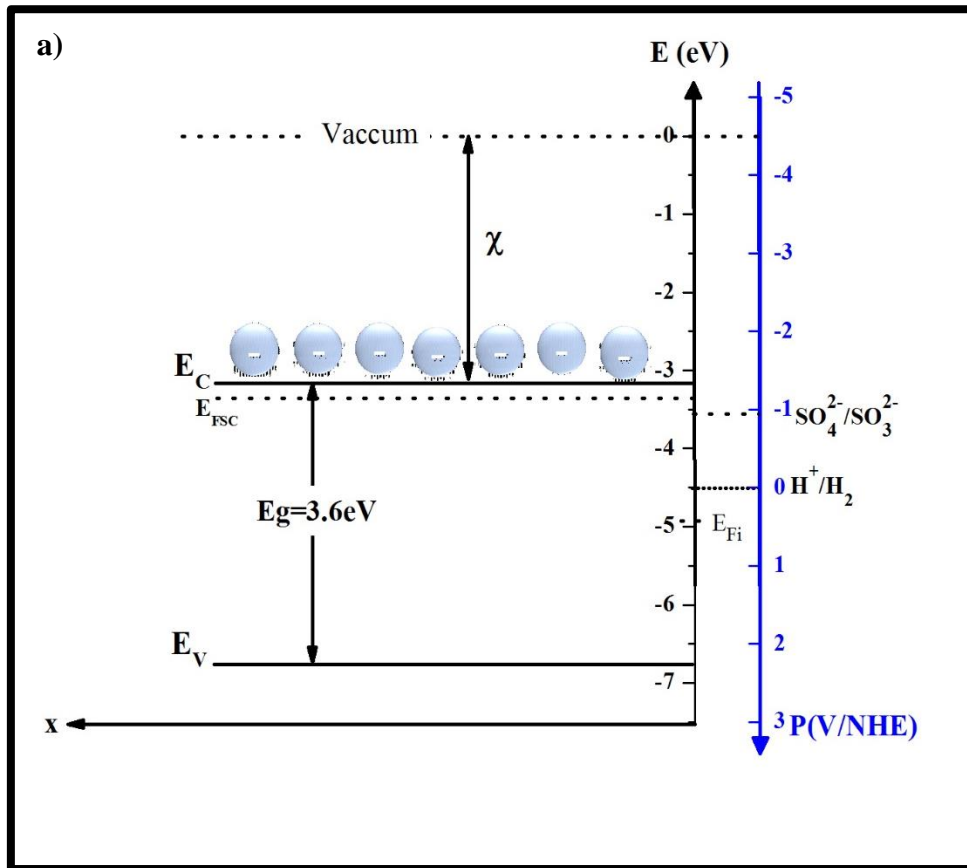
Figure IV. 5: *a) Energy diagram of the ZnS bands and the level of Redox couple and b) Band diagram corresponding to the equilibrium of the ZnS electrode in a solution of 0.5 M Na$_2$SO$_4$.*

1.3 Crystal structure

Figure IV. 6 shows the XRD patterns of the electrodeposited films. The addition of a small amount of erbium ions into the precursor solution does not change the crystal structure of the samples. All the undoped and Er doped ZnS films have a Blende type structure, oriented along the (200) plane. No extra diffraction peaks from Er-related second phase is observed (Er(OH$_3$) or Er$_2$O$_3$). This may be explained by the fact that Er^{3+} ions substituted for Zn^{2+} ions in the ZnS host semiconductor without changing the structure. The (200) peak position shifted to lower angle compared to the undoped ZnS film (Fig.IV.6). This means that the lattice parameter increases with Er doping, which is an expected result. Because the ionic radius of Zn^{2+} (0.74 Å) is smaller than the ionic radius of Er^{3+} (0.89 Å) and the larger lattice constant denotes that Er^{3+} ion incorporates into the ZnS lattice and substitutes the Zn^{2+} site. The incorporation of this latter is more effective in Cd (0.95 Å) chalcogenides than in Zn chalcogenides. The bigger radius of the Er^{+3} atom alters the (200) interplanar distance *d*, that gives place to the distortion of the ZB-ZnS lattice. Triply ionized Er atom in cubic CdS [137], CdTe, ZnO [138] and ZnSe [139] enters substitutionally in cation sites and interstitially in symmetric octahedral interstitial positions. We have assumed that both substitutional, and interstitial sites of Er^{3+} occur on ZB-ZnS. In the case of substitution, the Er^{3+} ion is surrounded by four S^{2-} neighbors same as in the positions occupied in the perfect crystal. While in the second case the Er^{3+} are placed in the interstitial site surrounded by a tetrahedron of four Zn^{2+} ions and 6 S^{2-} ions [139].
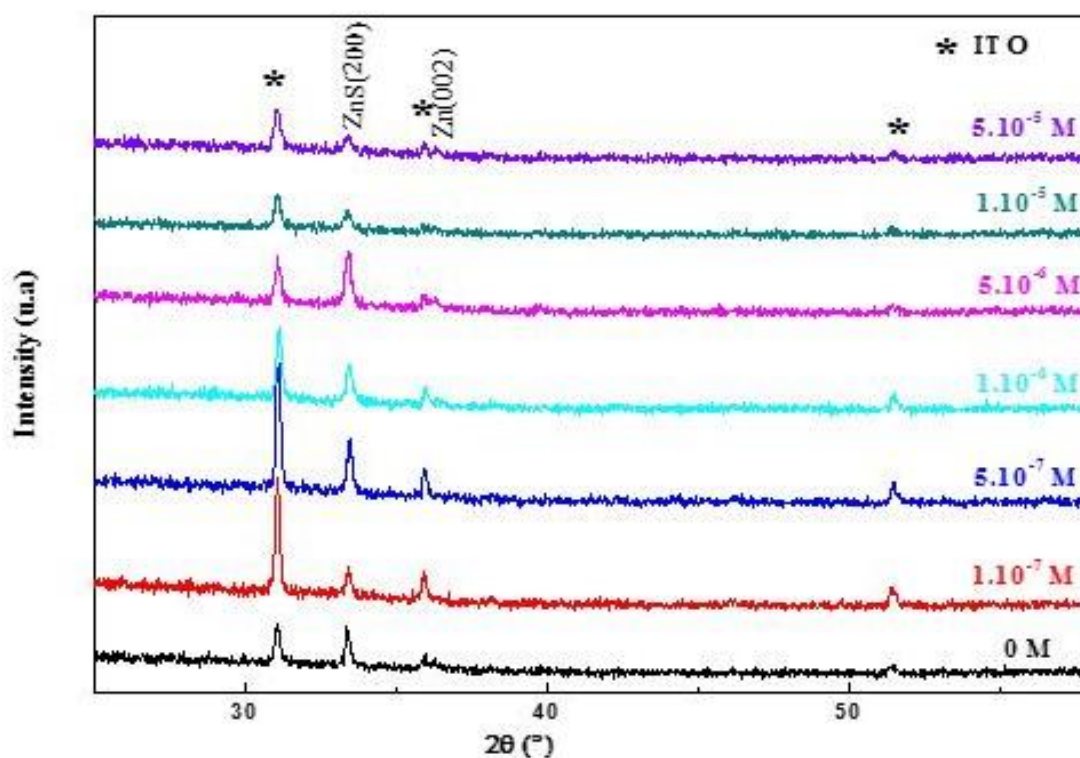
Figure IV. 6 : *XRD patterns of the undoped and Er-doped ZnS nanostructures.*

Table IV. 3: *Microstructural parameters of the Er doped ZnS*

samples	FWHM (°)	2Θ (°)	$d_{hkl}(Å)$	a (Å)	V ($Å^3$)	D (nm)	$\varepsilon \times 10^{-2}$
00	0.219	33.01	2.711	5.42	159.44	75.43	10.52
10^{-7}	0.213	33.00	2.712	5.42	159.59	77.60	10.23
5.10^{-7}	0.206	32.98	2.713	5.42	159.87	80.35	9.86
10^{-6}	0.248	32.93	2.717	5.43	160.58	66.69	11.91
5.10^{-6}	0.256	32.89	2.720	5.44	161.15	64.51	12.31
10^{-5}	0.300	32.88	2.721	5.44	161.29	55.20	14.39
5.10^{-5}	0.305	32.87	2.722	5.44	161.38	54.20	14.65

Previously, the XRD results of the undoped ZnS nanostructures elaborated with different parameters show the presence of metallic zinc impurities. Doping ZnS with Er (10^{-7} to 10^{-6} M) avoid the presence of Zn, beyond the concentration of Er^{3+} 5×10^{-6} the zinc impurities turn back. The

increasing of Er concentration leads to deterioration of the ZnS crystal structure, this is associated with the formation of the amorphous structure.
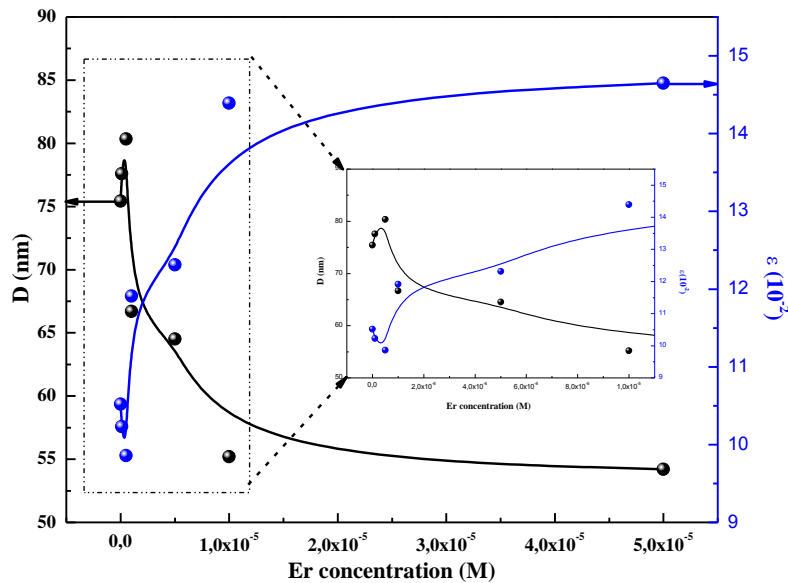
Figure IV. 7: *Variation of crystallites size and microstrain of the obtained films at different concentrations of Er³⁺.*

    The average volume (V) and the crystallite size (D) determined from the peak position (200) of the cubic structure of all the deposits film are collated in table IV.3. The volume of the undoped and doped ZnS at different concentrations of erbium has been calculated by the following relation [140]:

$$V = a^3 \tag{Eq. IV.9}$$

In the Figure IV. 5 we report the variation of the crystallite size and microstrain as a function of Er concentration. According to this last figure, the crystallites size of the ZnS nanostructures increases for the concentration between 0 to 10^{-6} M Er then it decreases. In addition, it has been observed that the micro-strain values are increased. This clearly shows that the incorporation of Er to the ZnS matrix affects the crystalline structure.

1.4 Optical charasterizations

1.4.1 Ultra Violet Visible spectroscopy

    The transmittance-wavelength graph of the undoped and Er doped ZnS nanostructures is shown in figure IV. 8. According to the optical transmission spectrum, a sharp absorption is observed

in the wavelength range between 200-310 nm. When Er ions are incorporated into the ZnS structure, a significant shift is not observed in the absorption edge.

It is observed that the average optical transmittance is about 80 % in the visible region, it exhibits an absorption edge at a wavelength of about 350 nm for undoped ZnS film. The average transmittance values of all doped ZnS films are above 60 % and their transmittances are higher than undoped ZnS sample. The transmittance of ZnS based nanostructures can be affected by defects such as film thickness, surface roughness and grain size.
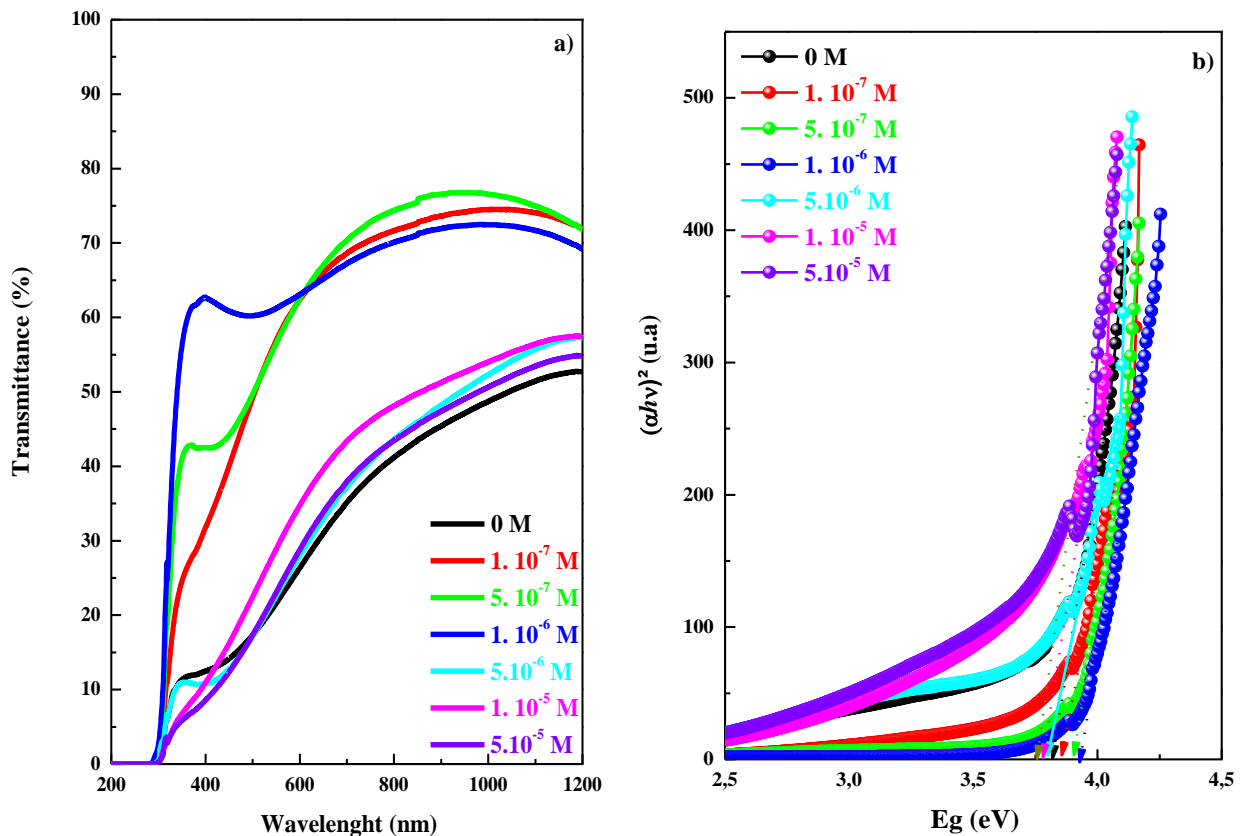
Figure IV. 8: *a) Optical transmission spectra and b) Tauc plots of ZnS nanostructures doped with different concentrations of Er.*

Tauc's plots of function $(\alpha h\upsilon)^2$ versus to energy $(h\upsilon)$ for ZnS and ZnS:Er nanostructures are given in figure IV. 8. The optical band gap energy (Eg) values for undoped and Er doped ZnS nanostructures are calculated using the formula:

$$(\alpha h\upsilon)^2 = A(h\upsilon - E_g) \qquad\qquad\qquad \text{(Eq. IV.10)}$$

Where A is constant, α is the absorption coefficient, is the discrete photon energy, Eg is the band gap energy, and n depends on the type of optical transmission in the band gap. n=1/2 is for direct band gap crystalline semiconductors. The Tauc plot which is extrapolating the linear portion to zero

absorption coefficient gives the optical band gap energy of the films. While the optical band gap energy is about 3.74 eV for undoped ZnS film, it is in the range of 3.74-3.94 eV for Er doped nanostructures as shown in figure IV. 8. Bandgap energy of the doped films is bigger than the undoped film. The optical absorption edge has a blue shift to the region of higher photon energy with an increase in Er concentration. The blue shift behavior in the band gap can be attributed to an increase in the carrier concentration that blocks the lowest states in the conduction band, known as the Burstein–Moss effect. An increase in the carrier concentration in Er doped ZnS will cause the Fermi level to move into the conduction band. Therefore, the low energy transitions are blocked [20, 21]. The filling of the conduction band by electrons generally causes a blue shift in the band gap.

1.4.2 Time resolved photoluminescence

Time resolved photoluminescence decay of undoped and ZnS doped with Er ions is shown in figure IV. 9. The decay curves can be fitted into bi exponentials. The decay times are indicative of donor–acceptor pair recombination. It can be noted that undoped ZnS sample has comparatively fast decay, doping increases its decay time as shown in figure IV. 9. The decay times of each sample at peak emission wavelength under UV excitation and relative contribution of each component are listed in table IV. 4.
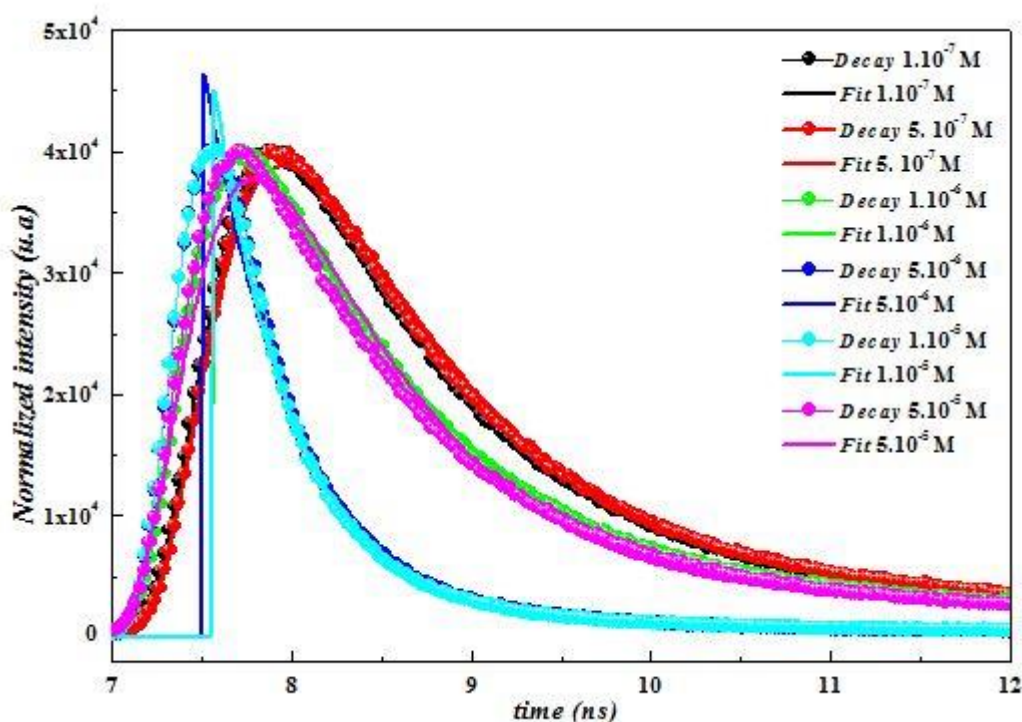
Figure IV. 9: *A set of spectrally integrated Time resolved photoluminescence curves of the ZnS:Er films measured at room temperature. The symbols are measurement data, and the solid lines are corresponding bi-exponential fits.*

To further explore the effect of the charge carrier transfer of ZnS with the Er doping, TRPL measurements were conducted and are shown in figure IV. 9. All the decay curves can be well-fitted to a bi-exponential function described by the equation reported in the previous chapter.

Table IV. 4 *:* Best Fit Values of τ_1, and τ_2 and of the Relative Weights A1 and A2 for the films deposited at differents ErCl3 concentration.

Concentration	τ_1	B1	τ_2	B2
10^{-7}	9.14×10^{-10}	67.90	6.24×10^{-9}	32.1
5.10^{-7}	9.17×10^{-10}	67.70	6.34×10^{-9}	32.3
10^{-6}	8.28×10^{-10}	69.59	4.33×10^{-9}	30.41
5.10^{-6}	4.28×10^{-10}	96.91	3.45×10^{-09}	3.09
10^{-5}	4.02×10^{-10}	99.28	2.32×10^{-9}	0.72
5.10^{-5}	8.61×10^{-10}	72.99	4.54×10^{-9}	27.01

IV.2 Samarium doped ZnS

In the second part we are going to present the obtained results of the Sm doped ZnS thin film stating by the electrochemical study than the morphological structural and optical properties. The following table summarizes the different concentration of the $SmCl_3$ used during the deposition of Sm doped ZnS nanostructures.

2.1 Electrochemical reactions and doping

Cyclic voltammograms (CVs) were recorded for all the Sm doped ZnS films with linear potential sweep between 0.5 and -1.2 V at scan rates 20 mVs^{-1} in the electrolyte of 10^{-3} M $Na_2S_2O_3$ and 10^{-4} M $ZnSO_4$ with respect to SCE. From the figure IV. 10 we can see that Sm doping has an obvious influence on the ZnS nanostructures. The increasing of the Sm doping amount from 10^{-7} to 5×10^{-5} M lead to reduce the current density as it was observed in the figure IV. 10. a). A previous study was done by Niu et al. where they doped TiO_2 by two rare earth (Sm and Ce) [141]. Adding Sm as dopant had a great influence on the TiO_2, the addition of this latest with a small amount enhances the formation of the product compared to that without adding it. In our case, we had found the same result to that obtained for doping TiO_2 by Sm. Whereas increasing the Sm amount from 10^{-7} to 10^{-6} M fast forward the reduction of thiosulfate ions, confirmed by the anodic shift of this peak. On the other side, when we increase the concentration more than 5×10^{-6}M we observe a cathodic shift

was obtained, which mean that when we enhance the concentration more than 5×10^{-6} give an opposite effect.
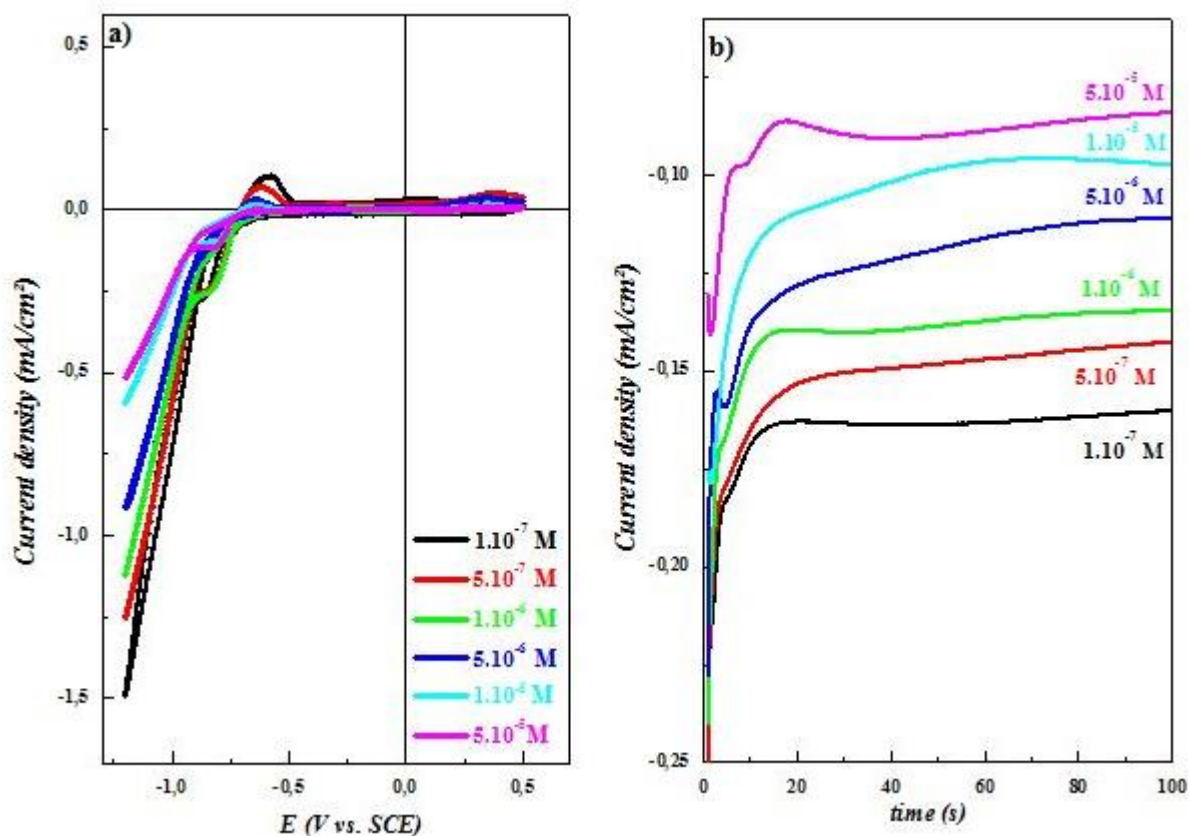
Figure IV. 10: *a) Cyclic voltammograms and b) Typical chronoamperometric curves obtained from bath containing $10^{-3}M$ $Na_2S_2O_3$, $10^{-4}M$ ZnS_4 at different concentrations of $SmCl_3$.*

Chronoamperometric measurements were made at various bath concentrations of $SmCl_3$ to explore the nucleation and growth process associated with electrochemical deposition of the Sm doped ZnS. Figure IV. 10. b) represents a series of current–time transients for the deposition of the Sm doped ZnS in different concentrations of $SmCl_3$. The shape is typical of a 3D electrocrystallization growth process, the current density decreases with increasing Sm concentration. This result confirms that obtained by CV measurements.

Table IV. 5: *Experimental values of some electrical parameters.*

Doped concentration	N_D (10^{20}cm^{-3})	E_{fb}(V/SCE)	E_{fb}(V/NHE)	E_F (eV vs Vaccumm)
10^{-7}	1.68	-0.18	0.06	-3.36
5×10^{-7}	1.35	-0.22	0.02	-3.40
10^{-6}	1.30	-0.25	-0.01	-3.43
5×10^{-6}	1.21	-0.30	-0.06	-3.48
10^{-5}	0.82	-0.33	-0.08	-3.50
5×10^{-5}	0.56	-0.49	-0.24	-3.66

2.2 Mott-Schottky measurements

In order to study the effect of the Sm dopant concentration on the carrier density N_D and the flat band potential $E_{fb,}$ the Mott-Schottky analysis was employed. Figure IV. 11 represents the obtained M-S plots for the Sm doped ZnS nanostructures at different concentration of SmCl$_3$, achieved in a supporting electrolyte of 0.5 M Na$_2$SO$_4$, while the frequency and amplitude are set at 800 Hz and 10mV/s. the linear slope of the obtained curves confirms that doping with Sm doesn't have an effect on the conductivity type. The calculated carrier concentration was reported in the table IV. 5, we observe that the increase of the Sm amount reduces the carrier concentration value. While the curves shift towards the negative values of potential.
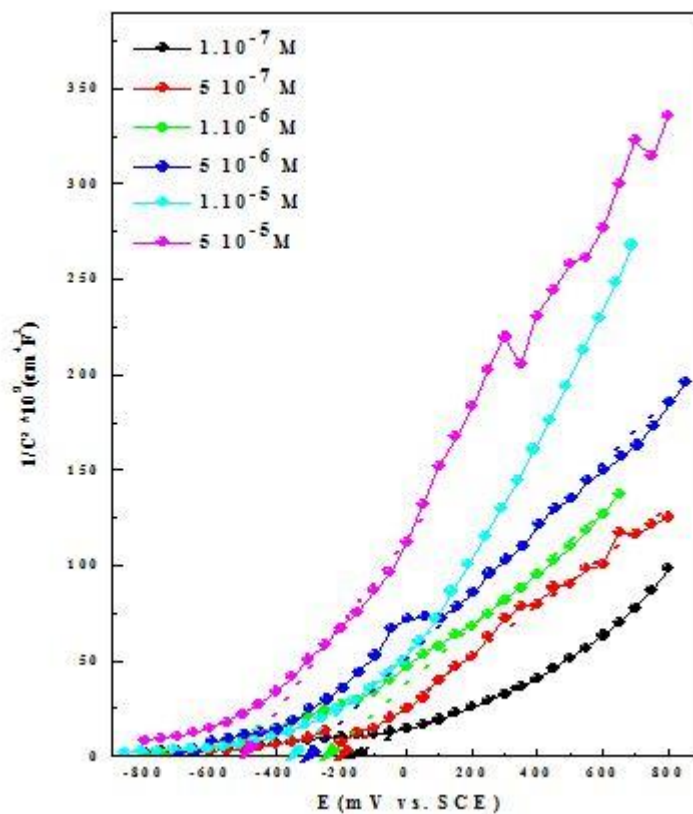
Figure IV. 11: *Mott-Schottky plots of the ZnS nanostructures electrodeposited at different concentration of SmCl₃.*

In order to study the effect of the presence of samarium in the ZnS lattice, we had used the flat band potential to calculate different parameters such as W, Ec, Ev and U_{bs}. It is also noted that the space charge region (W) decrease by increasing the amount of the Sm from 10^{-7} to 10^{-6} M, when we increase the amount of Sm more than 10^{-6} M we observe the opposite effect the increase in this area was explained by the decrease of the carrier concentration in the semiconductor.

Table IV. 6: Experimental values of some physical parameters.

Sm concentration (M)	E_{fb}(V/NHE)	W(Å)	E_C (eV)	E_V (eV)	U_{bs}(eV)
10^{-7}	0.061	5.55	-3.12	-6.72	0.44
5.10^{-7}	0.023	3.80	-3.15	-6.75	0.42
10^{-6}	-0.010	2.55	-3.18	-6.78	0.39
5.10^{-6}	-0.061	6.54	-3.23	-6.83	0.34
10^{-5}	-0.087	9.48	-3.25	-6.85	0.32
5.10^{-5}	-0.248	19.38	-3.40	-7.00	0.17

2.3 Morphology analysis

The surface morphology of the deposited films was investigated by AFM analyses. The ZnS:Sm nanostructures exhibit a fairly uniform distribution of grains with a smooth surface. The surface of the films has firmly packed grains without any voids and cracks. It was observed when the Sm concentration increases from 10^{-7} to 10^{-5} M, the root means square decrease.it is clearly noted that the Smooth of the coating surface increase as a result of increasing Sm doping utile 10^{-5} M.

These results indicate that the surface of the Sm doped ZnS film is smoother than that of the undoped ZnS films. A more scattered structure is noticed and the average surface grain size slightly decreases with the increase of the concentration. The opposite effect was observed for the concentration of 5×10^{-5} M.
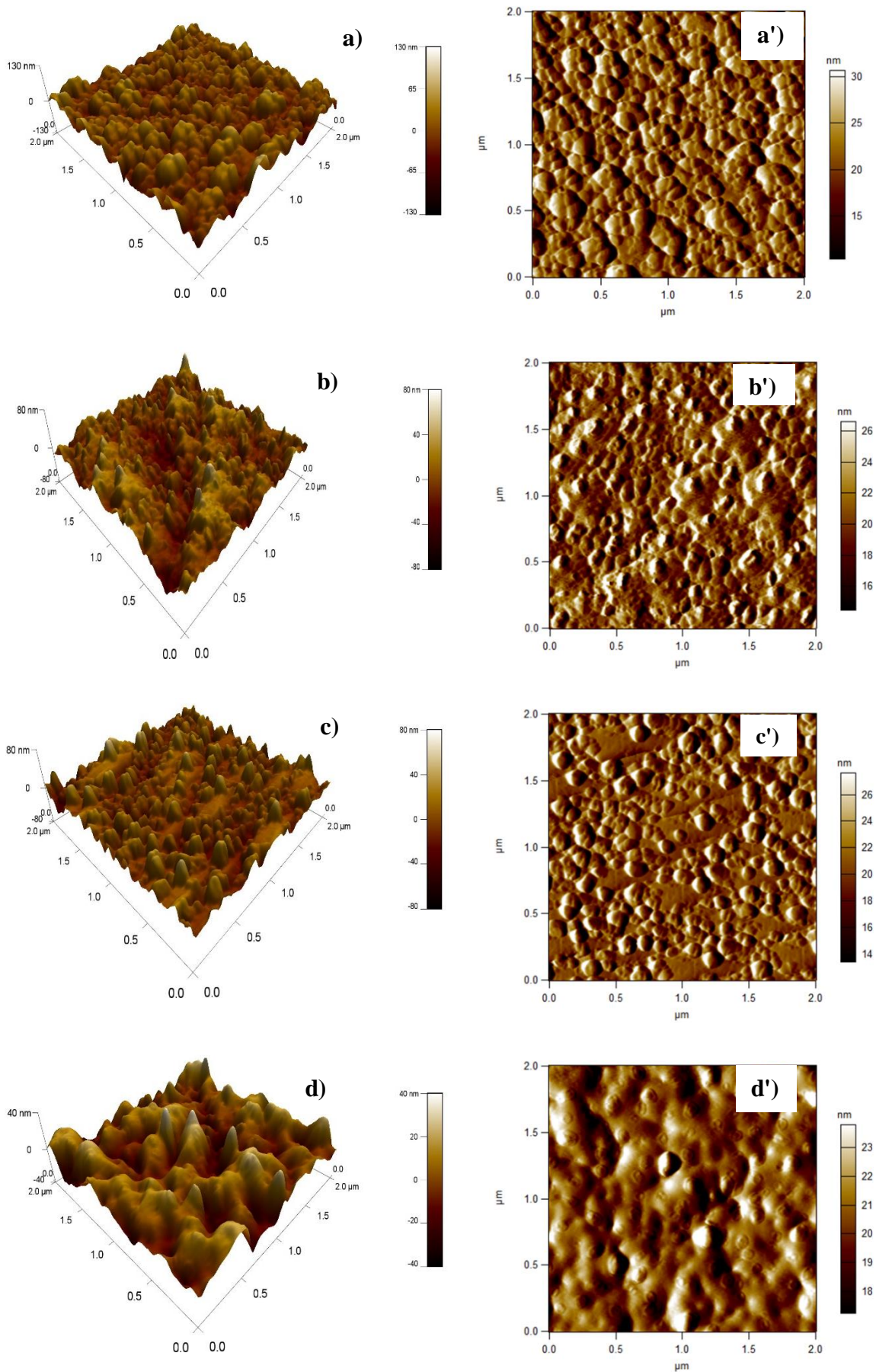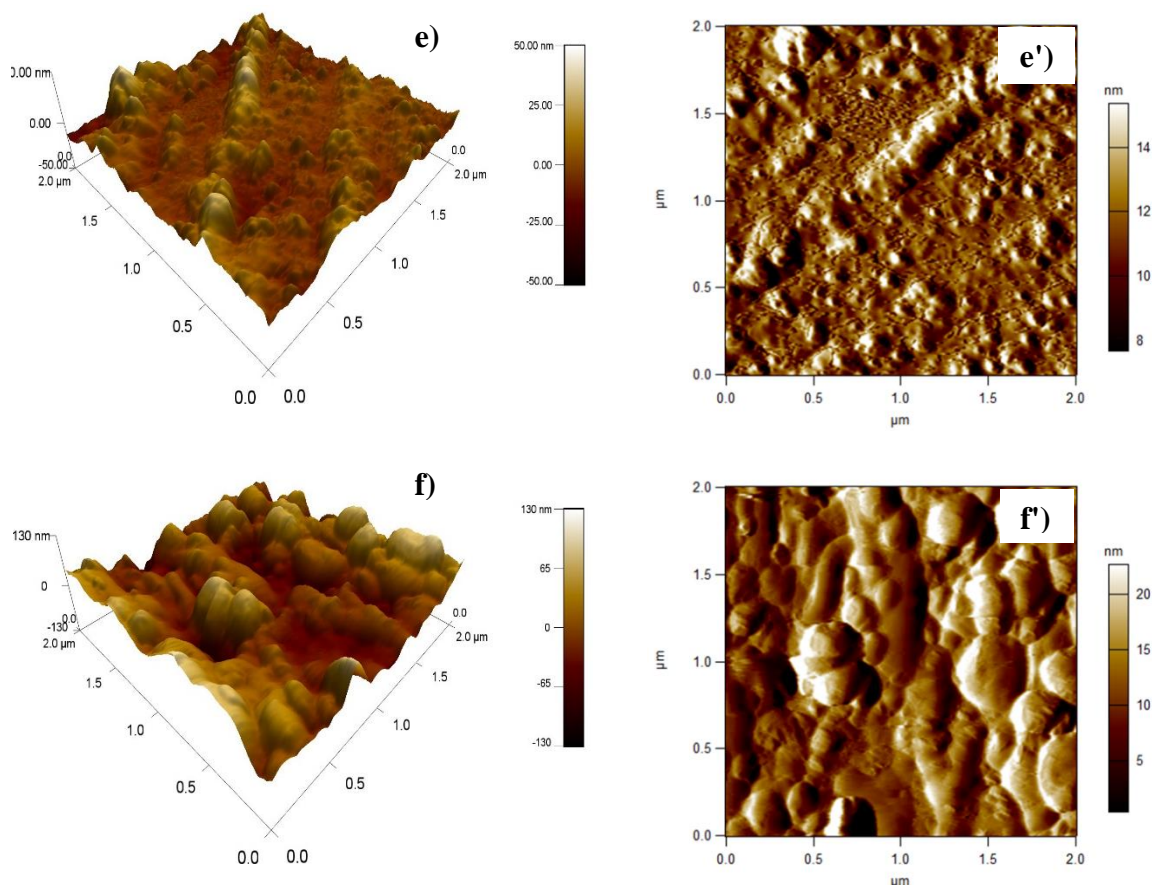
Figure IV. 12: *2D and 3D images atomic force microscopic images of ZnS nanostructures electrodeposited of the samples doped with different Sm concentration a), a') 10^{-7}, b), b') 5×10^{-7}, c), c') 10^{-6} d), d') 5×10^{-6}, e), e') 10^{-5} and f), f') 5×10^{-5} M.*

2.4. Crystal Structure

Figure IV. 12 illustrates the XRD patterns of the Sm-doped ZnS nanostructures. The main dominant peak was identified for pure ZnS at around $2\Theta°$ value of $32.93°$ which are related to the (200) plane of cubic blende ZnS (JCPDS Card-05-0566), without any diffraction peaks from samarium oxides or other impurities. The diffraction value of the diffracted plane revealed a shift to lower angles in the case of the Sm-doped ZnS in comparison with the pure ZnS (Fig. III. 25), indicating the insertion of Sm^{3+} ions into the ZnS.
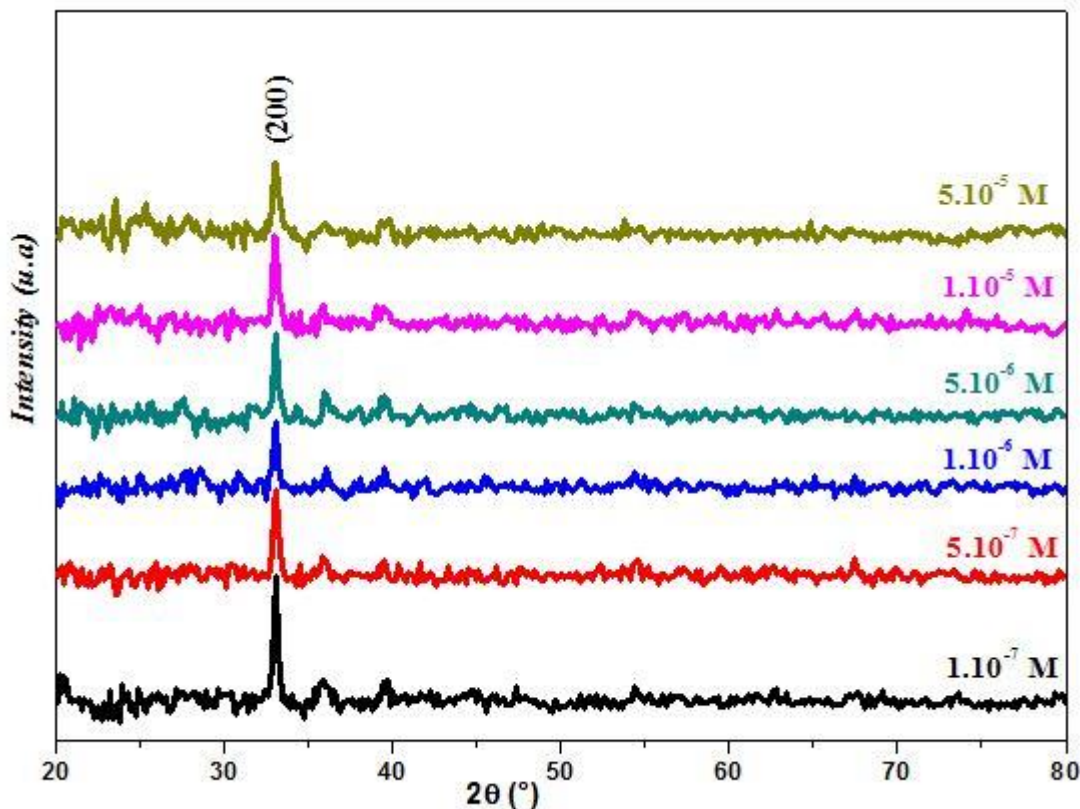
Figure IV. 13: *Diffractograms of ZnS:Sm electrodeposited on ITO at different concentrations of Sm^{+3}ions.*

This shift can be described by the expansion of the ZnS lattice through samarium doping due to the larger ionic radius of Sm^{3+} (0.964 Å) compared to Zn^{2+} (0.74 Å). Suggesting that Sm^{3+} ions are uniformly substituted into the Zn^{2+} sites in the lattices of ZnS [142], [143].

The average crystallite size of samarium doped ZnS nanostructures was determined from the broadening of XRD peak using the Scherer's formula. The estimated average crystallite size of samarium doped ZnS is given in table IV. 7. It is observed that there is a variation in the crystallite size of ZnS nanostructures from 44 to 33 nm when the concentration of Sm^{3+} ion varies from 10^{-7} to 5×10^{-5}M. The presence of different concentration of Sm^{3+} ion in the ZnS lattice might cause various effects such as influenced on the native defects or segregate the Sm^{3+} ion in the grain boundaries [142].

Table IV. 7: *Microstructural parameters of the Sm: ZnS nanostructures.*

Sm concentration (M)	FWHM (°)	2Θ(°)	d_{hkl} (Å)	A (Å)	D (nm)	Eg (eV)
10^{-7}	0.335	32.93	2.717	5.435	44.94	3.61
5.10^{-7}	0.346	32.90	2.720	5.440	43.64	3.63
10^{-6}	0.346	32.89	2.720	5.441	43.63	3.78
5.10^{-6}	0.370	32.89	2.720	5.441	40.76	3.69
10^{-5}	0.370	32.88	2.721	5.443	40.79	3.69
5.10^{-5}	0.453	32.86	2.723	5.446	33.30	3.69

2.5 Optical properties

2.5.1 Ultra Violet Visible spectroscopy

For further investigating the influence of Sm doping process on ZnS optical transmittance, UV-visible spectroscopy was used to study the change of transmittance. As shown in figure IV. 14, all the films exhibit a sharp fundamental absorption edge in the range of 200-325 nm can be attributed to the intrinsic band gap of pure ZnS (≈ 3.7 eV), which was generally associated with the electronic excitation of the valence band S 3p electron to the conduction band Zn 4s level. It was easy to observe that the presence of Sm^{3+} ions in the ZnS lattice made the absorption band edge shift toward shorter wavelength, namely bleu shift, which meant the Sm-doped ZnS nanostructures possessed a narrower band gap that was good for transmitting sunlight. So adding small amount of samarium lead to increase the transmittance as shown in the figure IV.14.
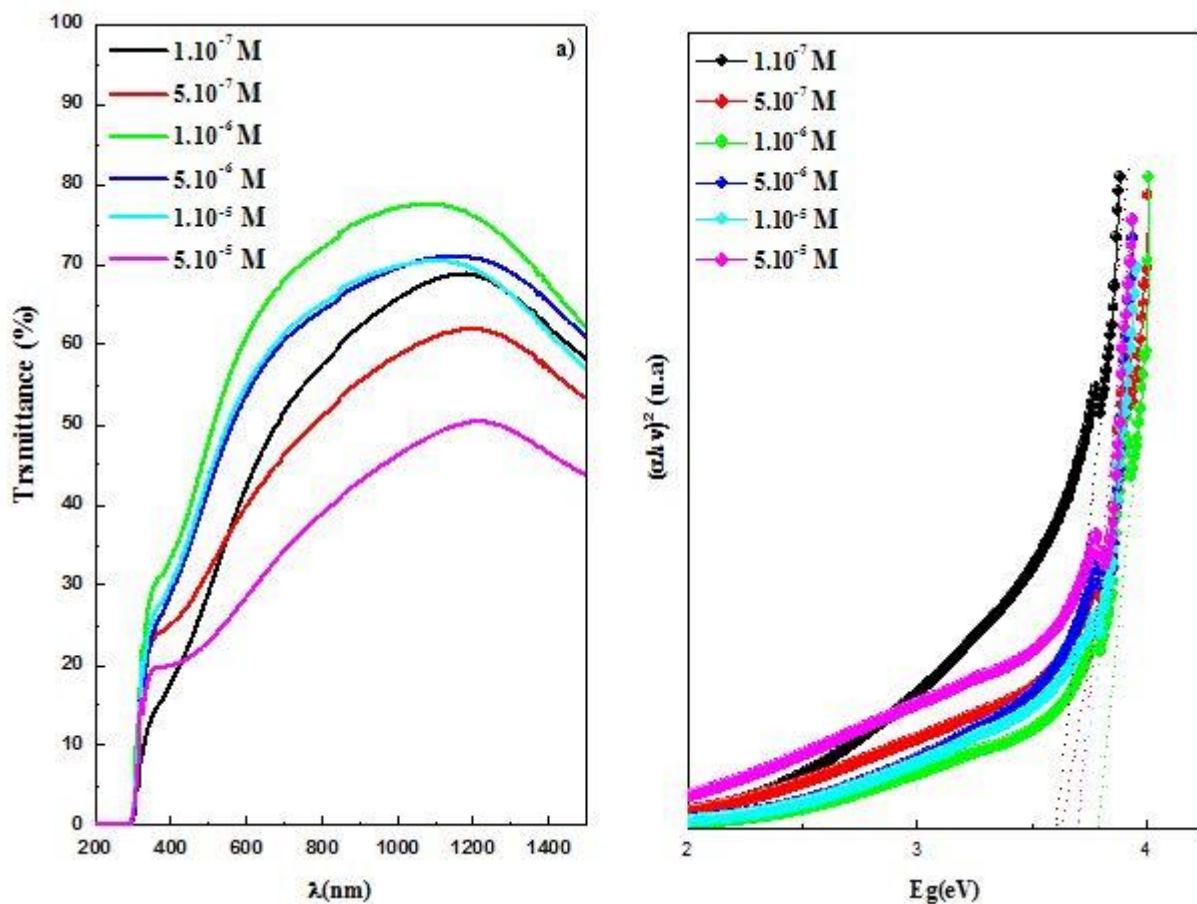
Figure IV. 14: *a) Optical transmission spectra and b) Tauc plots of ZnS nanostructures electrodeposited at different concentrations of Sm.*

2.4.2 Time resolved photoluminescence

Time resolved photoluminescence decay spectra recorded for Sm doped ZnS nanostructures were fitted into bi exponentials due to the emission from bi-level trapping states. Figure IV.15 shows the luminescence spectra recorded for Sm doped ZnS nanostructures. Two values of decay time have been calculated from each spectrum. The faster of the two calculated lifetime is interpreted to be due to the recombination transitions from shallow trapping levels, whereas the longest lifetime is tentatively attributed to the decay from the deeper levels of the respective set of traps.
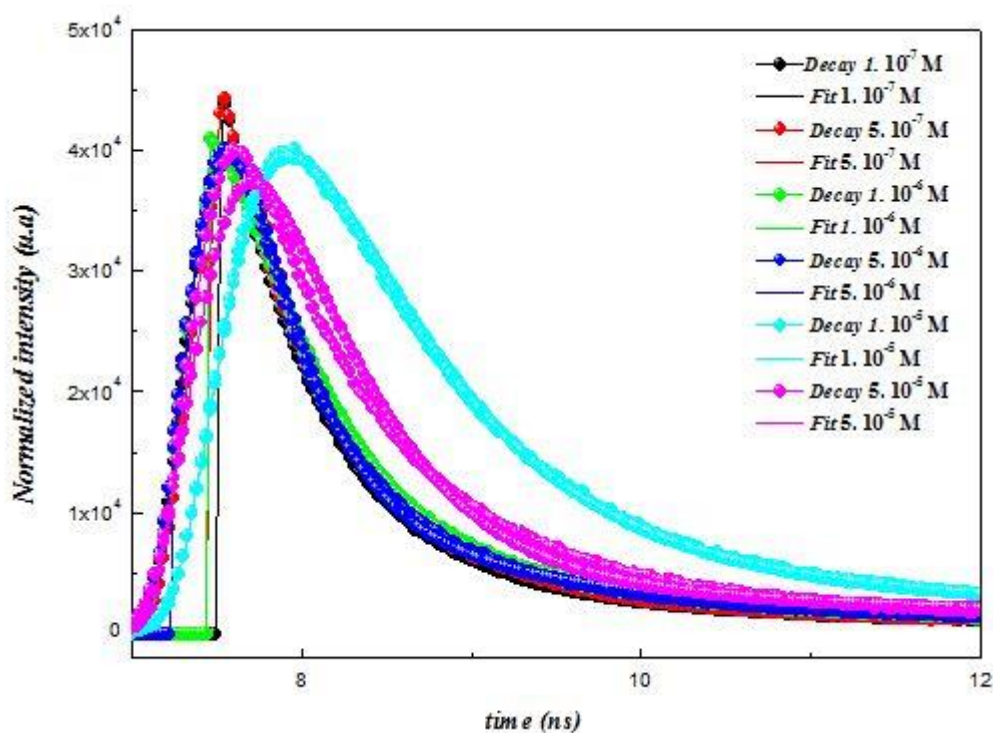
Figure IV. 15: *A set of spectrally integrated TRPL curves of the ZnS:Sm films measured at room temperature. The symbols are measurement data, and the solid lines are corresponding bi-exponential fits.*

Table IV. 8: *Best Fit Values of τ_1, and τ_2 and of the Relative Weights A1 and A2 for the films deposited at differents SmCl₃ concentration.*

Sm concentration (M)	τ_1 (s)	B_1 (%)	τ_2 (s)	B_2 (%)
10^{-7}	$5.99\ 10^{-10}$	71.02	$2.91\ 10^{-9}$	28.98
5.10^{-7}	$6.43\ 10^{-10}$	73.4	$3.11\ 10^{-9}$	26.6
10^{-6}	$4.25\ 10^{-10}$	68.13	$2.18\ 10^{-9}$	31.87
5.10^{-6}	$1.61\ 10^{-10}$	60.44	$1.54\ 10^{-9}$	39.56
10^{-5}	$7.95\ 10^{-10}$	65.72	$4.10\ 10^{-9}$	34.28
5.10^{-5}	$4.87\ 10^{-10}$	66.12	$3.87\ 10^{-09}$	33.88

IV.3 Summary

In this chapter, we had shown the effect of rare-earth doping on the ZnS nanostructure. A significant influence on the different properties of the ZnS nanostructures was obtained by electrodeposition on an ITO substrate.

The most significant results are summarized as follows:

➢ Comparing the voltammetry curves obtained at different concentrations of Er and Sm. it shows that the Er^{3+} and Sm^{3+} ions reduce the reduction reaction of $S_2O_3^{2-}$ and Zn^{2+}. From the Mott Schottky measurements, the estimation of the carriers charges density confirms the decrease of the conductivity of the ZnS deposits with different Er and Sm doping.

➢ X-ray diffraction analysis showed that all the samples of Er: ZnS and Sm: ZnS have a Cubic structure of Blende type having a preferential orientation along the direction (200). The increase in Er and Sm concentration led to a decrease in the average crystallites size, a very marked deterioration of the crystallinity. The results obtained by DRX confirm the substitution of the Zn^{2+} ion by the Er^{3+} and Sm^{3+} ion in the ZnS crystal lattice.

➢ Doping with Er and Sm improve the transparency of the obtained nanostructures.

Conclusion

This work focuses on the electrodeposition and characterization of undoped and doped zinc sulfide nanostructures (ZnS) on ITO glass substrate. The effect of different deposition parameters was studied to get a good quality which can be used in several applications such as: solar cells and gas sensor. The investigated parameters in this study were: zinc concentration, pH, applied potential and deposition time. The investigation of zinc concentration lead to even we reduce the concentration from 10^{-3} to 10^{-4} M of $ZnSO_4$ a good quality of films was obtained, Mott-schottky plot's show a positive slope indicate the n-type of the obtained films, the obtained nanostructures crystallize with zinc blend structure for both concentration with the crystallite size was 63.48 and 93.55nm and we observe the presence of some Zn impurity in the XRD results. The resulted films shows a low transmittance, this is related to the technique and the presence of Zn impurities, the optical band gap increase when we decrease the $ZnSO_4$ concentration. However, the films deposited at different pH grow with high growth rate. The SEM images show a uniform and homogenous films, when the XRD exhibits a zinc blende structure with the presence of zinc metallic in the diffractogramms.

When we run cyclic voltammetry we observe two large peaks related to the reduction of different species presented in the solution that's why a range of applied potential was studied (from -1 to -1.3V/SCE). The results was correlated, the Mott-Schottky measurement show a high carrier concentration values (10^{21} cm^3), when we increase the applied potential an increase of crystallite size was obtained (which mean the improvement of crystallinity). A large band gap was estimated from transmittance curves (3.54-3.74 eV) at the end of this part the effect of deposition time was presented, XRD show the presence of the preferential orientation (111) which is rarely obtained by electrodeposition, the variation of the deposition time is varied from 10 to 30 min, this last parameters show an improvement of the obtained nanostructures, high transmittance value (70 %) comparted with previous results.

In the second part of this work, Er and Sm doped ZnS thins films was presented. The measurements carried out by the Mott-Schottky technique for the Er and Sm doping have shown that all samples have an n-type conductivity. These measures have also made to get several characteristics of semiconductors such as: the flat band potential, the thickness of the space charge area and the carrier concentration values. Thus, it has been demonstrated that the incorporation of Er^{3+} and Sm^{3+} ions in the crystal lattice of ZnS considerably reduces the thickness of the space charge area, which leads to a significant increase in the density of the carrier's concentration and varies the flat band potential.

Conclusion

The morphological characterizations conducted by AFM of the ZnS is composed of spherical grains with a homogeneous distribution over the entire surface of the substrate. The introduction of Sm ions into the ZnS lattice leads to a notable change in topography. Alteration in the shape and grain size is obtained when we increase the concentration of Sm^{3+} dopant.

The XRD measurements show the presence of zinc blend structure with the desperation of Zn metallic phases for both dopants, the increase of Er and Sm amount lead to deterioration of the structure of the obtained films, it confirmed by the decrease of the intensity of the (200) diffraction peak.

At the end the optical characterization by UV-visible spectroscopy showed that the deposits films are highly (85%) transparent in the visible region. A shift to blue is observed the ZnS absorption edge with the increase in the concentration of Er and Sm. The optical gap values of the Er and Sm doped ZnS nanostructures are also determined, they are in good agreement with doping under the effect of Moss-Burstein phenomenon. On the other hand, the effect of Er and Sm doping on the optical properties was studied by Time Resolved Photoluminescence (TRPL).

As a conclusion to this work it's far away to put an end to this study. It's still many areas which justify further results and research in this area. It's still very large to study different material, the obtained results are the subject of a second work that ends very soon.

References

[1] J. Jie, W. Zhang, I. Bello, C. S. Lee, and S. T. Lee, "One-dimensional II-VI nanostructures: Synthesis, properties and optoelectronic applications," *Nano Today*, vol. 5, no. 4, pp. 313–336, 2010.

[2] X. Fang *et al.*, "ZnS nanostructures: From synthesis to applications," *Prog. Mater. Sci.*, vol. 56, no. 2, pp. 175–287, 2011.

[3] S. Ummartyotin and Y. Infahsaeng, "A comprehensive review on ZnS: From synthesis to an approach on solar cell," *Renew. Sustain. Energy Rev.*, vol. 55, pp. 17–24, 2016.

[4] A. N. Singh, L. R. Singh, S. N. Singh, and S. B. Singh, "Synthesis and Characterization of ZnS Nanostructured Thin Films," *Int. J. Lumin. Appl. Lumin. Appl.*, vol. 3, pp. 64–67, 2013.

[5] K. Ben Bacha, A. Timoumi, N. Bitri, and H. Bouzouita, "Structural, morphological and optical properties of sprayed ZnS thin films on various substrate natures," *Opt. - Int. J. Light Electron Opt.*, vol. 126, no. 21, pp. 3020–3024, 2015.

[6] S. Farhangfar, R. B. Yang, M. Pelletier, and K. Nielsch, "Atomic layer deposition of ZnS nanotubes," *Nanotechnology*, vol. 20, no. 32, p. 325602, 2009.

[7] O. L. Arenas, M. T. S. Nair, and P. K. Nair, "Chemical bath deposition of ZnS thin films and modification by air annealing," *Semicond. Sci. Technol.*, vol. 12, no. 10, pp. 1323–1330, 1997.

[8] M. B. Dergacheva, K. A. Urazov, G. M. Khussurova, and K. A. Leontyeva, "New Method of Pulsed Electrodeposition of Nanostructure of ZnS Films," *Coatings*, vol. 6, p. 14, 2016.

[9] Z. Ibupoto, K. Khun, X. Liu, and M. Willander, "Hydrothermal Synthesis of Nanoclusters of ZnS Comprised on Nanowires," *Nanomaterials*, vol. 3, no. 3, pp. 564–571, 2013.

[10] J. P. Borah and K. C. Sarma, "Optical and Optoelectronic Properties of ZnS

Nanostructured Thin Film," *ACTA Phys. Pol. A*, vol. 114, pp. 713–719.

[11] T. Ben Nasr, N. Kamoun, M. Kanzari, and R. Bennaceur, "Effect of pH on the properties of ZnS thin films grown by chemical bath deposition," *Thin Solid Films*, vol. 500, pp. 4–8, 2006.

[12] D. Hwang, J. Ahn, K. Hui, K. Hui, and Y. Son, "Structural and optical properties of ZnS thin films deposited by RF magnetron sputtering," *Nanoscale Res. Lett.*, vol. 7, no. 1, p. 26, 2012.

[13] A. S. and S. C. B Bhattacharjee, D Ganguli, K Iakoubovskii, "Synthesis and Characterization of Sol − gel Derived ZnS : Mn 2 + Nanocrystallites Embedded in a Silica Matrix," *Indian Acad. Sci. Synth.*, vol. 25, pp. 175–180, 2002.

[14] X. Xu, F. Wang, J. Liu, Z. Li, J. Ji, and J. Chen, "Structural and optical studies of ZnS nanocrystal films prepared by sulfosalicylic acid (C 7H 6O 6S)-assisted galvanostatic deposition with subsequent annealing," *Thin Solid Films*, vol. 520, no. 23, pp. 6864–6868, 2012.

[15] N. Fathy and M. Ichimura, "Photoelectrical properties of ZnS thin films deposited from aqueous solution using pulsed electrochemical deposition," *Sol. Energy Mater. Sol. Cells*, vol. 87, pp. 747–756, 2005.

[16] L. Miao, S. Tanemura, L. Zhao, X. Xiao, and X. T. Zhang, "Ellipsometric studies of optical properties of Er-doped ZnO thin films synthesized by sol-gel method," *Thin Solid Films*, vol. 543, pp. 125–129, 2013.

[17] H. Benelmadjat, N. Touka, B. Harieche, B. Boudine, O. Halimi, and M. Sebais, "Study of structural and optical properties of Sb doped ZnO thin films deposited by spin coating method," *Opt. Mater. (Amst).*, vol. 32, no. 7, pp. 764–767, 2010.

[18] T. Dedova, "Chemical Spray Pyrolysis Deposition of Zinc Sulfide Thin Films and Zinc Oxide Nanostructured Layers," *PhD thesis*, p. Tallinn University of Technology, 2007.

[19] M. C. Roco, "Nanoparticles and nanotechnology research," *J. Nanoparticle Res.*, vol. 1, pp. 1–6, 1999.

[20] N. U. R. A. Mustaffa, "Electrical and thermal Properties of This Composite

Semiconductors, (CdSe)1-x(Se)x and (CdS)1-x(S)x," *PhD thesis*, p. University Putra Malaysia, 2008.

[21] I. Wang, J. Minoru, "Wide-Bandga II-VI Semiconductors: Growth and Properties," *Electron. Photonic Mater.*, pp. 325–342, 2007.

[22] a. Rizzo, M. a. Tagliente, M. Alvisi, and S. Scaglione, "Structural and optical properties of silver thin films deposited by RF magnetron sputtering," *Thin Solid Films*, vol. 396, no. 1–2, pp. 29–35, 2001.

[23] M. McLaughlin *et al.*, "Properties of ZnS thin films prepared by 248-nm pulsed laser deposition," *Appl. Phys. Lett.*, vol. 63, no. 14, pp. 1865–1867, 1993.

[24] R. Vishwakarma, "Effect of substrate temperature on ZnS films prepared by thermal evaporation technique," *J. Theor. Appl. Phys.*, vol. 9, no. 3, pp. 185–192, 2015.

[25] J. Humenberger, H. Sitter, W. Huber, N. C. Sharma, and A. Lopez-Otero, "Hot wall epitaxy of II-VI compounds: CdS and CdTe," *Thin Solid Films*, vol. 90, no. 1, pp. 101–105, 1982.

[26] S. Banerjee, R. Dahal, and I. Bhat, "Low Temperature Metalorganic Chemical Vapor Deposition of Semiconductor Thin Films for Surface Passivation of Photovoltaic Devices," *Mater. Res. Soc.*, vol. 1, no. 50, pp. 3379–3390, 2016.

[27] L. A. Kolodziejski, "Molecular Beam Epitaxy of II-VI Based Heterostructures," *ACTA Phys. Pol. A*, vol. 79, no. 1, pp. 31–47, 1991.

[28] M. Opel, S. Geprägs, M. Althammer, T. Brenninger, and R. Gross, "Laser molecular beam epitaxy of ZnO thin films and heterostructures," *J. Phys. D. Appl. Phys.*, vol. 47, p. 34002, 2014.

[29] S. Shirakata, K. Saeki, and T. Terasako, "Metalorganic molecular beam epitaxy of ZnO using DEZn and H2O precursors," *J. Cryst. Growth*, vol. 237, no. 239, pp. 528–532, 2002.

[30] A. Koukitu, T. Miyazawa, H. Ikeda, and H. Seki, "Atmospheric pressure atomic layer epitaxy of ZnS using Zn and H2S," *J. Cryst. Growth*, vol. 123, pp. 95–100, 1992.

[31] K. Nagamani, P. Prathap, Y. Lingappa, R. W. Miles, and K. T. R. Reddy,

"Properties of Al-doped ZnS Films Grown by Chemical Bath Deposition," *Phys. Procedia*, vol. 25, no. i, pp. 137–142, 2012.

[32] D. U. Saenger, G. Jung, and M. Mennig, "Optical and Structural Properties of Doped ZnS Nanoparticles Produced by the Sol-Gel Method," *J. Sol-Gel Sci. Technol.*, vol. 639, pp. 635–639, 1998.

[33] R. A, Djelloul. M, Adnane. Y, Larbah. T, Sahraoui. C, Zegadi. A, Maha. B, "Properties Study of ZnS Thin Films Prepared by Spray Pyrolysis Method," *J. Nano-and Electron. Phys.*, vol. 7, p. 4045, 2015.

[34] N. H. Tran, A. J. Hartmann, and R. N. Lamb, "Epitaxial ZnS Thin Films Grown by Single Source Chemical Vapor Deposition," *J. Phys. Chem. B*, vol. 104, no. 6, pp. 1150–1152, 2000.

[35] M. R. Khelladi, L. Mentar, A. Beniaiche, L. Makhloufi, and A. Azizi, "A study on electrodeposited zinc oxide nanostructures," *J. Mater. Sci. Mater. Electron.*, vol. 24, no. 1, pp. 153–159, 2013.

[36] X. Xu, F. Wang, Z. Li, J. Liu, J. Ji, and J. Chen, "Effect of sulfosalicylic acid (C7H6O6S) on the electrodeposition of pure ZnS nanocrystal thin films from acidic solutions," *Electrochim. Acta*, vol. 87, pp. 511–517, 2013.

[37] H. M. M. N. Hennayaka and H. S. Lee, "Structural and optical properties of ZnS thin film grown by pulsed electrodeposition," *Thin Solid Films*, vol. 548, pp. 86–90, 2013.

[38] N. Fathy, R. Kobayashi, and M. Ichimura, "Preparation of ZnS thin films by the pulsed electrochemical deposition," *Mater. Sci. Eng. B Solid-State Mater. Adv. Technol.*, vol. 107, no. 3, pp. 271–276, 2004.

[39] H. Ahn and Y. Um, "Post-annealing Effects on ZnS Thin Films Grown by Using the CBD Method," *J. Korean Phys. Soc.*, vol. 67, no. 6, pp. 1045–1050, 2015.

[40] M. S. Akhtar, S. Riaz, and S. Naseem, "Optical Properties of Sol-gel Deposited ZnS Thin Films: Spectroscopic Ellipsometry," *Mater. Today Proc.*, vol. 2, pp. 5497–5503, 2015.

[41] P. C, Lokhande. V, Yermune and S, "Electrodeposition of Cd-Bi-S and Cd-Zn-

S Films," *J. Electrochem. Soc.*, vol. 138, no. 2, pp. 624–626, 1991.

[42] A. Kassim, S. Nagalingam, H. S. Min, and N. Karrim, "XRD and AFM studies of ZnS thin films produced by electrodeposition method," *Arab. J. Chem.*, vol. 3, no. 4, pp. 243–249, 2010.

[43] J. Dong, X. Zeng, C. Wang, W. Xia, X. Zhang, and M. Zhou, "Ferromagnetic behavior of non-stoichiometric ZnS microspheres with a nanoplate-netted surface," *RSC Adv.*, vol. 7, pp. 20874–20881, 2017.

[44] P. Li and S. H. Deng, "First-principles calculations reveal the n-type doping difficulties of group IIIA elements in zinc blende ZnS," *Solid State Commun.*, vol. 152, pp. 864–867, 2012.

[45] P. Li, S. Deng, L. Zhang, G. Liu, and J. Yu, "Native point defects in ZnS : First-principles studies based on LDA , LDA + U and an extrapolation scheme," *Chem. Phys. Lett.*, vol. 531, pp. 75–79, 2012.

[46] Y. Gai, J. Li, B. Yao, and J. B. Xia, "The bipolar doping of ZnS via native defects and external dopants," *J. Appl. Phys.*, vol. 105, no. 11, p. 113704, 2009.

[47] T. Aamodt, "Characterization of ZnS:Cr films for Intermediate Band Solar Cells," *PhD thesis*, p. Norwegian University of Science and Technology, 2011.

[48] J. H. Zhang, J. W. Ding, J. X. Cao, and Y. L. Zhang, "Infrared, visible and ultraviolet absorptions of transition metal doped ZnS crystals with spin-polarized bands," *J. Solid State Chem.*, vol. 184, pp. 477–480, 2011.

[49] E. M. Nasir, "Fabrication and Characterization of n-ZnS/p-Si and nZnS:Al/p-Si Heterojunction," *Int. J. Eng. Adv. Technol.*, vol. 3, pp. 425–429, 2015.

[50] D. E. Ortíz-ramos, L. A. González, and R. Ramirez-bon, "p-Type transparent Cu doped ZnS thin films by the chemical bath deposition method," *Mater. Lett.*, vol. 124, pp. 267–270, 2014.

[51] M. G. Sandoval-paz and R. Ramírez-bon, "Analysis of the early growth mechanisms during the chemical deposition of CdS thin films by spectroscopic ellipsometry," *Thin Solid Films*, vol. 517, no. 24, pp. 6747–6752, 2009.

[52] R. Zhang, B. Wang, and L. Wei, "Sulfidation growth and characterization of nanocrystalline ZnS thin films," *Vaccum*, vol. 82, pp. 1208–1211, 2008.

[53] R. Zhang, B. Wang, H. Zhang, and L. Wei, "Influence of sulfidation ambience on the properties of nanocrystalline ZnS films prepared by sulfurizing the as-sputtered ZnO films," *Appl. Surf. Sci.*, vol. 245, pp. 340–345, 2005.

[54] K. Jayanthi, S. Chawla, H. Chander, and D. Haranath, "Structural, optical and photoluminescence properties of ZnS: Cu nanoparticle thin films as a function of dopant concentration and quantum confinement effect," *Cryst. Res. Technol.*, vol. 42, no. 10, pp. 976–982, 2007.

[55] A. Mukherjee and P. Mitra, "Characterization of Sn Doped ZnS Thin Films Synthesized by CBD," *Mater. Res.*, vol. 20, no. 2, pp. 430–435, 2017.

[56] J. Lee, J. Han, J. Lee, S. Ji, and J. Yeo, "Hierarchical Nanoflowers on Nanograss Structure for a Non-wettable Surface and a SERS Substrate," *Nanoscale Res. Lett.*, vol. 10, p. 505, 2015.

[57] J. M. Chem *et al.*, "Gas sensors , thermistor and photodetector based on ZnS nanowires," *J. Mater. Chem.*, vol. 22, pp. 6845–6850, 2012.

[58] B. X. Fang *et al.*, "Single-Crystalline ZnS Nanobelts as Ultraviolet-Light Sensors," *Adv. Mater.*, vol. 21, pp. 2034–2039, 2009.

[59] Y. Yu *et al.*, "As featured in : High-gain visible-blind UV photodetectors based on chlorine-doped n-type," *Mater. Chem.*, vol. 21, p. 12632, 2011.

[60] T. Dedova *et al.*, "Effect of Zn:S Molar ratio in solution on the properties of ZnS thin films and the formation of ZnS nanorods by spray pyrolysis," *Phys. Status Solidi A*, vol. 211, no. 2, pp. 514–521, 2014.

[61] C. Y. Yeh, Z. W. Lu, S. Froyen, and A. Zunger, "Zinc-blendewurtzite polytypism in semiconductors," *Phys. Rev. B*, vol. 46, no. 16, pp. 10086–10097, 1992.

[62] T. Kryshtab, V. S. Khomchenko, J. A. Andraca-adame, and V. B. Khachatryan, "Phase transition in ZnS thin film phosphor," *J. Cryst. Growth*, vol. 275, pp. e1163–e1169, 2005.

[63] S. Salim, "Preparation and Characterization of ZnS Thin Films," *J. Appl. Sci. Rsearch*, vol. 6, no. 6, pp. 777–784, 2010.

[64] J. Vidal, O. Vigil, O. De Melo, and N. Lo, "Influence of NH3 concentration and

annealing in the properties of chemical bath deposited ZnS," *Mater. Chem. Phys.*, vol. 61, pp. 139–142, 1999.

[65] S. D. Sartale, B. R. Sankapal, and A. Ennaoui, "Preparation of nanocrystalline ZnS by a new chemical bath deposition route," *Thin Solid Films*, vol. 481, pp. 168–172, 2005.

[66] Adel H. Omran Al-khayatt1 and Mustafa D. Jaafer, "Characteristics of Nanocrystalline ZnS thin films grown on glass with different Zn ion concentrations by CBD technique.," *IOSR J. Appl. Phys.* , vol. 6, no. 1, pp. 27–35, 2014.

[67] H. Abdullah, N. O. R. H. Saadah, S. Shaari, and A. Muchtar, "Optical and Structural Properties of ZnS Thin Films Grown by CBD Technique," *Adv. Mater. Res.*, vol. 141, pp. 149–152, 2010.

[68] R. E. K. T.K. Pathak, V. Kumar, L.P. Purohit, H.C. Swart, "Substrate dependent structural, optical and electrical properties of ZnS thin films grown by RF sputtering," *Phys. E Low-dimensional Syst. Nanostructures*, vol. 84, pp. 530–536, 2016.

[69] S. M. Ho, "Role of Complexing Agent in Chemical Bath Deposition of Thin Films : A Review," *Aust. J. Basic Appl. Sci.*, vol. 31, no. 9, pp. 625–629, 2015.

[70] A. Göktaş and İ. H. Mutlu, "Room temperature ferromagnetism in Mn-doped ZnS nanocrystalline thin films grown by sol–gel dip coating process," *J. Sol-Gel Sci. Technol.*, vol. 69, pp. 120–129, 2013.

[71] A. K. Das, A. K. Buzarbaruah, and S. Bardaloi, "An Analysis of Structural and Optical Properties Undoped ZnS and Doped (with Mn , Ni) ZnS Nano Particles," *J. Mod. Phys.*, vol. 4, pp. 1022–1026, 2013.

[72] A. S. Obaid, M. A. Mahdi, Y. Yusof, M. Bououdina, and Z. Hassan, "Structural and optical properties of nanocrystalline lead sulfide thin films prepared by microwave-assisted chemical bath deposition," *Mater. Sci. Semicond. Process.*, vol. 16, no. 3, pp. 971–979, 2013.

[73] A. A. Jasib and A. A. Yousif, "The Effect of Thickness Nanoparticle ZnS Films on Optical Properties," *Int. J. Basic Appl. Sci.*, vol. 3, no. 3, pp. 38–51, 2015.

[74] N. amin F. Haque, K. S. Rahman, M. A. Islam, M. J. Rashid, M. Akhtaruzzaman, M. M. Alam, Z. A. Alothman, A. sopian, "Growth optimization of ZnS thin films by RF-Magnetron sputtering as prospective buffer layer in thin film," *Chalcogenide Lett.*, vol. 11, no. 4, pp. 189–197, 2014.

[75] S. Z. Karazhanov, P. Ravindran, A. Kjekshus, H. Fjellvag, and B. G. Svensson, "Electronic structure and optical properties of ZnX (X=O, S, Se, Te)," *Phys. Rev. B*, vol. 75, p. 155104, 2007.

[76] G. Wang *et al.*, "Synthesis and characterization of ZnS with controlled amount of S vacancies for photocatalytic H 2 production under visible light," *Sci. Rep.*, vol. 5, p. 8544, 2015.

[77] D. F. Moore, "Novel ZnS nanostructures : Synthesis , Growth Mechanism , and Applications," *PhD thesis*, p. Georgia Institute of Technology, 2006.

[78] K. HAN, "Electrodeposition cuprous oxide solar cells," *PhD thesis*, p. The university of texas at arlington, 2009.

[79] D. Lincot, A. Kampmann, B. Mokili, J. Vedel, R. Cortes, and M. Froment, "Epitaxial electrodeposition of CdTe films on InP from aqueous solutions: Role of a chemically deposited CdS intermediate layer," *Appl. Phys. Lett.*, vol. 67, no. 16, pp. 2355–2357, 1995.

[80] R. N. Bhattacharya, "Electrodeposited Two-Layer Cu–In–Ga–Se/In–Se Thin Films," *J. Electrochem. Soc.*, vol. 157, no. 7, pp. D406–D410, 2010.

[81] J. N. Yao, P. Chen, and A. Fujishima, "Electrochromic behavior of electrodeposited tungsten oxide thin films," *J. Electroanal. Chem.*, vol. 406, no. 1–2, pp. 223–226, 1996.

[82] S. Laidoudi, "Elaboration électrochimique de nanostructures d'oxyde de cuivre (Cu2O)," *PhD thesis*, p. University Ferhat Abbas Setif-1, 2015.

[83] P. Heinonen, "Fabrication of organic tunnel diodes with ultra-thin TiO2 interfacial layers," *PhD thesis*, p. Tampere University of Technology, 2015.

[84] L. Mentar *et al.*, "Effect of nitrate concentration on the electrochemical growth and properties of ZnO nanostructures," *J. Mater. Sci. Mater. Electron.*, vol. 26, pp. 1217–1224, 2014.

[85] V. Lee, Bill. Gadow, Rainer. Mitic, "Proceedings of the IV Advanced Ceramics and Applications Conference," *Atl. Press*, p. (2017), Germany.

[86] R. U. Li, "Electrodeposition And Characterization of ZnO Thin Films for Solar Cell Applications," *PhD thesis*, p. Université de montréal, 2011.

[87] A. K. Shahi, B. K. Pandey, R. K. Swarnkar, and R. Gopal, "Surfactant assisted surface studies of zinc sulfide nanoparticles," *Appl. Surf. Sci.*, vol. 257, no. 23, pp. 9846–9851, 2011.

[88] A. Begum, A. Hussain, and A. Rahman, "Effect of deposition temperature on the structural and optical properties of chemically prepared nanocrystalline lead selenide thin films," *Beilstein J. Nanotechnol.*, vol. 3, no. 1, pp. 438–443, 2012.

[89] U. Franz, "The long-Wavelength Edge of photographic sensitivity and electronic Absorption of solids," *Phys. Rev.*, vol. 92, no. 3, p. 1324, 1953.

[90] M. A. Hossain *et al.*, "Controlled growth of Cu2O thin films by electrodeposition approach," *Mater. Sci. Semicond. Process.*, vol. 63, pp. 203–211, 2017.

[91] J. Y. Liao and K. C. Ho, "A photovoltaic cell incorporating a dye-sensitized ZnS/ZnO composite thin film and a hole-injecting PEDOT layer," *Sol. Energy Mater. Sol. Cells*, vol. 86, no. 2, pp. 229–241, 2005.

[92] K. Ghezali, L. Mentar, B. Boudine, and A. Azizi, "Electrochemical deposition of ZnS thin films and their structural, morphological and optical properties," *J. Electroanal. Chem.*, vol. 794, 2017.

[93] O. K. Echendu, A. R. Weerasinghe, D. G. Diso, and F. Fauzi, "Characterization of n -Type and p -Type ZnS Thin Layers Grown by an Electrochemical Method," vol. 42, no. 4, pp. 692–700, 2013.

[94] A. NICOARA, "Mott-Schottky analysis of electrodeposited ZnS thin films A," *Stud. Univ. babes-bolyai, Chem.*, vol. 1, pp. 23–28, 2008.

[95] J. L. Birman, "Electronic energy bands in ZnS: Potential in zinc blende and wurtzite," *Phys. Rev.*, vol. 109, no. 3, pp. 810–817, 1958.

[96] C. Mark and O. Pelicano, "Effect of Solution pH and ZnCl2 on Zinc Oxide Nanostructures Grown on Zn Foil," *MATEC Web Conf.*, vol. 27, p. 2007, 2017.

[97] S. C. R.K. Pandey, S.N. Sahu, "Handbook of Semiconductor Electrodeposition," *CRC Press*, p. (2017), USA.

[98] B. Subramanian, C. Sanjeeviraja, and M. Jayachandran, "Cathodic electrodeposition and analysis of SnS films for photoelectrochemical cells," *Mater. Chem. Phys.*, vol. 71, pp. 40–46, 2001.

[99] D. R. Lide *et al.*, "CRC Handbook of Chemistry and Physics," *CRC Press*, p. (2010), USA.

[100] M. R. Khelladi, L. Mentar, A. Azizi, F. Kadirgan, G. Schmerber, and A. Dinia, "Nucleation, growth and properties of Co nanostructures electrodeposited on n-Si(1 1 1)," *Appl. Surf. Sci.*, vol. 258, no. 8, pp. 3907–3912, 2012.

[101] M. R. Khelladi, L. Mentar, A. Azizi, A. Sahari, and A. Kahoul, "Electrochemical nucleation and growth of copper deposition onto FTO and n-Si(1 0 0) electrodes," *Mater. Chem. Phys.*, vol. 115, no. 1, pp. 385–390, 2009.

[102] B. Long *et al.*, "The Optical and Electrical Characteristics of ZnS : In Thin Films Prepared by Chemical Bath Deposition Method," *ECS Solid State Lett.*, vol. 3, no. 11, pp. 140–143, 2014.

[103] S. G. Pandya, "Structural , Optical And Electrical Properties Of Chemically Deposited Zinc Sulphide Thin Films," *Int. J. Recent Sci. Res.*, vol. 7, no. 12, pp. 14700–14703, 2016.

[104] C. D. Kale, S.S., Jadhav, U.S., Lokhande, "Preparation and characterization of chemically deposited CdS films," *Indian J. Pure Appl. Phys.*, vol. 34, no. 5, pp. 324–327, 1996.

[105] L. Mentar, M. R. Khelladi, A. Beniaiche, and A. Azizi, "Influence Of The Electrodeposition Potential On The Co-Cu Alloys Thin Films Properties," *Int. J. Nanosci.*, vol. 12, no. 1, p. 1250038, 2013.

[106] A. U. Ubale and D. K. Kulkarni, "Preparation and study of thickness dependent electrical characteristics of zinc sulfide thin films," *Bull. Mater. Scii*, vol. 28, no. 1, pp. 43–47, 2005.

[107] M. A. Islam *et al.*, "Comparative Study Of ZnS Thin Films Grown By Chemical Bath Deposition And Magnetron Sputtering," *7th Int. Conf. Electr.*

Comput. Eng., pp. 86–89, 2012.

[108] A. Purohit, S. Chander, A. Sharma, S. P. Nehra, and M. S. Dhaka, "Impact of low temperature annealing on structural , optical , electrical and morphological properties of ZnO thin films grown by RF sputtering for photovoltaic applications," *Opt. Mater. (Amst).*, vol. 49, pp. 51–58, 2015.

[109] K. Benyahia, A. Benhaya, and M. S. Aida, "ZnS thin films deposition by thermal evaporation for photovoltaic applications," *J. Semicond.*, vol. 36, no. 10, pp. 3–6, 2015.

[110] F. Haque, K. S. Rahman, and M. A. Islam, "A Comparative Study on ZnS Thin Films Grown by Thermal Evaporation and Magnetron Sputtering," *IEEE Student Conf. Res. Dev.*, pp. 16–17, 2013.

[111] H. Zhu, J. F. Huang, Y. Wang, L. Y. Cao, H. Y. He, and J. P. Wu, "Synthesis and characterisation of ZnS optical thin films through cathodic electrodeposition technique," *Surf. Eng.*, vol. 27, no. 1, pp. 42–45, 2011.

[112] H. S. AL-Jumaili, "Structural and Optical Properties of Nanocrystalline Pb1-xCdxS Thin Films Prepared by Chemical Bath Deposition," *Appl. Phys. Res.*, vol. 4, no. 3, pp. 58–71, 2012.

[113] M. P. Valkonen, S. Lindroos, R. Resch, M. Leskelä, G. Friedbacher, and M. Grasserbauer, "Growth of zinc sulfide thin films on (100)Si with the successive ionic layer adsorption and reaction method studied by atomic force microscopy," *J. Mater. Res.*, vol. 13, no. 6, pp. 131–136, 1998.

[114] W.-S. Chae, T. D. T. Ung, and Q. L. Nguyen, "Time-resolved photoluminescence and photostability of single semiconductor quantum dots," *Adv. Nat. Sci. Nanosci. Nanotechnol.*, vol. 4, no. 4, p. 45009, 2013.

[115] J. Luo, S. Zhao, P. Wu, K. Zhang, C. Peng, and S. Zheng, "Synthesis and characterization of new Cd-doped ZnO/ZnS core–shell quantum dots with tunable and highly visible photoluminescence," *J. Mater. Chem. C*, vol. 3, no. 14, pp. 3391–3398, 2015.

[116] E. S. Barnard *et al.*, "Probing carrier lifetimes in photovoltaic materials using subsurface two-photon microscopy," *Sci. Rep.*, vol. 3, p. 2098, 2013.

[117] T. K. C. Tran, Q. P. Le, Q. L. Nguyen, L. Li, and P. Reiss, "Time-resolved photoluminescence study of CuInS $_2$ /ZnS nanocrystals," *Adv. Nat. Sci. Nanosci. Nanotechnol.*, vol. 1, no. 2, p. 25007, 2010.

[118] X. Wang, J. Shi, Z. Feng, and C. Li, "Visible emission characteristics from different defects of ZnS nanocrystals," *Phys. Chem. C hem. P hys*, vol. 13, pp. 4715–4723, 2011.

[119] M. O. Neil and J. Marohn, "Dynamics of Electron-Hole Pair Recombination in Semiconductor Clusters," *J. Phys. Chem.*, vol. 94, no. 10, pp. 4356–4363, 1990.

[120] M. Thackray, "Melting Point Intervals of Sulfur Allotropes," *Chem. Eng. data*, vol. 15, no. 4, pp. 495–497, 1970.

[121] W. Terdthaichairat and P. Senthongkaew, "Effect of Copper and Zinc on Microstructures , Melting Points and Corrosion Resistance of Sn-Zn-Cu-Bi Soldering Alloys," *Key Eng. Mater.*, vol. 658, pp. 59–63, 2015.

[122] D. M. Alsebaie, W. Shirbeeny, A. Alshahrie, and M. S. Abdel-wahab, "Ellipsometric Study of Optical Properties of Sm-doped ZnO Thin Films Co-deposited by RF-Magnetron Sputtering," *Opt. - Int. J. Light Electron Opt.*, vol. 148, pp. 172–180, 2017.

[123] V. Awasthi, S. K. Pandey, V. Garg, B. S. Sengar, P. Sharma, and S. Kumar, "Plasmon generation in sputtered Ga-doped MgZnO thin films for solar cell applications," *J. Appl. Phys*, vol. 119, p. 233101, 2016.

[124] E. Choi *et al.*, "Ferroelectric Sm-Doped BiMnO 3 Thin Films with Ferromagnetic Transition Temperature Enhanced to 140 K," *Appl. Mater. interfaces*, vol. 6, pp. 14836–4843, 2014.

[125] A. Hafdallah, F. Yanineb, M. S. Aida, and N. Attaf, "In doped ZnO thin films," *J. Alloys Compd.*, vol. 509, no. 26, pp. 7267–7270, 2011.

[126] M. Jun, S. Park, and J. Koh, "Comparative studies of Al-doped ZnO and Ga-doped ZnO transparent conducting oxide thin films," *Nanoscale Res. Lett.*, vol. 7, pp. 639–645, 2012.

[127] C. Moditswe, C. M. Muiva, and A. Juma, "Highly conductive and transparent Ga-doped ZnO thin films deposited by chemical spray pyrolysis," *Opt. - Int. J.*

Light Electron Opt., vol. 127, pp. 8317–8325, 2016.

[128] R. Pérez-casero *et al.*, "Er-doped ZnO thin films grown by pulsed-laser deposition Er-doped ZnO thin films grown by pulsed-laser deposition," *J. Appl. Phys.*, vol. 97, p. 54905, 2005.

[129] G. C. Xie *et al.*, "Effect of In-doping on the optical constants of ZnO thin films," *Phys. Procedia*, vol. 32, pp. 651–657, 2012.

[130] D. Lincot, A. Goux, and T. Pauporte, "Deposition of mixed zinc oxide / lanthanide films by electrochemical precipitation : The ZnO / Er system," *J. Electroanal. Chem.*, vol. 587, pp. 193–202, 2006.

[131] T. I. Incorporated *et al.*, "Paramagnetic-Resonance Studies of Rare-Earth Impurities in II-VI Compounds," *Phys. Rev.*, vol. 173, pp. 417–426, 1968.

[132] A. J. Nozik, "Photoelectrochemistry: Applications to Solar Energy Conversion," *Ann Rev Phys Chem*, vol. 29, pp. 189–222, 1978.

[133] S. Brook and B. Hall, "Surface charge development on transition metal sulfides : An electrokinetic study," *Geochim. Cosmochim. Acta*, vol. 62, no. 4, pp. 633–642, 1998.

[134] E. Environ *et al.*, "Environmental Science Ultrathin films on copper (I) oxide water splitting photocathodes : a study on performance and stability," *Energy Environ. Sci.*, vol. 5, pp. 8673–8681, 2012.

[135] L. I. Berger, "seminconductor Materials," *CRC Press*, p. (1996), USA.

[136] Z. Cynthia G, "Handbook of Electrochemistry," *Elsevier*, p. (2011),UK.

[137] J. A. Davila-pintle, R. Lozada-Morales, M. R. Palomino-Merino, J. A. Rivera-marquez, O. Portillo-Moreno, and O. Zelaya-Angel, "Electrical properties of Er-doped CdS thin films Electrical properties of Er-doped CdS thin films," *J. Appl. Phys.*, vol. 101, p. 13712, 2007.

[138] S. Komuro, T. Katsumata, T. Morikawa, X. Zhao, H. Isshiki, and Y. Aoyagi, "Highly Erbium-doped Zinc – Oxide thin film prepared by Laser ablation and its 1 . 54 m emission dynamics," *J. Appl. Phys.*, vol. 88, pp. 7129–7136, 2000.

[139] J. D. Kingsley and M. Aven, "Paramagnetic Resonance and Fluoresecence of Er3+ at Cubic Sites in ZnSe," *Phys. Rev.*, vol. 155, no. 2, pp. 235–246, 1967.

[140] U. Hotje, C. Rose, and M. Binnewies, "Lattice constants and molar volume in the system ZnS , ZnSe , CdS , CdSe," *Solid State Sci.*, vol. 5, pp. 1259–1262, 2003.

[141] W. Niu, X. Bi, G. Wang, and X. Sun, "TiO2 Gel Thin Film Doped Ce and Sm Preparation and Cyclic Voltammetry Characteristics," *Int. J. Electrochem. Sci.*, vol. 8, pp. 11943–11950, 2013.

[142] M. M. H. Farooqi and R. K. Srivastava, "Enhanced UV-vis photoconductivity and photoluminescence by doping of samarium in ZnO nanostructures synthesized by solid state reaction method," *Optik (Stuttg).*, vol. 127, pp. 3991–3998, 2016.

[143] A. Khataee, S. Saadi, B. Vahid, S. W. Joo, and B. K. Min, "Sonocatalytic degradation of Acid Blue 92 using sonochemically prepared samarium doped zinc oxide nanostructures," *Ultrason. Sonochem.*, vol. 29, pp. 27–38, 2016.

Abstract

This thesis deals with the elaboration and characterization of zinc sulfide (ZnS) nanostructures for photovoltaic applications. We used the electrochemical deposition method to synthesize these films, and this, for its simplicity and low cost. The deposit solution is composed of zinc sulfate and sodium thiosulfate ($Na_2S_2O_3$) as sources of Zn and S, respectively. This work is devised on two part. First, the samples were prepared by varying several parameters such as zinc concentration, pH, deposition potential and time deposition. The obtained nanostructures were subjected to various characterizations such as electronic (Mott-Schottky), morphological (SEM, AFM), Structural (XRD) and optical properties (UV-Vis). The Mott-Schottky measures showed that the films have an n-type conductivity when the carrier concentration and flat band potential was strongly depend on the different parameters. The morphological characterization of the samples by AFM and SEM showed a significant change of the with topography different parameters. The structural analysis shows that the obtained films are monocrystalline, they exhibit a zinc blend structure. The preferential orientation is strongly related to the experimental parameters. Studied at the end of this part the optical results show a lower transmittance. The second part is devoted to the doping of ZnS nanostructures by rare earths (Er, Sm). An improvement of optical properties (transmittance 80%) was obtained when we increase the dopants concentration and the optical band gap increases after doping from 3.54 to 3.8 eV for both dopants. The time-resolved photoluminescence decay were used to determine the charge carrier transfer (life time) of ZnS with the Er and Sm doping.

Key words; Electrodeposition, nanostructures, ZnS, Mott-Schottky, TRPL.

Étude de composé nanostructure à base de semi-conducteurs II-VI (ZnS)

Résumé :

Cette thèse est basé essentiellement sur l'élaboration et de la caractérisation des nanostructures de sulfure de zinc (ZnS) pour les applications photovoltaïques. Nous avons utilisé la méthode électrochimique pour synthétiser ces films, ce qui, pour sa simplicité et son faible coût. La solution de dépôt est constituée par le sulfate de zinc(ZnSO$_4$) et le thiosulfate de sodium (Na$_2$S$_2$O$_3$) en tant que sources de Zn et S, respectivement. Ce travail est conçu sur deux parties. La première partie a été consacré a l'effet des paramètres d'électrodéposition a savoir la concentration de zinc, le pH, le potentiel et le temps de déposition sur les propriétés des dépôts. Les nanostructures ainsi obtenues sont caractérisés par diverses technique a savoir les mesures Mott-Schottky, MEB, AFM, DRX et UV-Visible. Les mesures de Mott-Schottky ont montré que les films ont une conductivité de type n. et la concentration de porteur de charge et le potentiel de la bande plate dépendent fortement des différents paramètres. La caractérisation morphologique des échantillons par AFM et MEB a montré un changement significatif de la topographie des nanostructures avec les paramètres de déposition . L'analyse structurale montre que les films obtenus se cristallisent selon la phase cubique (structure blende) avec la présence des impuretés de zinc métallique. L'orientation préférentielle est fortement liée aux paramètres expérimentaux étudiés à la fin de cette partie, les résultats optiques montrent une transmittance faible. La deuxième partie est consacrée au dopage des nanostructures de ZnS par les terres rares (Er, Sm). Une amélioration des propriétés optiques (transmittance 80 %) a été obtenue avec l'augmentation de la concentration de dopants et l'écart de bande optique augmente après dopage de 3,54 à 3,8 eV pour les deux dopants. La décroissance de TRPL a été utilisée pour déterminer le transfert de charge (durée de vie) de ZnS avec le dopage Er et Sm.

Mots clés; Electrodéposition, nanostructures, ZnS, Mott-Schottky, TRPL.

دراسة المركبات ذات البنية النانوية لأشباه الموصلات II-VI (ZnS)

ملخص:

يستند هذا البحث بشكل أساسي على تطوير وتوصيف المواد النانوية من كبريت الزنك (ZnS) لتطبيقات الخلايا الشمسية. استخدمنا طريقة الكهروكيميائية لتجميع هذه الأفلام، وذلك لبساطتها وانخفاض التكلفة. يتكون محلول الترسب من كبريتات الزنك (ZnSO₄) وثيوسلفات الصوديوم (Na₂S₂O₃) كمصادر الزنك والكبريت، على التوالي. تم تصميم هذا العمل من لدراسة عدة عوامل. تركيز الزنك، ودرجة الحموضة، وفرق الجهد المطبق ووقت ترسب :أولا، تم من خلال تغيير العديد من المعلمات لإعداد العينات. وقد تعرض الطبقات الرقيقة على مختلف الأجهزة لدراسة خصائصها، بعد ذلك قمنا بتطعيم اللوحات الرقيقة بواسطة العناصر الأرضية النادرة وتمت دراستها.

الكلمات المفتاحية :الهياكل النانوية، كبريت الزنك، العناصر الأرضية النادرة